



Cable Guardrail End Terminal Simulation

FHWA Center of Excellence in DYNA3D Analysis

Submitted by

John D. Reid, Ph.D.
Associate Professor

Nicholas R. Hiser, M.S.M.E.
Graduate Research Assistant

MIDWEST ROADSIDE SAFETY FACILITY
University of Nebraska-Lincoln
N104 WSEC (0656)
Lincoln, Nebraska 68588
(402) 472-3084

MwRSF Research Report No. TRP-03-142-03

October 30, 2003

Technical Report Documentation Page

1. Report No. TRP-03-142-03	2.	3. Recipient's Accession No.	
4. Title and Subtitle Cable Guardrail End Terminal Simulation - FHWA Center of Excellence in DYNA3D Analysis		5. Report Date October 30, 2003	
		6.	
7. Author(s) Reid, J.D. and Hiser, N.R.		8. Performing Organization Report No. TRP-03-142-03	
9. Performing Organization Name and Address Midwest Roadside Safety Facility University of Nebraska-Lincoln N104 WSEC (0656) Lincoln, NE 68588		10. Project/Task/Work Unit No.	
		11. Contract © or Grant (G) No. DTFH61-00-X-00084	
12. Sponsoring Organization Name and Address Federal Highway Administration 6300 Georgetown Pike McLean, VA 22101		13. Type of Report and Period Covered Final Report 2003	
		14. Sponsoring Agency Code	
15. Supplementary Notes			
16. Abstract <p>The objective of this simulation research is to develop detailed finite element models of a new cable barrier end terminal being developed at the Midwest Roadside Safety Facility. The primary complicated feature of the end terminal is the slip base mechanism used on the first post in the system. Model development involved locating and isolating the physical phenomenon that occurs within the slip base mechanism, including frictional sliding behavior, friction coefficients, and bolt preloading. These phenomena were individually modeled, tested, and evaluated prior to application within a more complex model, incrementally validating the model components until a complete slip base model was attained.</p> <p>Two bolt preloading techniques were developed and evaluated, including one method which utilized a discrete spring element, and a second method which utilized pre-stressed bolt shaft elements. Both methods produced desired bolt preload, as well as acceptable correlation with data obtained from tensile testing of a slip base joint. However, after incorporation of both preloading techniques into post and slip base models, preliminary impact simulations indicated that the model using pre-stressed solid elements was significantly more accurate and thus, was used for further study. Additionally, results from a friction investigation showed that mesh size is critical for contact stability and for capturing theoretical slip behavior.</p> <p>The verified post and slip base model was then incorporated into the new cable guardrail system end terminal model. Performance of the slip base model was acceptable in both end-on impact and length-of-need impact simulations. Thus, the model was deemed appropriate for use in further development and analysis of existing cable systems, as well as alternate slip base applications.</p>			
17. Document Analysis/Descriptors LS-DYNA Simulation, Cable Guardrail End Terminal, Three Strand Cable, Nonlinear Finite Element Analysis		18. Availability Statement No restrictions.	
19. Security Class (this report) Unclassified	20. Security Class (this page) Unclassified	21. No. of Pages 107	22. Price

DISCLAIMER STATEMENT

The contents of this report reflect the views of the authors who are responsible for the facts and the accuracy of the data presented herein. The contents do not necessarily reflect the official views or policies of the Federal Highway Administration or State Highway Departments participating in the Midwest States Regional Pooled Fund. This report does not constitute a standard, specification, or regulation.

ACKNOWLEDGMENTS

This material is based upon work supported by the Federal Highway Administration (FHWA) under cooperative agreement number DTFH61-00-X-00084. The authors wish to acknowledge (1) Martin Hargrave from the FHWA, (2) the Midwest State's Regional Pooled Fund Program for sponsoring the corresponding new cable system design and crash testing projects; (3) LSTC for providing valuable support in LS-DYNA, and (4) the faculty and staff of the Midwest Roadside Safety Facility who made significant contributions to the completion of this research project.

TABLE OF CONTENTS

	Page
1. INTRODUCTION	1
1.1 Background	1
1.2 COE Simulation Research Objective	2
2. MODELING OF THE CABLE END TERMINAL	3
3. DELIVERABLES	3
4. REFERENCES	5
5. APPENDICES	7
Slip Base Modeling for Cable Guardrail Systems	

1. INTRODUCTION

At the start of this project, the Midwest Roadside Safety Facility (MwRSF) at the University of Nebraska-Lincoln (UNL) began a series of three projects designing and testing of 3-strand cable roadside and median barrier systems. These projects were funded by the Midwest States Pooled Fund Program. It was proposed to simulate the 3-strand cable barriers in conjunction with that design program as the targeted project for UNL's Center of Excellence in DYNA3D Analysis.

1.1 Background

3-strand cable barrier systems are versatile and economical barriers that are often used along non-recoverable slopes and in locations where the relatively large dynamic deflections of the barrier is acceptable. Crash tests of cable guardrail installed on slopes has shown that large automobiles can be contained and redirected by only one of the 3 cables used in the current design. This same testing clearly demonstrated that cable guardrails are more tolerant of roadside slopes than any other barrier. Further, accident data has shown that cable guardrail has the lowest injury rate of any roadside barrier system.

Crash testing of 3-strand cable systems has been extensive. A partial list of previous testing is given in the references [1-11]. Recent testing has concentrated on certifying existing systems to meet NCHRP Report 350 crash test requirements and has been very successful. Most of the historical crash testing has been performed by the Southwest Research Institute, the Texas Transportation Institute and the State of New York. However, the MwRSF has recently completed a project for the South Dakota Department of Transportation in which a cable guardrail to W-beam transition was successfully crash tested to NCHRP Report 350 requirements [10], [12].

Because of the advantages of 3-strand cable barriers, the Midwest States Pooled Fund Program initiated three projects with the MwRSF. These projects are as follows:

1. Redesign the New York flared 3-strand cable terminal and anchor as a tangent system and size the anchor block according to need. Crash test the terminal to determine whether it meets requirements of NCHRP 350.

2. Crash test 3-strand cable guardrail adjacent to a 2:1 slope in order to determine whether it meets requirements of NCHRP 350. If not, the MwRSF is to design a cable system that would meet the requirements.
3. Improve the design of the 3-strand cable median barrier by eliminating operational restrictions and maintenance problems while improving its impact performance. Specifically, determine the maximum slope 3-strand cable median barrier can be mounted on and still satisfactorily meet NCHRP Report 350 TL-3 criteria; determine post spacing required to reduce lateral deflections; determine cable configuration to eliminate or minimize vehicle penetrations under or over the barrier; and develop a breakaway release design of the cable from the post to simplify and expedite repair of the system after impact.

1.2 COE Simulation Research Objective

The objective of the proposed simulation research is to develop detailed finite element models of 3-strand cable roadside and median barrier systems in support of the design and testing program described above. However, in order to be held accountable for specific deliverables, simulation models for the cable barrier end terminal project will be developed and distributed through presentations, publications and models delivered to NCAC. LS-DYNA, a nonlinear, finite element analysis code, is used for the simulation effort [13].

The benefits of this development are three-fold. First, the simulation effort will provide analysis support for the research projects at the MwRSF in which three separate, but related projects for developing NCHRP Report 350 3-strand cable barrier systems are being designed and tested. Second, enhanced understanding of the crashworthiness of 3-strand cable barrier systems will be obtained. This understanding is gained through detailed analysis available in FEA which is not available through testing. Third, and finally, the resulting models will be available for other researchers to modify and incorporate in future research and design projects.

2. MODELING OF THE CABLE END TERMINAL

Details of the simulation effort associated with the cable end terminal have been published in Nicholas Hiser's Masters Thesis and will not be repeated here. Instead a copy of that Thesis is included as Appendix A.

3. DELIVERABLES

The following products were developed during this project as a result of the FHWA funded COE at UNL.

Models

Two LS-DYNA models were submitted to the NCAC for public distribution of the cable end terminal design developed at UNL: (1) an end-on impact model, and (2) a LON impact model

Publications

N.R. Hiser and J.D. Reid, "Modeling Slip Base Mechanisms," abstract submitted to *ICrash 2004* October 7, 2003, sponsored by *International Journal of Crashworthiness*, if accepted, paper due March 2004.

J.D. Reid and N.R. Hiser, "Friction Modeling between Solid Elements," *International Journal of Crashworthiness*, accepted for publication October 14, 2003 pending minor revisions.

J.D. Reid, N.R. Hiser and T.J. Paulsen, "Simulation and Bogie Testing of a New Cable Barrier Terminal," *Crashworthiness, Occupant Protection and Biomechanics in Transportation Systems - 2003*, ASME, November 2003.

J.D. Reid and B.A. Coon, "Finite Element Modeling of Cable Hook Bolts," *Seventh International LS-DYNA Users Conference*, Dearborn, MI, May 2002, pp. 17-11 to 17-22.

MwRSF Research Reports

Coon, B.A., Faller, R.K., and Reid, J.D., *Cable Barrier Literature Review*, Final Report to the Midwest State's Regional Pooled Fund Program, Report No. TRP-03-118-02, MwRSF - UNL, July 10, 2002.

Fating, R.M. and Reid, J.D., *Dynamic Impact Testing of S75x8.5 Steel Posts (Cable Guardrail Posts)*, Final Report to the Midwest State's Regional Pooled Fund Program, Report No. TRP-03-117-02, MwRSF - UNL, June 28, 2002.

Master Thesis

Ritesh M. Fating, M.S. Mechanical Engineering, *Dynamic Impact Testing and Simulation of Cable Barrier Posts*, December 2002.

Nicholas R. Hiser, M.S. Mechanical Engineering, *Slip Base Modeling for Cable Guardrail Systems*, May 2003.

Tony J. Paulsen, M.S. Mechanical Engineering, *Improvements to the Suspension and Modularization of the C2500 Pickup Truck Finite Element Model*, May 2003.

4. REFERENCES

1. C.E. Buth, W.L. Campise, M.L. Love, L.I. Griffin III and D.L. Sicking, *Performance Limits of Longitudinal Barrier Systems*, Texas Transportation Institute, May 1985.
2. M.E. Bronstad, J.D. Michie and J.B. Mayer, Jr., "Minicar Crash Test Evaluation of Longitudinal Traffic Barriers," *Transportation Research Record 1024*, TRB, National Research Council, Washington, D.C., 1985, pp. 9-18.
3. SwRI Project No. 06-8299-001, 3 Reports to the South Dakota Department of Transportation and the Federal Highway Administration, Prepared by Southwest Research Institute, San Antonio, Texas, January 1989.
4. C.E. Kimball and K.L Hancock, *Develop Performance Standards and Hardware for Low Service Level Guardrail System*, SwRI Project 06-8615, NCHRP 22-5, January 1989.
5. *Crash-Test Evaluation of a Franklin Post and Cable Guardrail System - Test Nos. SD-1, SD-2 and SD-3*, (actually 3 separate reports) SwRI Project No. 06-2696-001, Report to the South Dakota Department of Transportation, Prepared by Southwest Research Institute, San Antonio, Texas, August 1989.
6. R.G. Phillips, A.B. Tyrell, J.E. Bryden and J.S. Fortuniewicz, *Cable Guiderail Breakaway Terminal Ends*, Research Reprt 148, New York State Dept. of Transportation, March 1990.
7. M.H. Ray and J.E. Bryden, *Summary Report on Selected Guardrails*, Momentum Engineering, Report No. FHWA7589-1, June 1992.
8. Mak, K.K., and Menges, W.L., *Crash Testing and Evaluation of GI Wire Rope Guardrail System*, Research Study No. RF 471470, Contract No. DTFH61-89-C-00089, Draft Report to the Federal Highway Administration, Prepared by Texas Transportation Institute, Texas A&M University, College Station, Texas, December 1994.
9. D.L. Bullard, Jr., and W.L. Menges, W.L., *Crash Testing and Evaluation of the WSDOT Three Strand Cable Rail System*, Research Study No. 270687-WDT2, Texas Transportation Institute, Texas A&M University, College Station, Texas, June 1996.
10. Faller, R.K., Sicking, D.L., Rohde, J.R., Holloway, J.C., Keller, E.A., and Reid, J.D., *Crash Testing of South Dakota's Cable Guardrail to W-Beam Transition*, South Dakota Report No. SD98-16, Final Report to the South Dakota Department of Transportation, Report No. TRP-03-80-98, Project No. SPR-3(017), MwRSF - UNL, December 4, 1998.

11. D.L. Bullard, Jr., W.L. Menges, W.L., C.E. Buth and S.K. Schoenman, *NCHRP Report 350 Test 3-11 of the Washington 3-Strand Cable Barrier with New York Cable Terminal*, Project No. 404211-8, Texas Transportation Institute, Texas A&M University, College Station, Texas, March 2000.
12. Ross, H.E., Sicking, D.L., Zimmer, R.A. and Michie, J.D., *Recommended Procedures for the Safety Performance Evaluation of Highway Features*, National Cooperative Research Program (NCHRP) Report No. 350, Transportation Research Board, Washington, D.C., 1993.
13. Hallquist, J.O., *LS-DYNA Keyword User's Manual - Version 950*, Livermore Software Technology Corporation, Livermore, CA, 1999.

SLIP BASE MODELING FOR CABLE GUARDRAIL SYSTEMS

by

Nicholas R. Hiser

A THESIS

Presented to the Faculty of
The Graduate College at the University of Nebraska
In Partial Fulfillment of Requirements
For the Degree of Master of Science

Major: Mechanical Engineering

Under the Supervision of Professor John D. Reid

Lincoln, Nebraska

April, 2003

SLIP BASE MODELING OF CABLE GUARDRAIL SYSTEMS

Nicholas R. Hiser, M.S.

University of Nebraska, 2003

Advisor: John D. Reid

Cable guardrail systems are used exclusively for the purpose of shielding roadside hazards from impact with errant vehicles. The end terminals are crucial to the overall performance of the cable system as they serve as the anchor, but must remain crashworthy for end-on impacts. The slip base mechanism is commonly used to facilitate breakaway end terminals for cable guardrail systems.

The objective of this study was to conduct a detailed investigation of the slip base mechanism, and to develop improved methods of modeling slip base structures in LS-DYNA. The methodology for the LS-DYNA model development involved locating and isolating the physical phenomenon that occurs within the slip base mechanism, including frictional sliding behavior, friction coefficients, and bolt preloading. These phenomenon were individually modeled, tested, and evaluated prior to application within a more complex model, incrementally validating the model components until a full end terminal model was attained.

A solid element friction investigation in LS-DYNA concluded that mesh size is critical for contact stability and for capturing theoretical slip behavior, and it also verified the ability of LS-DYNA to capture the static-to-dynamic friction transition. Two bolt preloading techniques were developed and evaluated, including one method which utilized a discrete spring element, and a second method which utilized prestressed bolt shaft elements. Both methods produced desired bolt preload, as well as acceptable correlation with data obtained from tensile testing of a slip base joint. However, after incorporation of both preloading techniques into post and slip base models, preliminary impact simulations verified only the model using prestressed solid elements. The verified post and slip base model was then incorporated into a cable system end terminal model, and finally into a full-length cable system model. The slip base model performed acceptably in both end on impact and length-of-need impact simulations. Finally, it was deemed appropriate for use in further development and analysis of existing cable systems, as well as alternate slip base applications.

ACKNOWLEDGMENTS

The author wishes to acknowledge the following people and organizations that made this project, and its completion, possible. First and foremost, a sincere thanks to Dr. John Reid whose experience, insight, and advice were invaluable in all aspects of the graduate experience. Secondly, a great deal of thanks to the staff and leadership of the Midwest Roadside Safety Facility for providing a wonderful learning opportunity. Thanks also to the faculty and staff of the UNL Department of Mechanical Engineering for providing academic challenges and guidance in various courses of study. A special thanks is extended to Ken Koch and the Parker Hannifin Corporation, whose patience and flexibility has been more than accommodating throughout the whole of this academic pursuit. The simulation work performed during this project was completed utilizing the Research Computing Facility of the University of Nebraska-Lincoln. This material is based upon work partially supported by the Federal Highway Administration under the cooperative agreement number DTFH61-00-X-00084.

I would also like to offer a personal thanks to some individuals whose love and support has directly influenced my ability and desire to complete this work. To my lifelong buddies, Mark, Bob, and Tory: May our weekend adventures continue for as long as we do. It is something special to have good friends to share the fun in life with. To my in-laws, Larry, Sue, Jeanette, and Missy: Thank you for accepting me, supporting me, and loving me as your son and brother. To my Grandparents, Howard and Davene Holliday, and Fred Hiser, the most generous and loving grandparents a person could have: Thank you for being such an important part of my life. To my sister, Jennifer Ayn Degen, all the way up in Alaska: Thank you for setting such a good example for an impressionable little brother all those years ago. Living up to my big sis may be difficult, but I'm convinced the chase has led me down the right path. To my Dad and Mom, Rod and Jeane Hiser, the people who taught me how to think, love, and live: Thank you for your devotion as parents and teachers, for your unconditional love and support, and for your friendship. Finally, and most importantly, to my lovely wife and best friend, Jennifer Hiser, the most patient and caring woman I have ever known: I was only able to reach my goal through your patience, support, understanding, and sacrifice. The part you played was no less significant than the actual work I produced. Thank you for your enduring love, incredible patience, and unwavering moral support. Let us now move on to other things that life has to offer.

DISCLAIMER STATEMENT

The contents of this report reflect the views of the author who is responsible for the facts and the accuracy of the data presented herein. The contents do not necessarily reflect the official views or policies of the University of Nebraska-Lincoln, the state highway departments participating in the Midwest State's Regional Pooled Fund Program, or the Federal Highway Administration. This report does not constitute a standard, specification, or regulation.

TABLE OF CONTENTS

	Page
1. INTRODUCTION.....	1
1.1. Background.....	1
1.2. Objective and Problem Statement.....	2
1.3. Research Methodology.....	2
2. EXISTING CABLE GUARDRAIL SYSTEMS.....	4
2.1. UK Four Rope Safety Fence.....	4
2.2. Wood Post Cable System.....	6
2.3. G1 Cable System.....	8
2.4. New York DOT Cable System.....	11
2.5. MwRSF Cable System.....	14
3. SLIP BASE LITERATURE REVIEW.....	18
3.1. Slip Base Theory and Analytical Techniques.....	18
3.1.1. Slip Base Fundamentals.....	18
3.1.1.1. Clamping Force.....	18
3.1.1.2. Frictional Slip Force.....	19
3.1.1.3. Base Fracture Energy.....	21
3.1.1.4. Momentum Transfer.....	23
3.1.2. Quasi-Static Analysis.....	24
3.1.3. Three-Stage Dynamic Analysis.....	28
3.2. Slip Base Testing Results.....	30
3.2.1. Slip Base Slip Forces.....	31
3.2.2. Slip Base “Lock-Up”.....	32
3.2.3. Data Correlation with Analytical Techniques.....	34
4. CLAMPING FORCES LITERATURE REVIEW.....	37
4.1. Importance of Jolt Preload.....	37
4.2. Preload Control Methods.....	38
4.2.1. Bolt Strain Measurement.....	38
4.2.2. Torque Measurement.....	39
4.2.3. Alternate Preload Control Methods.....	39
4.2.3.1. Belleville Washer Test.....	41
4.3. The Torque-Tension Relationship.....	43
4.3.1. Analytical Torque-Tension Relationship.....	43
4.3.2. Empirical Torque-Tension Relationship.....	47
4.3.2.1. Obtaining Torque-Tension Data using Pressure Paper.....	50
4.3.3. Analytical-Empirical Data Correlation.....	51
4.3.4. Using the Torque-Tension Relationship in Practice.....	52
5. EXISTING SLIP BASE MODELING IN LS-DYNA.....	55
5.1. NCAC Oregon 3x3 Sign Post Slip Base.....	56

5.1.1. Model History.....	56
5.1.2. Model Description.....	56
5.1.3. Discussion of Results.....	61
5.1.4. Model Evaluation.....	66
5.2. TTI Arizona DOT Luminaire Pole Slip Base.....	68
5.2.1. Model History.....	68
5.2.2. Model Description.....	68
5.2.3. Discussion of Results.....	72
5.2.4. Model Evaluation.....	78
5.3. Conclusions.....	81
6. FRICTION MODELING IN LS-DYNA.....	82
6.1. LS-DYNA Theory.....	82
6.2. LS-DYNA Friction Simulation.....	84
6.3. Conclusions.....	89
7. SLIP BASE CLAMPING TECHNIQUES IN LS-DYNA.....	90
7.1. Jnt-1 Bolted Joint Model.....	90
7.2. Jnt-2 Bolted Joint Model.....	92
7.3. Jnt-3 Bolted Joint Model.....	97
7.3.1. Stress-1 Solid Element Prestress Model.....	98
7.3.2. Using Prestressed Solid Elements for Bolt Preload.....	103
8. SLIP BASE COMPONENT TESTING AND SIMULATION.....	107
8.1. MTS Pull-Test Data.....	107
8.2. LS-DYNA Pull-Test Simulations.....	113
9. SLIP BASE MODELING – RIGID CYLINDER IMPACT.....	120
9.1. Sb-1 Post and Slip Base Model.....	120
9.2. Sb-2 Post and Slip Base Model.....	121
9.3. Sb-3 Post and Slip Base Model.....	125
9.4. Comparison of Sb-2 and Sb-3 Slip Base Models.....	129
9.4.1. Weak Axis Impact.....	129
9.4.2. Strong Axis Impact.....	135
9.4.3. Conclusions.....	139
10. END TERMINAL IMPACT SIMULATION.....	140
10.1. Sb-1 End Terminal Development and Simulation.....	140
10.2. Sb-3 End Terminal Simulation.....	145
11. LENGTH-OF-NEED IMPACT SIMULATION.....	154
11.1. CT-1 Crash Test Results.....	154
11.2. Lon-1 Length-of-need Impact Simulation.....	158
11.3. Lon-2 Length-of-need Impact Simulation.....	162
11.4. Lon-3 Length-of-need Impact Simulation.....	163
11.5. Conclusions.....	167

12. SUMMARY and CONCLUSIONS.....	170
13. FUTURE WORK and RECOMMENDATIONS.....	176
14. REFERENCES.....	178
15. APPENDICES.....	182
APPENDIX A	
Fortran Program, Solid Element Stress Initialization.....	182

LIST OF FIGURES

	Page
Figure 1. U.K. Four-Rope Safety Fence and End Terminal.....	5
Figure 2. Wood Post Cable Guardrail System and End Terminal.....	7
Figure 3. G1 Cable Guardrail System and End Terminal.....	9
Figure 4. New York Cable Guardrail System and End Terminal.....	12
Figure 5. MwRSF Cable Guardrail System End Terminal.....	15
Figure 6. MwRSF Cable Guardrail System End Terminal, CT-2 Crash Test.....	15
Figure 7. General Force vs. Deflection Relationship for Slip Base Mechanism.....	22
Figure 8. Slip Base Free Body Diagram.....	24
Figure 9. Base Resisting Force vs. Impact Force for Various Friction Coeff.....	25
Figure 10. Base Resisting Force vs. Impact Force for Various Impact Heights.....	26
Figure 11. Base Resisting Force vs. Impact Force for Various Bolt Preloads.....	27
Figure 12. Breakaway Force vs. Friction Coefficient for Two Impact Heights.....	28
Figure 13. Change in Velocity vs. Impact Height, NCHRP 318 Program.....	30
Figure 14. Quasi-static Force vs. Deflection Test Data for Slip Base.....	31
Figure 15. Slip Base Warpage and Lockup due to Pole Deformation.....	33
Figure 16. Alternate Methods of Controlling Slip Base Clamping Forces.....	40
Figure 17. Bolt Tension Using Belleville Springs.....	42
Figure 18. Bolt Tension Using Standard Torquing Method.....	42
Figure 19. Torque-tension Curves Showing Effect of Repetitive Installation.....	48
Figure 20. Union Metal Test Data, Applied Torque vs. Bolt Tension.....	48
Figure 21. Torque-tension Data Correlation, 1.00-8 UNC Bolt.....	49
Figure 22. Torque-tension Data Correlation, 0.625-11 UNC Bolt.....	50
Figure 23. Torque-tension Data Correlation, 0.500-13 UNC Bolt.....	51
Figure 24. NCAC Oregon 3x3 Slip Base Model Geometry.....	57
Figure 25. Bolted Joint Model, NCAC Oregon 3x3 Slip Base.....	57
Figure 26. Bolt Spring Load Curve, NCAC Oregon 3x3 Slip Base Model.....	58
Figure 27. Spring Element Identification, Contact Entity.....	58
Figure 28. Keeper Plate failure, NCAC Oregon 3x3 Slip Base Model.....	61
Figure 29. Deforc Data, NCAC Oregon 3x3 Slip Base Clamping Loads.....	62
Figure 30. Rcforc Data, NCAC Oregon 3x3 Slip Base Model.....	63
Figure 31. Secforc Data, NCAC Oregon 3x3 Slip Base Model.....	64
Figure 32. Glstat Data, NCAC Oregon 3x3 Slip Base Model.....	65
Figure 33. Matsum Data, NCAC Oregon 3x3 Slip Base Model.....	65
Figure 34. TTI Arizona D.O.T. Luminaire Slip Base Model Geometry.....	69
Figure 35. Bolted Joint Model, TTI Arizona D.O.T. Luminaire Slip Base.....	69
Figure 36. Bolt Spring Load Curve, TTI Arizona D.O.T. Slip Base Model.....	70
Figure 37. Spring Element Identification, Contact Entity.....	70
Figure 38. Slip Base Activation, TTI Arizona D.O.T. Slip Base Model.....	72
Figure 39. Bolt Deformation due to Initial Penetrations.....	73
Figure 40. Deforc Data, Clamping Loads, TTI Slip Base Model.....	74
Figure 41. Rcforc Data, TTI Arizona DOT Slip Base Model.....	75
Figure 42. Secforc Data, TTI Arizona DOT Slip Base Model.....	76
Figure 43. Glstat Data, TTI Arizona DOT Slip Base Model.....	77

Figure 44. Matsum Data, TTI Arizona DOT Slip Base Model.....	77
Figure 45. Friction Coefficient vs. Relative Velocity.....	83
Figure 46. LS-DYNA Friction Investigation Model.....	85
Figure 47. Slip Force vs. Time, Friction Constant $f_s=f_d=0.2$, Velocity Varies....	87
Figure 48. Slip Force vs. Time, Friction Varies $f_s=0.2$, $f_d=0.1$, Velocity Varies..	89
Figure 49. Jnt-1 Bolted Joint Model.....	91
Figure 50. Deforc Clamping Data, Jnt-1 Bolted Joint Model.....	91
Figure 51. LS-DYNA Model Jnt-2, Clamping Technique #2.....	92
Figure 52. Bolt, Nut, and Washers Following Slip Base Activation (CT-2).....	93
Figure 53. Force vs. Deflection, Discrete Spring Element in Jnt-2 Model.....	96
Figure 54. LS-DYNA Deforc Data, Preload Verification of Model Jnt-2.....	96
Figure 55. Six Principal Stress Components on a Volume Element.....	99
Figure 56. Stress-1, Element Prestress Investigation Model.....	100
Figure 57. Element Stress Fringe Plots.....	101
Figure 58. Secforc Data, Tensile Load due to Prestress in Solid Elements.....	101
Figure 59. Glstat Data, Energy due to Prestress in Solid Elements.....	102
Figure 60. LS-DYNA Model Jnt-3, Clamping Technique #3.....	104
Figure 61. Secforc Data, Preload Verification of Model Jnt-3.....	105
Figure 62. MTS Machine with Slip Base Jig.....	107
Figure 63. CAD Drawing of Slip Base Jig.....	108
Figure 64. Slip Base Jig, Front and Side Views.....	109
Figure 65. Force vs. Displacement, Quasi-static MTS Pull Test Data.....	111
Figure 66. Dynamic MTS Pull Test Data, Force vs. Displacement.....	113
Figure 67. Pull Test Simulation, Slip Base Joint Models.....	115
Figure 68. MTS Pull-test and Simulation Sequences.....	115
Figure 69. Slip Force vs. Displacement Simulation Data.....	116
Figure 70. Sb-2 Post and Slip Base FEA Model.....	122
Figure 71. Sb-2 Post and Slip Base and Rigid Impact Cylinder.....	123
Figure 72. Model Sb-2, Bolt and Slip Base Clamping Loads.....	124
Figure 73. Sb-2 Slip Base Activation when Impacted by Rigid Cylinder.....	124
Figure 74. Glstat Data, Sb-2 Post and Slip Base Impacted by Rigid Cylinder.....	125
Figure 75. Model Sb-3, Bolt and Slip Base Clamping Loads.....	127
Figure 76. Sb-3 Slip Base Activation when Impacted by Rigid Cylinder.....	127
Figure 77. Glstat Data, Sb-3 Post and Slip Base Impacted by Rigid Cylinder.....	128
Figure 78. Sb-2 Model Slip Base Lock-up, Weak Axis Bumper Height Impact...	130
Figure 79. Sb-3 Model, Weak Axis Bumper Height Impact.....	131
Figure 80. Bolt Comparison During Slip Base Activation.....	132
Figure 81. Stress Fringe Plots Indicating Binding of Sb-2.....	133
Figure 82. Sb-2 Model, Bumper Height Impact, Strong Axis.....	136
Figure 83. Sb-3 Model, Bumper Height Impact, Strong Axis.....	137
Figure 84. Sb-3 Model Bolt Failure, Bumper Height Impact, Strong Axis.....	138
Figure 85. CTB-4, Prototype End Terminal and Bogie Vehicle.....	141
Figure 86. Three-strand Cable Guardrail End Terminal FEA Model.....	142
Figure 87. Cable End Fitting Modeling Approximation.....	144
Figure 88. Time Comparison, High-Speed Film vs. LS-Dyna Simulation.....	147
Figure 89. Individual Bolt Preload During Sb-3 End Terminal Impact.....	149

Figure 90. Total Cable Tension During Sb-3 End Terminal Impact.....	150
Figure 91. Sb-3 Slip Base Activation Sequence, End Terminal Impact.....	151
Figure 92. Deformation Comparison.....	152
Figure 93. CT-1 Length-of-need Test Setup and Impact Location.....	155
Figure 94. Aftermath of CT-1 Length-of-need Crash Test.....	156
Figure 95. CT-1 Cable Tension Load Cell Data.....	157
Figure 96. CT-1 Slip Base Damage.....	158
Figure 97. Model Lon-1 and Lon-2, Cable System Length-of-need Impact.....	159
Figure 98. Model Lon-1, Secforc Data, Cable Tension.....	160
Figure 99. Model Lon-1, Sb-3 Post and Slip Base Following Impact.....	160
Figure 100. Model Lon-2, Secforc Data, Cable Tension.....	162
Figure 101. Model Lon-2, Sb-3 Slip Base Failure Following Impact.....	163
Figure 102. Model Lon-3, Length-of-need Impact, Pickup Truck Model.....	164
Figure 103. Model Lon-3, Cable System Length-of-need Impact Sequence.....	165
Figure 104. Model Lon-3, Secforc Data, Cable Tension.....	166
Figure 105. Model Lon-3, Sb-3 Post and Slip Base Following Impact.....	167

LIST OF TABLES

	Page
Table 1. Measured and Predicted Velocity Changes During Slip Base Impacts, Pendulum Test Data Correlation.....	34
Table 2. Measured and Predicted Velocity Changes During Slip Base Impacts, Full-scale Bogie Test Data Correlation.....	35
Table 3. Torque Coefficient Values for Threaded Fasteners.....	45
Table 4. Kt Values Defined in Highway Research Record 222.....	46

1 INTRODUCTION

1.1 Background

Cable guardrail systems are used extensively for the purpose of shielding obstacles along the road from impact with errant vehicles. These systems consist of high-tension steel cables supported by weak posts. When an errant vehicle obliquely impacts the cable system, sufficient tension is developed within the cables to redirect the vehicle, effectively shielding the roadside hazard and increasing the safety of the driver. Due to the likelihood of a longitudinal impact with the end of the cable guardrail system, a crashworthy end terminal is required. For this purpose, various crashworthy end terminal designs for cable guardrail systems have been designed using the breakaway feature of the slip base mechanism.

Slip base mechanisms are often used in the roadside safety industry at the base of structures such as sign posts, luminaire poles, and guardrail system posts. Due to the breakaway feature of the slip base, it has considerable potential for reducing the amount of crash resistance, and thus occupant injury, when vehicles inadvertently leave the roadway and strike these fixed objects.

Due to observed inadequacies in existing cable system end terminal designs, the Midwest Roadside Safety Facility (MwRSF) has designed an improved breakaway end terminal which utilizes the slip base mechanism on the end system post. Because the end terminal behavior is critical to overall system behavior during an impact, it was concluded that a detailed slip base investigation would be conducted.

Due to the observations of erratic slip base behavior in practice, and current limitations with existing slip base analytical techniques and computer models, a new slip

base modeling effort was undertaken in this study. The LS-DYNA finite element code, developed by the Livermore Software Technology Corporation (LSTC) (L), has been chosen for use in modeling of the slip base mechanism in this study. LS-DYNA is an explicit, non-linear finite element analysis code that has proven its usefulness in the roadside safety industry due to its widespread use and verified ability to accurately model dynamic impact events. For use in predicting slip base behavior, the LS-DYNA model must be able to capture the dynamic interactions of the various slip base components. Of utmost importance is the ability to realistically capture the frictional sliding event, which is the primary failure mode of the joint upon breakaway.

1.2 Objective and Problem Statement

It was the overall objective of this study to conduct a detailed investigation of the slip base mechanism, and to develop improved methods of slip base modeling in LS-DYNA. More specifically, it was the goal of this research to produce a detailed, validated LS-DYNA model of the rectangular, unidirectional slip base that is used extensively for breakaway end terminals on common cable guardrail systems. The validated model is intended for use in the development of the MwRSF cable guardrail system end terminal, as well as other slip base applications.

1.3 Research Methodology

An extensive literature review was initially conducted to summarize the background information relevant to this study. The various cable guardrail systems and their end terminal designs were first summarized. Prior theoretical and analytical investigations of the slip base was documented, as well as significant discoveries that were observed during laboratory testing of slip base impacts. The significance of bolt preload and the

torque-tension relationship of structural bolts was included as a valuable reference. The literature review was concluded with a detailed investigation of two existing LS-DYNA slip base models.

The general methodology for the LS-DYNA simulation portion of this study involved locating and isolating the physical phenomenon that occurs within the slip base components during installation and activation. The physical phenomenon of most interest with regard to slip base behavior are friction coefficients, frictional sliding behavior, and the initial preloading of the bolts. These mechanical interactions were individually modeled, tested, and evaluated prior to assembly into a larger and more complex model. The verified components were incorporated into a detailed model of the cable guardrail end terminal system. This cable system end terminal model was finally utilized by Dr. John Reid of the University of Nebraska-Lincoln to run full-scale length-of-need impacts on an LS-DYNA cable guardrail system model. This model could subsequently be used to analyze prior full-scale crash tests results, as well as assist in the modification or further development of the MwRSF cable system.

2 EXISTING CABLE GUARDRAIL SYSTEMS

Developing end terminals that are safe and effective has proven to be a difficult design problem for longitudinal barriers of all types, including cable guardrail systems. Cable guardrail systems are longitudinal barrier systems used extensively along roadways to help shield obstacles from errant vehicles. These systems are used exclusively for redirection of vehicles in oblique impacts. All cable guardrail systems are terminated at the ends with some type of anchor that is able to withstand high tensile loads in the cables during an oblique impact without the cables breaking free. However, due to the probability of end-on and departure impacts, cable system end terminals and anchors are a point of concern for roadway safety engineers. The various cable system designs employed along the nations highways inherently exhibit varying levels of safety for the drivers of errant vehicles in end-on and departure impacts, as shown by Coon et al in a previous cable barrier literature review (2). Included herein is a summary of the cable guardrail systems and their respective end terminals as they relate to this study.

2.1 UK Four-Rope Safety Fence

In the late 1960's the U.K. Transport and Road Research Laboratory (TRRL) assisted in the development of a weak post-and-wire safety fence for containment of cars. The design consisted of two wire ropes at the same height resting in slots atop weak steel posts. This design remedied the then common problem of vehicles snagging on line posts during impact, although, it often resulted in either vehicle override or underride of the cables. Beginning in 1986, a new wire-rope safety fence was being developed in the United Kingdom to remedy the weaknesses in the two-rope system (3).

The final U.K. cable system design was comprised of 4 steel interwoven cables supported on weak steel posts of z-shaped cross-section, with post spacing of 2.4 meters on center. Refer to Figure 1 for illustrations of the U.K. four-rope safety fence (3-4).

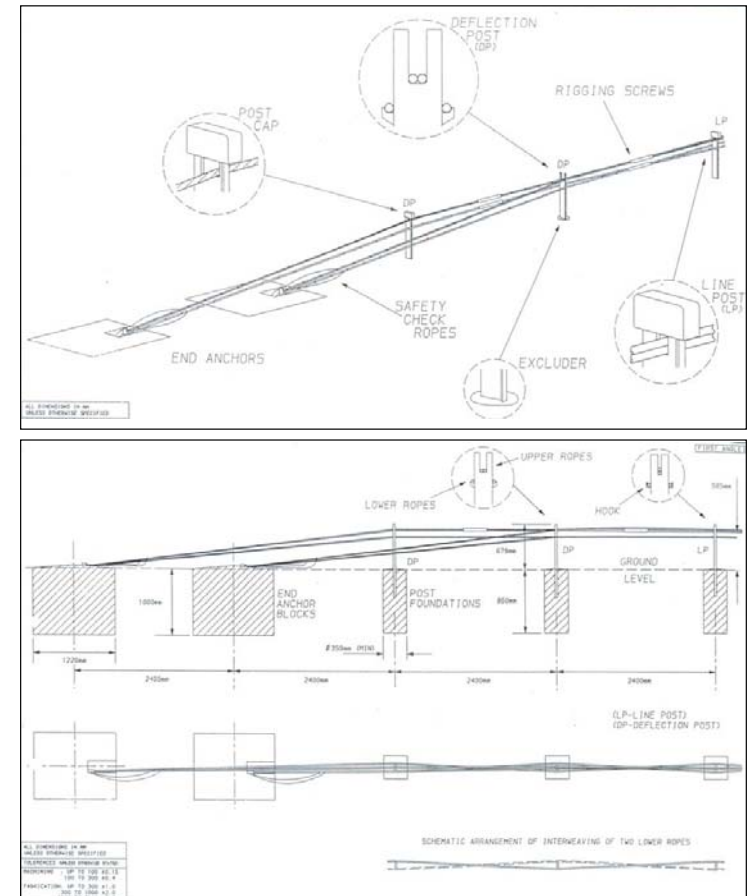


Figure 1. U.K. Four-Rope Safety Fence and End Terminal

The steel z-section line posts used in the U.K. cable system are installed so the strong axis resists oblique mid-length impacts, with the weak axis offering minimal resistance to longitudinal impacts, thus reducing the potential for snagging and rollover of impacting vehicles. The systems' top two cables rest in a vertical slot at a height of 585 mm (23 inches), and the lower pair of cables are supported by brackets on either side of the posts at a height of 490 mm (19.3 inches). The lower cable pair is interwoven between each cable to improve the rope retention by trapping it against the post, thus helping to maintain desirable cable height during impact. To terminate the cable system, the two cable pairs are turned down over a distance of 2.4 m, where they are attached to two separate concrete anchor blocks buried underground. Finally, turnbuckles are used to pretension all cables with a static load of 22.4 kN (3-4).

The U.K. four-rope safety fence was subjected to numerous mid-length crash tests that proved it provided adequate redirective capability for both small and full-size automobiles. However, the end terminal design was at no time tested or approved for end-on or departure impacts, making this end terminal subject to safety concerns. (3)

2.2 Wood Post Cable System

The wood post cable guardrail was developed in the late 1960's, and it was intended to be a weak-post cable guardrail system. However, full scale crash testing in 1985 with a small car impacting at mid-length of the system resulted in vehicle rollover due to the excessive strength of the wood posts in the longitudinal direction. A later study determined that boring a 1.5 inch diameter hole in the posts parallel with the cable below the ground line resulted in adequate performance in mid-length impact tests. (5) Refer to Figure 2 for illustrations of the wood post cable system and end terminal.

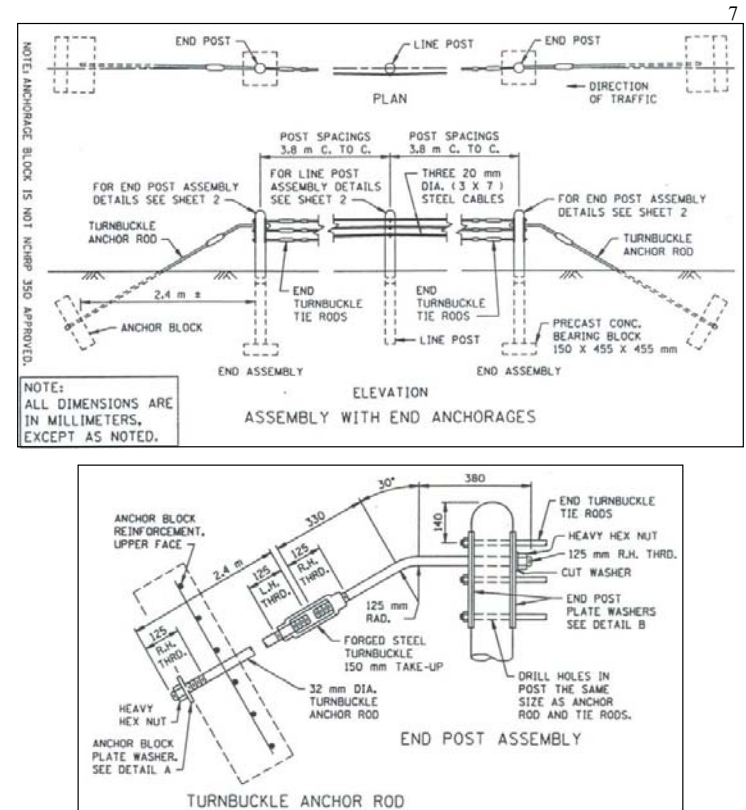


Figure 2. Wood Post Cable Guardrail System and End Terminal

The terminal developed for the wood post system consists of a single wood post placed on top of a precast concrete bearing block. Steel plates on either side of the wood end post serve as a connection point for the ends of the three steel cables and a single steel anchor rod. The steel anchor rod slopes to the ground at a 30 degree angle where its end is set in a concrete anchor block buried 8 ft (2.4 m) from the end post. As mentioned

previously, the 1.5 inch (38 mm) diameter hole drilled in the wood posts parallel with the cable and below grade significantly improves the performance of this barrier for mid-length impacts. The drilled hole greatly reduced the longitudinal strength while maintaining 95% of its lateral strength. This combination greatly reduces the potential for post snagging in a longitudinal hit, and thus reduces rollover potential, but maintains strength for redirection in a lateral impact (5). The top cable is located at a height of 28 inches (711 mm) above ground, with the middle and bottom located at 24 inches (610 mm) and 20 inches (508 mm) respectively. All posts in this system are spaced at 12.5 ft (3.81 m) between centers. Slack is provided in the cables during installation to accommodate cable length changes due to daily temperature fluctuations (5-7).

The wood post cable system end terminal has displayed inadequate impact performance in a 60 mph end-on crash test as it resulted in vehicle rollover. Numerous subsequent attempts to modify the wood post end terminal have proven unsuccessful in providing adequate cable anchorage without causing vehicle rollover when impacted near the terminal ends. Thus, the wood post system provides adequate redirective capability for mid-length impacts, but provides unacceptable performance for impacts near the terminal ends (5).

2.3 G1 Cable Guardrail System

The G1 cable guardrail system was developed with the intention of providing a crashworthy longitudinal cable barrier with improved end terminal impact safety. The G1 system is a three-strand, weak post cable guardrail system that utilizes S3x5.7 steel posts rather than wood posts. The end terminal for the G1 cable guardrail system was designed with the system cables sloping from normal cable height to ground level over a

distance of 24 ft (7.2 m), creating a very gradual slope. In order to reduce the likelihood of impacts on the end terminal portion of the barrier altogether, the anchor is also typically offset by 48 inches (1225 mm) from the front face of the barrier, flaring the terminal away from the roadway. The gradually sloping and flared cable of the G1 end terminal is intended to minimize vehicle rollover and sudden deceleration in an end-on impact (5,8-11). Refer to Figure 3 for an illustration of the G1 cable system and end terminal.

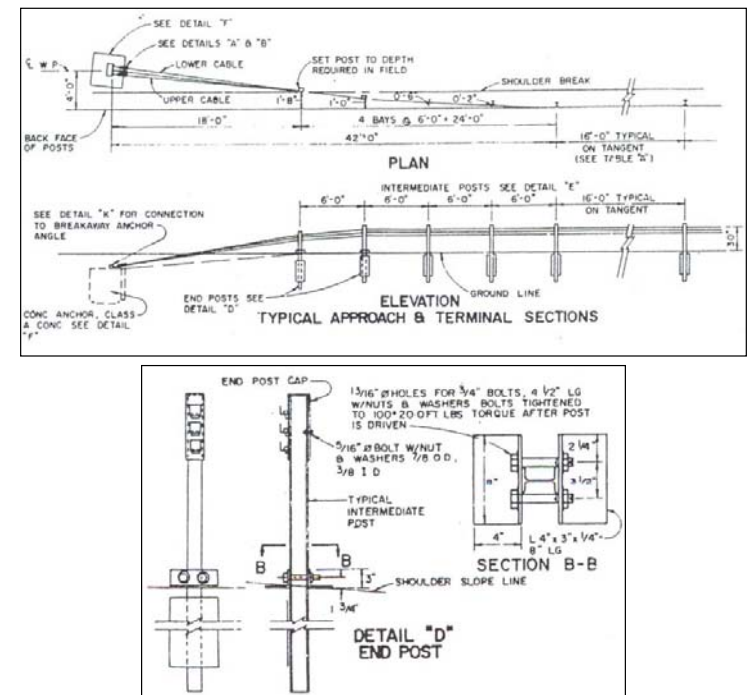


Figure 3. G1 Cable Guardrail System and End Terminal

As previously described, the cable end terminal is constructed by gradually sloping and flaring the cables from full system height to a rigid anchor point offset from the roadway. The first system post is mounted at a reduced height to accommodate the sloping of the cables. Both the first and second posts are fitted with end post brackets that act as soil bearing plates to resist the downward forces that result from the tension in the sloping cables. At the very end of the system where the sloping cables meet the ground, the cable ends are fitted into a slotted anchor assembly rigidly fixed to a concrete anchor block that is buried underground. For departure impacts, the slotted anchor assembly is intended to release the cable ends, thus allowing the impacting vehicle to pass through the end of the cable system without snagging (5.8-11).

The top cable height on the G1 system was originally 30 inches, with the middle and bottom cables at 27 and 24 inches respectively. However, it has been shown that cable heights of 27, 24, and 21 inches provides increased safety for occupants of small cars. Smaller cars typically have lower bumpers and wedge-shaped front ends that increase the potential for underride of the guardrail if the cables are too high (5.8,10-11). Thus, most current cable guardrail specifications indicate a top cable height of 27 inches. The steel posts most typically used to support the cables in the G1 cable system are I-beam shaped posts installed so the strong axis resists oblique mid-length impacts, with the weak axis offering minimal resistance to longitudinal impacts (5.9-11). Installing the posts in this manner will reduce the potential for snagging, and thus rollover, of impacting vehicles. The steel inline system posts are spaced at 16 feet (4.9 m) between centers, and the system utilizes spring compensators to maintain a minimum level of tension in the cables at all times (5.8-10).

The design of the G1 end terminal was intended to minimize the severity of end-on collisions. However, it has been shown with full-scale crash testing that the cables do not release with a departing vehicle impact just upstream of the anchor, often resulting in snagging and vehicle rollover (5.10). The result is a cable guardrail system that provides adequate system anchorage and redirection in mid-length collisions, but often results in snagging and/or vehicle rollover when impacts occur near the end terminals of the system (5.10-11).

2.4 New York DOT Cable Guardrail System

In order to improve the impact performance of the previously described cable guardrail end terminals, in 1990 the State of New York developed an improved three-strand cable system end terminal. The improved terminal design eliminated the gradually sloping cables as used in the G1 design. Rather, the first system post is installed a mere 27 inches (685 mm) away from the cable anchor bracket, with the cables turned down from normal cable height at a relatively sharp 45 degree angle. By increasing the cable turndown angle, the designers believed that the impact load would be transmitted more directly to the anchor bracket to achieve more reliable cable release, with a smaller resultant force imposed on the impact vehicle. A subsequent departure test revealed successful cable release with the new 45 degree cable turndown design. However, an end-on impact resulted in vehicle vaulting and rollover, and thus, the end post was redesigned to include a slip base (10). Refer to Figure 4 for illustrations of the New York cable system and end terminal.

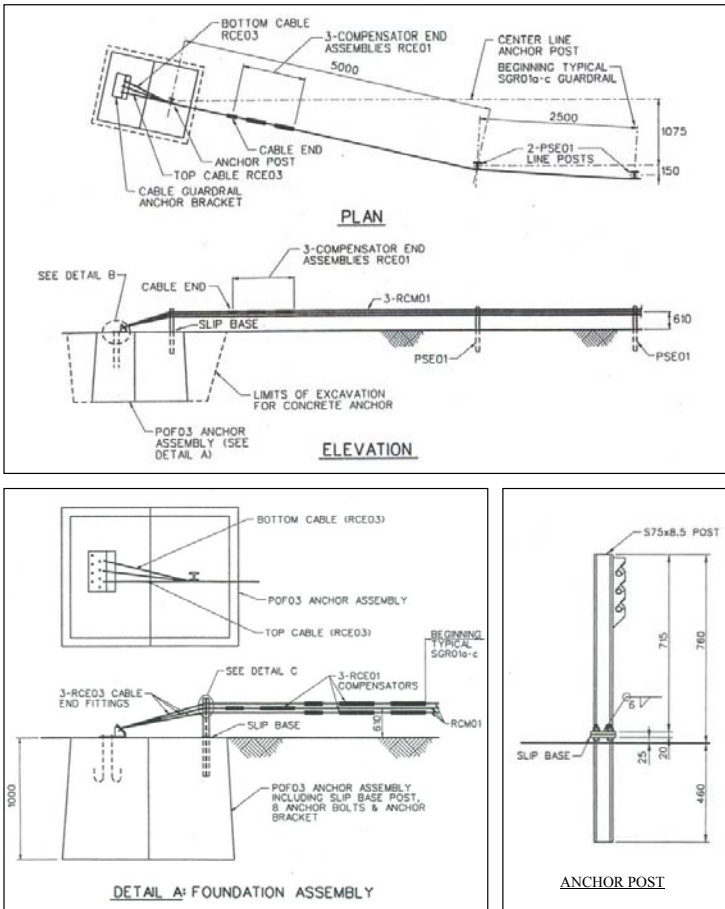


Figure 4. New York Cable Guardrail System and End Terminal

The final design of the New York cable guardrail system is a three-strand, weak post cable guardrail system that utilizes S3x5.7 steel posts with spacing of 16 feet (4.9 m). The steel I-beam shaped line posts are installed so the strong axis resists oblique

mid-length impacts, with the weak axis offering minimal resistance to longitudinal impacts, thus reducing the potential for snagging and rollover. The system has a top cable height of 27 inches, with the middle and lower cables at 24 and 21 inches respectively. Like the G1 cable system, spring compensators are used to maintain a minimum level of tension in the cables at all times (5.10.12-14).

In order to reduce the likelihood of an impact with the cable system end terminal altogether, the New York end terminal is flared away from the roadway over a distance of 24 ft (7.2 m), offsetting the anchor by 48 inches (1225 mm) from the guardrail face. Both the anchor bracket assembly and the first post are set into a concrete anchor block that is buried underground. The end post is embedded in the concrete anchor in order to resist the significant downward loads that result from the 45-degree cable turndown (5). Where the sloping cables meet the ground, the cable ends are fitted into slots in the anchor bracket assembly that are intended to allow the cable ends to release when impacted by a departing vehicle (5.10). As stated previously, a rectangular slip base is provided on the first post so it can release if impacted near the terminal end without snagging or vaulting the vehicle. The slip base is uni-directional in that it was designed to release from a longitudinal impact, but stay fixed to the anchor during a mid-length oblique impact. Cable clips are placed on the cables immediately downstream of the first post in order to prevent clockwise rotation of the post, and thus prevent slip base lock-up, in an end-on impact (5.10.12-14).

The New York cable system end terminal design has been shown to offer improved performance for impacts near the end terminal as compared to the G1 end terminal or the wood post end terminal. The new end terminal design was shown to

provide adequate impact performance in end-on, mid-length, and departure impacts using full-scale crash testing. Even though it was shown to be the best available cable guardrail end terminal at the time of its development, there is still some question as to whether the end terminal is capable of reliably making end-on impacts less severe (5,10).

2.5 MwRSF Cable Guardrail System

Although the cable system end terminal developed by the New York DOT was a significant improvement over pre-existing designs, improved impact safety was still desired. In 2000, the Midwest Roadside Safety Facility began development of a new crashworthy end terminal for the three-strand cable guardrail system. The design goal was to improve upon the New York end terminal design in order to assure the release of the pretensioned cables during end-on impacts, while maintaining departure and mid-length impact performance.

To accomplish the task of reliably disengaging the cable end fittings upon impact, the standard cable anchor bracket was modified to accommodate a cable release lever. The cable release lever is a mechanism that was designed to transmit the longitudinal force of the impacting vehicle to an upward force that lifts the cable end fittings from V-notches in the cable anchor bracket. Even though the system uses weak steel posts to support the cable, the end post is attached to a slip-base to further reduce its resistance to an impacting vehicle, very similar to the New York DOT design. Once the cable end fittings are dislodged from the anchor bracket, the tension in the cables is released, and the vehicle is allowed to pass through the system with minimal obstruction. Refer to Figures 5 and 6 for illustrations of the end terminal design (15).

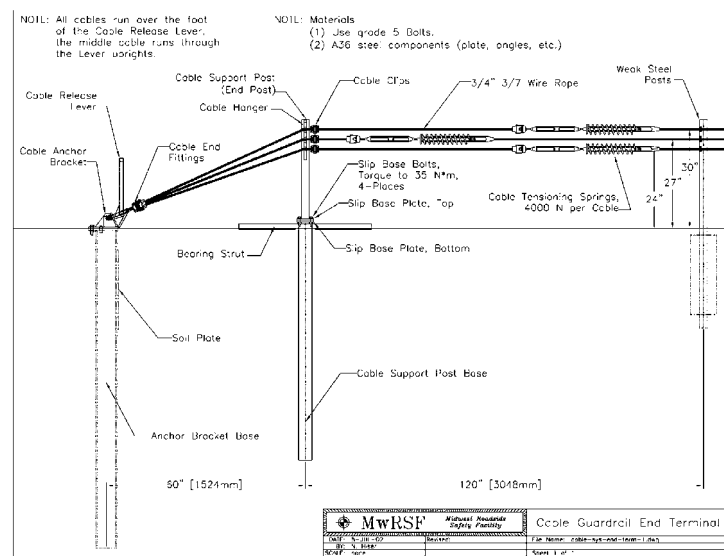


Figure 5. MwRSF Cable Guardrail System End Terminal



Figure 6. MwRSF Cable Guardrail System End Terminal, CT-2 Crash Test

The MwRSF cable guardrail system is a three-strand, weak post cable guardrail system that utilizes S3x5.7 steel posts with spacing of 16 feet (4.9 m). However, the distance between the end terminal slip base post and the first line post is 10 feet (3.1 m). The steel I-beam shaped line posts are installed so the strong axis resists oblique mid-length impacts, with the weak axis offering minimal resistance to longitudinal impacts, thus reducing the potential for snagging and rollover. The system has a top cable height of 30 inches, with the middle and lower cables at 27 and 24 inches respectively. Like both the G1 and New York cable systems, spring compensators are used to maintain a minimum level of tension in the cables at all times (15).

Unlike the New York end terminal, the MwRSF terminal is tangent with the remainder of the system. The anchor bracket is mounted on top of a 96 inch long W6x25 steel post with an attached 24"x24" soil plate to resist horizontal cable loads. The first post is mounted atop a W6x9 steel post with a bearing strut assembly to resist vertical loads from the turned down cables. Where the sloping cables meet the ground, the cable ends are fitted into slots in the anchor bracket assembly. These slots are intended to allow the cable ends to release if impacted near the terminal by a departing vehicle. As stated previously, a rectangular slip base is provided on the first post so it can release if impacted near the terminal end without snagging or vaulting the vehicle. The slip base is uni-directional in that it was designed to release from a longitudinal impact, but stay fixed to the anchor during a mid-length oblique impact. Cable clips are placed on the cables immediately downstream of the first post in order to prevent clockwise rotation of the post, and thus prevent slip base lock-up, in an end-on impact (15).

The MwRSF cable system design is intended to improve end terminal impact performance over the New York, G1, and wood post end terminals. At the time of this study, crash testing and approval of the cable system was not complete. However, two full scale crash tests, CT-1 and CT-2, have been conducted, and the results will be used as reference within this work.

3 SLIP BASE LITERATURE REVIEW

3.1 Slip Base Theory and Analytical Techniques

3.1.1 Slip Base Fundamentals

Slip base mechanisms are commonly used on roadside structures to provide a breakaway feature if the structure is impacted by an errant vehicle. All slip base designs incorporate two slip base flanges, an upper and lower, clamped together using standard bolts. The bolts reside in slots or grooves that allow the bolts to separate from the structure if the flanges move relative to each other. The primary failure mechanism of slip base structures is overcoming the friction that is present between the upper and lower slip base flanges. The slip base mechanism has proven to significantly reduce impact severity, and thus the theoretical and analytical slip base mechanism behavior is studied in greater detail herein.

3.1.1.1. Clamping Force

The primary variable that affects the breakaway force levels of a slip base mechanism is the clamping force exerted by the bolts. Slip base mechanisms typically utilize multiple bolts to clamp the slip base flanges together. The total clamping force, Nt , is thus the tensile force of a single bolt, N , multiplied by the number of bolts in the slip base mechanism (16). A tensile load is generated within a bolt as the bolt is torqued. Excessively high bolt tensions could easily result in degraded impact performance of a slip base mechanism (17). It is thus very important in all slip base designs to utilize the minimum bolt torque that will provide stability of the structure in order to minimize the slip base breakaway force (17).

3.1.1.2. Frictional Slip Force

When a slip base mechanism is impacted and breaks away, it is said to have activated. The base slip force is defined as the force required to activate the slip-base mechanism (16). In general, the slip force between two bodies sliding past one another is calculated using the common friction formulation:

$$F_f = \mu \cdot N \quad \text{Eqn 3.1}$$

Where F_f is the frictional slip force, μ is the coefficient of friction, and N is the normal force loading the bodies together. Note that it has been shown that the peak slip base activation force is almost directly proportional to mounting bolt torque, which supports the above formulation (17). Therefore, this is the starting point for theoretical analysis of slip base structures.

In reality, the activation force, or slip force, has also been shown to be dependent on a wide variety of factors, which are consequently significant design parameters for slip bases. These factors include bolt torque, surface treatment and finish, friction coefficient between the sliding surfaces, bolt diameter, and notch geometry (16). Slip base configurations also tend to be directional in nature. The impact angle relative to the slip base flange geometry has a direct influence on the base activation force. The slip force is also dependent on the height at which the vehicle contacts the pole above the slip plane (16).

In regards to surface finishes, it is important to note that control of the sliding surfaces in terms of coatings (paint, anodization, galvanization, etc.) plays an important role in slip base activation behavior (17). Because significant variations in slip base

friction have been reported, it is advisable to use caution when applying the relationship in equation 3.1 during specification of the slip base clamping loads (16).

Published values of steel on steel static friction range between 0.15 and 0.25. Published values of steel on steel dynamic friction range between 0.03 and 0.15, varying with velocity (18-19). In a previous study by Belter (19), a test was conducted to verify these frictional values. Two pieces of galvanized guardrail were used, one as the sliding surface, the other as a sled. Various masses were applied to the sled, and a force transducer was used to obtain the frictional slip force required to pull the weighted sled over the sliding surface. The normal force, friction force, and coefficient of friction were related by equation 3.1. The coefficient of static friction, calculated and averaged from the tests, was 0.179. The average coefficient of dynamic friction turned out to be 0.145. These empirical values agree reasonably well with the published values (19).

In addition to the frictional forces that develop during impact, many of the previously mentioned design parameters have been shown to contribute to a mechanical interlocking of slip base components. Specifically, the slip base notch geometry, impact angle, impact height, post deformation, bolt size, and surface characteristics all contribute to mechanical interlocking of the slip base flanges. The forces generated because of this mechanical interlocking must also be overcome before the slip base mechanism will activate (16). To calculate the base slip force, the following modified formulation has been proposed:

$$F_s = (\mu_e) \cdot N_t \quad \text{Eqn 3.2}$$

where F_s is the slip force, μ_e is the “effective” friction coefficient for a particular slip base, and N_t is the total clamping load generated by all the bolts. In addition to the

normal friction between sliding surfaces, the effective friction coefficient accounts for the forces generated by the various mechanical interactions previously described. However, because of the complexities of these interactions, it is difficult to theoretically derive the activation force of a slip base mechanism through analytical means (16).

In practice the effective friction coefficient of a three-bolt, triangular, multi-directional slip base under typical impact conditions has been shown to vary from approximately 0.49 to 0.83. A subsequent parameter study found that an effective friction coefficient of 0.5 gave the best correlation with measured values. A rectangular, uni-directional slip base has a different effective friction coefficient than the triangular slip base because of the basic differences in slip base geometry, bolt orientation, and notch geometry. The effective friction coefficient for a rectangular slip base was found to be approximately 0.26 (16).

3.1.1.3. Base Fracture Energy (BFE)

When a slip base mechanism is impacted by an errant vehicle, the slip force previously described translates into an energy dissipation at fracture or breakaway. The energy associated with failure of the slip base is commonly referred to as the base fracture energy, or BFE, which is the area under the slip force vs. slip distance curve. Therefore, the energy dissipated due to activation of the slip base can be calculated using the following formula:

$$BFE = (1/2) \cdot F_s \cdot \delta_s \quad \text{Eqn 3.3}$$

where BFE is the base fracture energy, F_s is the slip force, and δ_s is the slip distance (16). In the NCHRP Report No. 318 the force vs. deflection relationship associated with slip base structures was assumed to linearly decay over the slip distance as shown in the

Figure 7. It continues to say that slip distances of 1 to 3 inches are common depending on the particular slip base design (16).

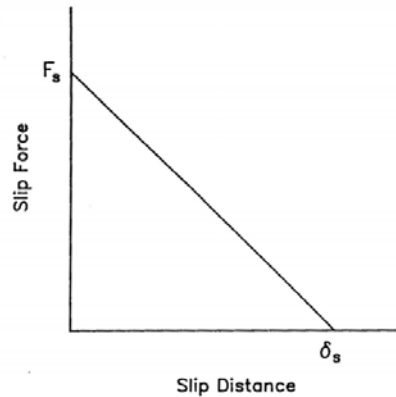


Figure 7. General Force vs. Deflection Relationship for Slip Base Mechanism (16)

Base fracture energy values can be utilized effectively when designing slip base mechanisms. For example, the BFE values determined from laboratory impact tests can be used as a measure of energy absorbed by the base in a full-scale collision. This allows a relatively simple laboratory test to substitute for full-scale vehicle crash tests in the evaluation of new concepts or designs (20). However, it is noted that the BFE value of any slip base under consideration should be determined by a reliable means, either by laboratory tests or proven analytical calculations (20). Due to the fact that the magnitude of the BFE values for slip base mechanisms can be used as a reasonable measure of impact severity, the lowest base fracture energy should be used which is consistent with static and wind strength requirements to hold the structure in place (20).

3.1.1.4. Momentum Transfer

Along with base fracture energy, a second analytical technique that is commonly used to evaluate impact severity of slip base structures is done by calculating the momentum transfer during impact. Although momentum transfer is not used directly in this study for analysis of slip base models, it is briefly explained here prior to presentation of test results in the following chapter.

The usefulness of momentum transfer, as applied to breakaway mechanisms, was outlined by Breaux and Morgan in Transportation Research Record No. 1258 (21). The principle of impulse and momentum is as follows:

$$m_1 \cdot v_1 + m_2 \cdot v_2 - \int F dt = m_1 \cdot v_1' + m_2 \cdot v_2'$$

where m_1 is the car mass, m_2 is mass of pole, v_1 and v_1' are the velocities of car prior to and after impact, v_2 and v_2' are the velocities of pole prior to and after impact, and the integral of $F \cdot dt$ is the total change in momentum (21). The principle of impulse and momentum can be reduced when the mass of the pole (m_2) relative to the mass of the car (m_1) is negligible, which yields:

$$m_1 \cdot v_1 - \int F dt = m_1 \cdot v_1'$$

By using the momentum equations above, or alternately using the more common conservation of energy principal, the final velocity of the vehicle can be found. The total velocity change of the impacting vehicle is a useful indicator of impact severity (21).

3.1.2. Quasi-Static Analysis

A quasi-static slip base analysis was conducted by Chisholm and Meczkowski et al, and the results were reported in FHWA-RD-78-204 (22). In this study the variables known to play a critical role in affecting peak slip loads, such as bolt clamping loads, striking height, and coefficient of friction between flanges were included in the analysis to obtain a better understanding of the effects these variables have on slip base behavior. The free body diagram used in the analysis is shown in Figure 8 (22). The equations derived from this analysis were plotted in such a way as to isolate individual variables of interest.

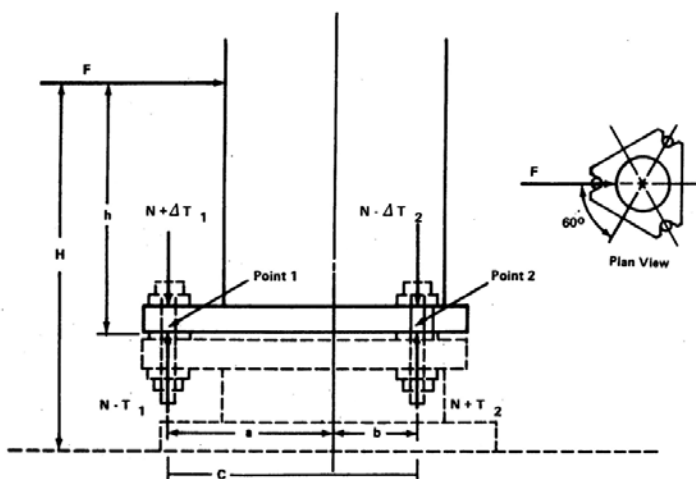


Figure 8. Slip Base Free Body Diagram (22)

The effect of friction coefficient on slip load is plotted in Figure 9. “Prior to separation the base resistance force is a constant. After separation (where separation is

defined as the lifting of the front of the flange connected to the pole away from the front of the base flange), the base resistance force rises linearly with increased impact force. Note that the point of intersection of these curves rapidly increases the resultant impact force. Variations of friction coefficient (f) between 0.15 and 0.20 for example result in a more than two-fold increase in impact force from 20 kips to 45 kips, for the specific geometry selected. This behavior creates concern over the potential long-range effects of faying surface corrosion and suggests that even small changes in friction coefficient due to corrosion may result in a slip base “locking up” under impact (22).”

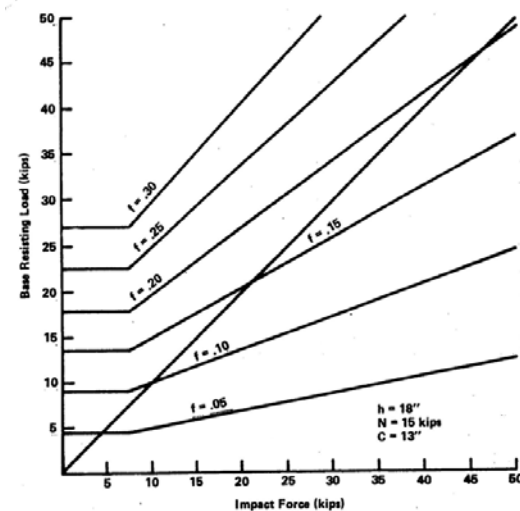


Figure 9. Base Resisting Force vs. Impact Force for Various Friction Coefficients (22)

Note that slip base “separation” in this analysis is defined as the lifting of the front of the top flange off of the front of the bottom flange. In other words, the moment acting on the slip plane due to the impact force causes the upper flange to rotate relative

to the lower flange. It is this relative rotation that is defined as “separation” in this analysis. For further clarification, if the flanges do not “separate” per this definition, they have remained parallel. It is evident from Figure 9 that slip bases that have “separated” are very sensitive to friction effects, displaying greatly increased breakaway force levels, which translates to greatly increased lock-up potential.

The effect of impact height on breakaway force levels is plotted in Figure 10. As impact height is varied from 12 to 18 inches, an increase in breakaway force of about 5 kips is observed. It is therefore concluded that the breakaway force level, or slip force, is not particularly sensitive to impact height within this range of striking heights (22).

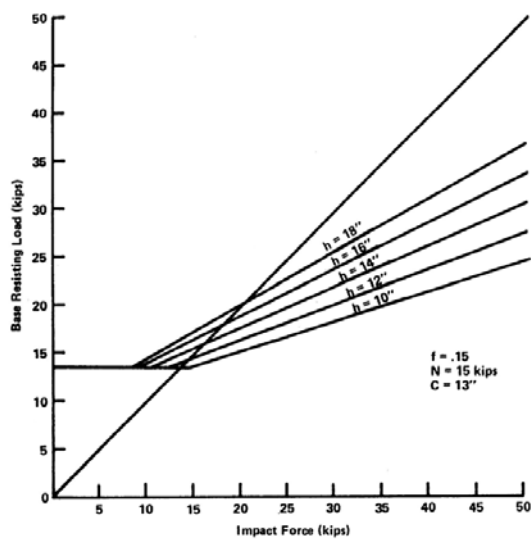


Figure 10. Base Resisting Force vs. Impact Force for Various Impact Heights (22)

The effect of initial bolt tension is plotted in Figure 11. As bolt preload increases from 10 to 20 kips, the breakaway force levels increase from 14 to 28 kips. It is therefore concluded that the breakaway force increases linearly with initial bolt load (22).

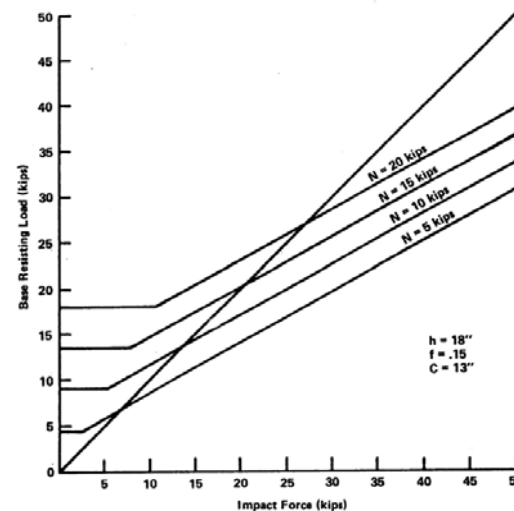


Figure 11. Base Resisting Force vs. Impact Force for Various Initial Bolt Loads (22)

The breakaway force level is plotted as a function of friction coefficient for two impact heights in Figure 12. At a friction coefficient of 0.15, a 12 inch impact height yields a breakaway force of 14 kips, while a 18 inch impact height yields a 20 kip breakaway force. At a friction coefficient of 0.20, a 12 inch impact height yields a breakaway force of 24 kips, while a 18 inch impact height yields a 48 kip breakaway force. It is therefore concluded that the breakaway force is higher for increased impact height and more sensitive to variations in friction coefficient at increased impact heights (22).

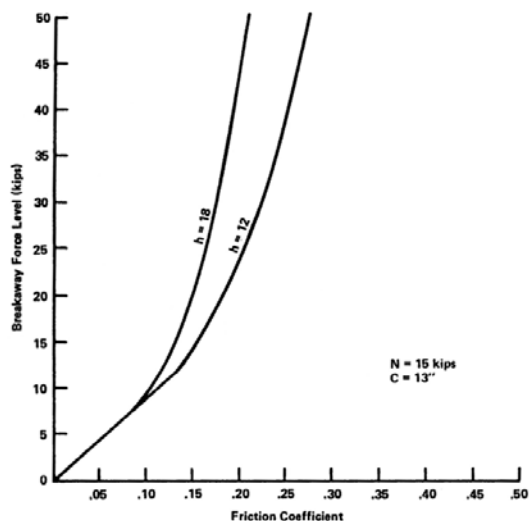


Figure 12. Breakaway Force vs. Friction Coefficient for Two Impact Heights (22)

The preceding quasi-static slip base analysis was conducted to gain insight into the variables that are known to affect slip base behavior. However, as in any analytically derived model, it has been developed with assumptions and simplifications which inherently limit its ability to capture reality. Therefore, it is advised to use it as a tool, but not a fool-proof validation technique.

3.1.3. Three-Step Dynamic Analysis

In NCHRP 318 a rigorous three-step dynamic procedure for analyzing slip base impacts was developed (16). The first phase is vehicle crush, during which energy is absorbed by the crushing vehicle. The crush force is assumed proportional to crush distance, and conservation of energy is used to calculate vehicle velocity at the end of phase one. Phase 2 is momentum transfer from the vehicle to the pole, and the velocity at

the end of phase two can be calculated using laws of conservation of linear and angular momentum. Phase three involves only the energy dissipated to the slip base activation, which was previously discussed as the base fracture energy. The law of conservation of energy can then be used to calculate the velocity at the end of phase 3 (16).

The equations associated with the velocity change in phases 1-3 were incorporated into a computer program for the purpose of developing design charts and conducting parametric studies of important variables for the improvement of slip base structures (16). This computer program is available to roadside engineers as a design and development tool for slip base structures in various applications.

A common concern about slip base mechanisms is the effect of impact height on the performance of the slip base mechanism. The program developed in the NCHRP 318 study accounts for the effect of impact height on the transfer of momentum; however, it does not account for slip force changes that may occur due to the added moment on the slip plane. As such, the results should be viewed as a lower bound on estimated changes in vehicular velocity. However, it should be noted that the program incorporates “effective” friction coefficients that have been empirically derived. The effective friction coefficient accounts for frictional slip behavior as well as other variables that increase slip forces as observed in slip base tests. Figure 13 shows the effect of impact height on change in velocity of the impacting vehicle, as calculated using the computer program. It can be seen in the plot that varying the effective bumper height within a rather narrow range of values results in significant vehicle velocity changes (16).

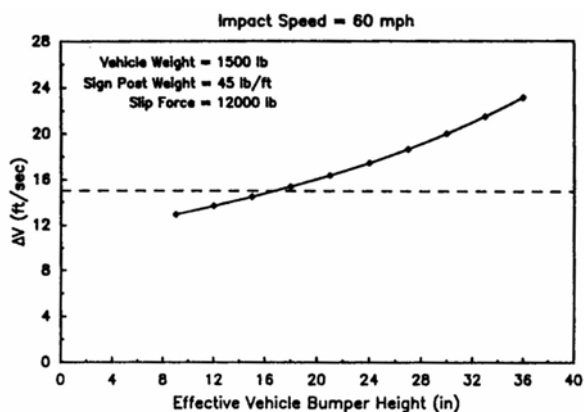


Figure 13. Change in Velocity vs. Impact Height, NCHRP 318 Program Output

Although the preceding three-step procedure could be a very beneficial technique when analyzing the severity of slip base impacts, they go beyond the scope of this work, and thus, the analytical equations will not be discussed in detail within this study. For anyone involved in slip base design for specific applications, reviewing the referenced documents and utilizing this procedure is highly recommended.

3.2 Slip Base Testing Results

Theoretical and analytical slip base behavior, as previously discussed, is useful to designers and developers only to the extent that the theoretical behavior mimics actual slip base behavior. Because every analytical model has limitations due to simplifications and assumptions, it is of utmost importance to verify or validate the model with physical testing. Sections 3.2.1 through 3.2.3 summarize previously conducted slip base testing results that are relevant to this study.

3.2.1 Slip Base Slip Force

In the NCHRP Report No. 318, the force vs. deflection relationship associated with slip base structures was assumed to linearly decay over the slip distance, as shown in the Figure 7. This linear assumption was no doubt based on previously obtained quasi-static slip base test results, which are shown in Figure 14 (17). At lower bolt loads the slip behavior was shown to decay linearly. With increased bolt loads the slip behavior displayed a somewhat concave force displacement curve. However, in terms of energy dissipated, or area under the curve, the slight concavity is of negligible concern, and it is concluded the linear assumption is valid. The test data in Figure 14 also illustrates that the peak slip force is almost directly proportional to mounting bolt torque (17).

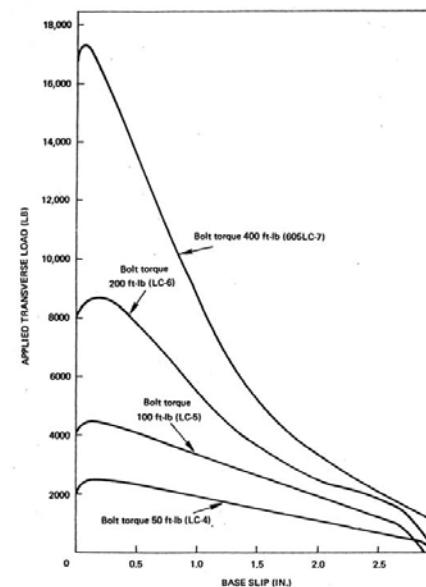


Figure 14. Quasi-static Force vs. Deflection Test Data for Slip Base Mechanism (17)

3.2.2 Slip Base “Lock-up”

The mechanical interlocking of slip base flanges is commonly referred to as slip base lockup. Because of the potential for increased impact severity due to slip base lockup, laboratory tests have been conducted to study this phenomenon. In 1978 the FHWA funded a laboratory study which used a pendulum impact facility to investigate slip base behavior, and the results were published in Report No. FHWA-RD-78-204 (22). A series of 13 pendulum impact tests were conducted on slip bases to investigate the critical parameters affecting the momentum transfer of the impacting body. The primary variables considered in this study were bolt preload, impact height, and washer stiffness (22).

The impact testing revealed that the impact height, and subsequent effects on pole deflection, greatly affect slip base performance. The momentum transfer of the impacting body was shown to be three to four times higher for poles with local elastic and plastic shaft deformation than for undeformed poles. These results strongly suggest that slip bases exhibit a fundamental instability when pole deformation in the contact zone is present. From the data it is inferred that the flanges remain parallel if the impact stresses do not cause the pole to deform or buckle, assuring low momentum change values. On the contrary, if significant pole deformation occurs, the flanges do not remain parallel, and the slip base tends to warp and lockup during impact. This warping behavior due to pole deformation is illustrated in Figure 15 (22). This same lockup effect will result from a moment at the slip plane due to, for example, a high impact, or a deflecting post. From the data obtained in this study, the FHWA made the following conclusion: “If pole deformation occurs, the flange bolts will be more heavily loaded due

to the instantaneous misalignment of the flange surfaces. It is this misalignment that causes the great increase in momentum transfer and eliminates the advantages of the slip base (22).”

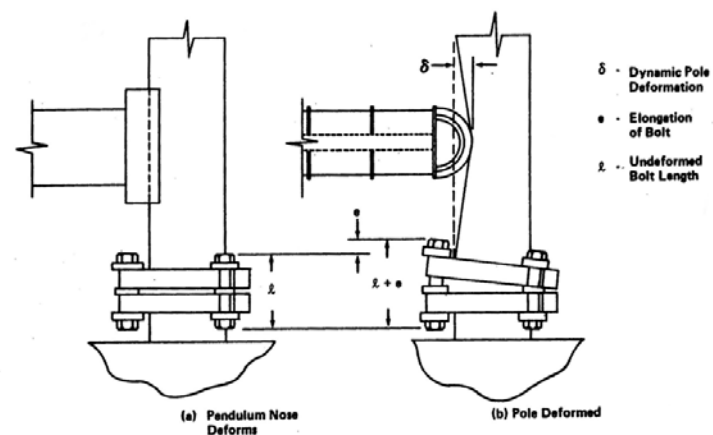


Figure 15. Slip Base Warpage and Lockup due to Pole Deformation (22)

Bolt clamping load was also shown to dramatically affect slip base performance. In one set of tests which used turn-of-the-nut tensioning method, there was a large discrepancy between two consecutive and identical tests. The first had a momentum transfer of 1,047 lb-sec, while the second had a momentum transfer of only 472 lb-sec. The lack of control of the clamping load is believed to have played a major role in the discrepancy. Washer deformation into the V-slots in the upper and lower flanges is also suspected to have caused some wedging with subsequent galling during the slipping process. It is believed both factors contributed to the significant scatter observed in the

momentum change data. In order to investigate these variables further, strain-gaged bolts for monitoring actual bolt preload and non-deformable washers were used. Subsequent tests verified that the use of these bolts, which allowed for closer control of slip base clamping forces, along with the non-deformable washers provided greater control over the peak slip force, and therefore, significantly reduced the scatter in the momentum transfer data (22).

3.2.3 Data Correlation with Analytical Techniques

A three step, dynamic slip base analysis was conducted in NCHRP 318, and was briefly explained in section 3.1.3. The resulting analytical equations and computer program were validated by comparing predicted velocity changes with results of actual pendulum impact tests and full-scale bogie tests documented in Report No. FHWA-RD-76-35 (16).

A comparison of the predicted and measured velocity changes for each of the three phases of impact for 5 pendulum impact tests is illustrated in Table 1. Based on the data comparison, it was concluded that the analytical procedure yielded reasonably accurate velocity change predictions for each of the 5 pendulum tests evaluated (16).

Test #	PHASE 1		PHASE 2		PHASE 3		TOTAL AV	
	Measured	Predicted	Measured	Predicted	Measured	Predicted	Measured	Predicted
201-204*	2.54**	1.24	1.70	1.30	0.60	0.70	4.84	3.54
4	N/A	0	2.54	2.78	--	0.47	2.99	3.25
10	--	5.38	2.49	2.78	--	1.61	9.39	9.30
9	--	2.02	2.49	2.61	--	0.88	5.55	5.51

* - Average of 4 tests
 ** - Nonlinear crushable nose used in this test

Table 1. Measured and Predicted Velocity Changes During Slip Base Impacts (ft/sec), Pendulum Test Data Correlation (16)

Similarly, a comparison of the predicted and measured velocity changes for six full-scale bogie tests is illustrated in Table 2. The predicted velocity changes were within ± 2 ft/sec of the average measured values, and thus, it was concluded that the model simulated the bogie crash tests with reasonably good accuracy (16).

Test #	Impact Speed (mph)	Change in Velocity (ft/sec)	
		Measured ^a	Predicted
B101	20	11.0 - 12.9	13.7
B102	40	14.2 - 16.4	15.6
B103	60	17.2 - 19.2	20.2
504	20	10.9 - 11.6	11.1
509 ^b	60	6.4 - 9.7	9.8
515	60	7.2 - 8.7	9.6

^a Range of values measured from film, speed trap, and accelerometers
^b Off-center impact

Table 2. Measured and Predicted Velocity Changes During Slip Base Impacts (ft/sec), Full-scale Bogie Test Data Correlation. (16)

As previously noted, following the validation of the three-step dynamic analysis procedure, the mathematical models were combined into a single comprehensive program for analysis of breakaway structures (16).

Conclusions were drawn from the existing slip base testing data. First and foremost concerns the instability of the slip base mechanism to separate when clamping force is not controlled and/or pole deformation occurs. The slip base lockup phenomenon is clearly a concern due to its ability to eliminate the effectiveness of the slip base mechanism in reducing impact severity. Slip base lockup results from mechanical interlocking of the slip base components that is dependent on a wide variety of variables.

It is these variables that must be thoroughly investigated before slip base behavior can be accurately predicted in a wide variety of circumstances.

The three-step dynamic procedure outlined in NCHRP 318 was shown to give reasonably accurate velocity change predictions when correlated with actual test data. This validated the concept that an “effective” friction coefficient can mathematically compensate for the mechanical interlocking of slip base components in controlled impact conditions. This effective friction coefficient takes into account frictional slip characteristics of the sliding surfaces, as well as the mechanical interlocking behavior that cannot be easily measured. However, in light of the FHWA test results that clearly verify the sensitivity of the slip base mechanism to lock-up, it is concluded that an inherent weakness in the three-step dynamic procedure is in fact the use of an “effective” friction coefficient. This conclusion implies that slight variations in impact conditions and slip base geometry may result in unacceptable impact behavior.

4 CLAMPING FORCES LITERATURE REVIEW

4.1 Importance of Joint Preload

In both theoretical and empirical investigations, slip base clamping forces were shown to be of significant importance in controlling the slip base activation forces, and thus impact severity. In fact, the key variable that controls the impact behavior of a slip base is the clamping force between the upper and lower flanges (17). It is therefore crucial to thoroughly investigate both commonly used and alternative slip base clamping methods.

Standard structural bolts are commonly used to supply slip base clamping forces. The bolt tensile loads are typically induced during assembly by providing a specified torque. Because bolt tension has been referred to as the single most critical factor for the safe operation of slip base mechanisms, control of the torque-tension relationship is a prerequisite for control of slip base BFE levels (17-23).

Clamping loads are not only important for slip base impact behavior, but also must maintain static structural integrity over time. Through extensive experimental studies and analytical modeling, Edwards et al. showed that if the applied tension is above specified levels, the slip base joint will not fail under impact. On the other hand, if the applied tension in the bolt is below the specified levels, the joint may not withstand the static structural requirements of the application. For example, a slip base joint used on a sign post may loosen over time and collapse during a wind storm. Therefore, it was concluded that initial bolt tension is critical, and that it be maintained throughout the life of the slip base structure (24).

In general, sufficient bolt preload is essential in critical bolted joints in order to assure the joint will not separate and fail under an applied loading. A means of ensuring a safe joint is to specify a bolt preload that is higher than the externally applied load. Therefore, it is critical to know the actual external loads acting on the joint, specify an appropriate preload, and finally to consistently control the tensile loads in the bolts (25).

4.2. Preload Control Methods

Because of the importance for preload control in many joints, including slip bases, bolt preload is often monitored or measured using various techniques. All preload measurement techniques are not equal, and experience has proven that accurate determination of the bolt tensile load produced during tightening is a difficult task (26).

4.2.1. Bolt Strain Measurement

The only absolutely reliable method known for controlling bolt tensile loads is by directly measuring bolt strain (22). If the overall length of the bolt is measured before and after assembly, the bolt elongation due to the preload is known. The bolt preload can then be computed using the formula:

$$\delta = (F_i \cdot L) / (A \cdot E). \quad \text{Eqn. 4.1}$$

where δ is the bolt elongation, F_i is the preload, L is the strained portion of the bolt shaft, A is the tensile area, and E is the elastic modulus of the bolt material (25). Bolt length can be measured before and after tightening with a micrometer, with axial strain gages within the bolt shaft, or with more costly ultrasonic equipment which is used primarily in production settings (26).

4.2.2. Torque Measurement

Often times it is not possible or practical to measure bolt elongation. In such cases, torquing methods can be used to estimate the bolt preload, and the torque wrench is undoubtedly the most common method used in practice (25-26). In fact, the torque wrench has proven to be the most cost effective way to estimate bolt preload in high production environments (26). Another common preload method, although more crude, is the "turn-of-the-nut" method in which nut rotation is monitored (26). In either case, variation in the preload of bolts has plagued designers for years due to inherent inconsistencies in the torque-tension relationship. Because of the practical use of the torque wrench, a more in-depth investigation of the torque-tension relation was conducted in the Chapter 4.3.

4.2.3. Alternate Preload Control Methods

Torquing methods often prove inadequate for proper control of critical joints. For slip base applications, three alternate preloading techniques have been suggested. These methods are depicted in Figure 16 (17).

The first method consists of using elastic compression washers, often referred to as Belleville washers, to control the clamping load. These washers are conical in shape and are designed to elastically deflect at a predetermined load. By simply controlling the deflection of the spring washers, a desired preload can be achieved (17).

A second type of washer is the load-calibrated crushable washer designed to buckle or collapse plastically at a predetermined axial load. By applying just enough torque to cause the upper portion of the crushable washer to contact the lower portion of the washer, a controlled axial crush load is achieved. Both the Belleville washer and the

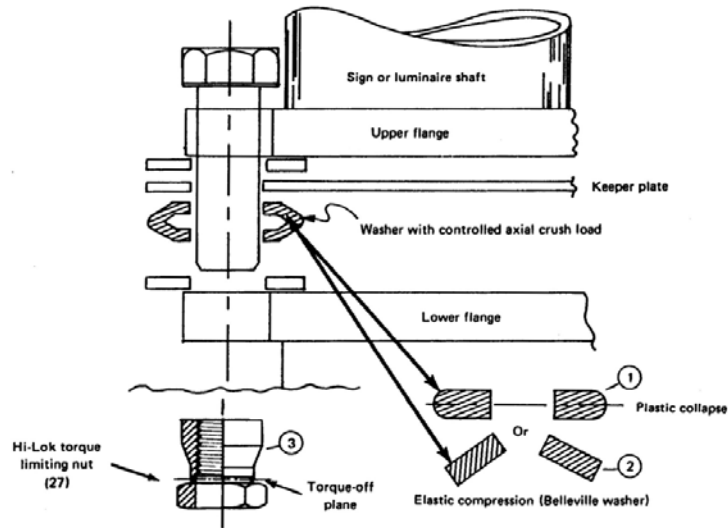


Figure 16. Alternate Methods of Controlling Slip Base Clamping Forces (17)

plastic collapse washer eliminate the dependence on unreliable torque tension readings, and thus, good control over breakaway energy levels can be achieved (17).

The third and final preload control method is the torque-limiting nut. The Hi-Lok torque limiting nut is shown in Figure 16. These devices have two distinct sections; the threaded section and the hex nut section. Separating the two sections is a thin walled area referred to as the torque-off plane. At a predetermined torque during installation, the hex nut section twists off and fails through the torque-off plane, and the threaded section remains on the bolt, preloaded at the failure torque. As in the torque wrench method, these nuts rely on the torque-tension relationship of the bolt, which is often unreliable.

However, torque-limiting nuts may provide improved load control in some situations (17, 22).

4.2.3.1. Belleville Washer Testing

The Belleville washer was used in a long-term investigation to develop a more accurate and reliable method to induce slip base clamping forces, as well as to ensure the tension will remain constant over the life of the connection (24). There were 7 test sites which used Belleville washers to tension the slip base bolts, and 7 additional test sites used traditional torquing methods for preload control. In all cases the requirement was to maintain a bolt tension between 10,680 N (2400 lbf) and 16,020 N (3600 lbf). The bolt tensions in all cases were measured with strain gages, and monitored weekly over a period of 14 months (24).

In 5 out of 7 sites, the Belleville springs were able to maintain the proper tension in the bolts for extended periods of time, as shown in Figure 17 (24). In 6 out of 7 of the sites using standard torquing techniques, the bolt tension failed to remain in the allowable range. Though all were initially torqued to FDOT specifications, the bolts were initially undertensioned in 5 out of the 7 cases. The sixth bolt loosened over time and fell under the required minimum tension, as shown in Figure 18 (24).

The results of this investigation indicated that Belleville washers could be effectively used to measure and maintain the tension in slip base bolts. By installing the Belleville washers to a prescribed deflection, the desired load was attained. The main advantage of this technique is that it eliminated the inconsistencies associated with torque measurements (24).

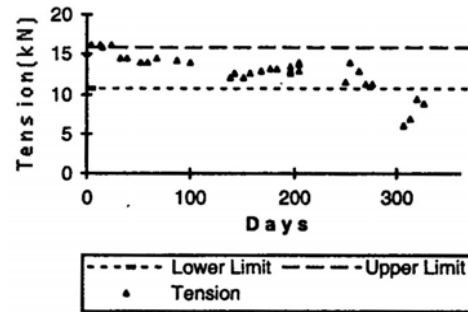


Figure 17. Bolt Tension Using Belleville Springs (24)

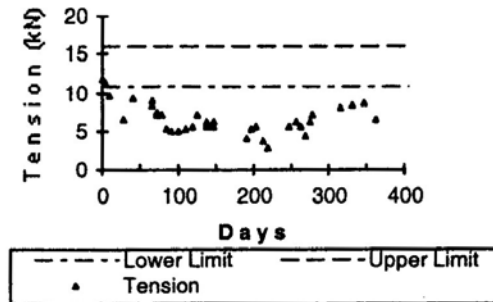


Figure 18. Bolt Tension Using Standard Torquing Method (24)

4.3. The Torque-Tension Relationship

4.3.1 Analytical Torque-Tension Relationship

The torque-tension relationship for typical bolts is derived from analysis of the power screw. The torque-load relationship for a power screw is derived by summing equilibrium forces acting at the mean diameter of a square shaped helical power screw thread. When summing forces it becomes clear that the total torque required to lift the load is generated by three reaction torques. These reaction torques are caused by the inclined planes of threads, friction between thread surfaces, and the frictional resistance between the face of the collar and the stationary surface (26). The three reaction torques appear as two main terms in the torque coefficient K . The first term accounts for the lifting of the load and overcoming of the thread friction. The second term accounts for the friction between the collar and the stationary piece. The equation is then modified to account for the thread angle that is present in typical screw threads, as shown in equation 4.3 (25).

$$T = F \cdot K, \text{ where} \quad \text{Eqn. 4.2}$$

$$K := \frac{D_m}{2} \left[\frac{(\mu_1 \cdot \sec(\beta) + \tan(\alpha))}{(1 - \mu_1 \cdot \sec(\beta) \cdot \tan(\alpha))} \right] + \frac{\mu_2}{2} \cdot (D_c) \quad \text{Eqn. 4.3}$$

T = applied torque

F = axial load

K = torque coefficient

D_m = mean thread diameter

D_c = mean collar diameter

μ_1 = thread friction coefficient

μ_2 = collar/bolt head friction coefficient

β = one half the thread angle

α = lead angle of thread = $\tan(\text{pitch}/(\pi \cdot D_m))$

An alternate derivation of the torque coefficient K is shown in equation 4.4. This technique yields a different second term, which accounts for the friction between the collar and the stationary piece. In this derivation the second term is based on a method used to compute torque requirements to overcome friction between disk clutches (25,27). This derivation results in a more flexible final equation, as it allows for variations in the geometry of the bolted joint. The following alternate formulation has been employed for many years with significant success in a high production environment.

$$K := \frac{Dm}{2} \left[\frac{(\mu_1 \cdot \sec(\beta) + \tan(\alpha))}{(1 - \mu_1 \cdot \sec(\beta) \cdot \tan(\alpha))} \right] + \frac{\mu_2}{3} \left[\frac{(D_o^3 - D_i^3)}{(D_o^2 - D_i^2)} \right] \quad \text{Eqn. 4.4}$$

D_o = outside bolt head diameter
 D_i = clearance/hole diameter

The previous equations are simplified when applied to the standard geometry of hex head bolts. The result, as shown in equations 4.5 and 4.6, is the common form used for most bolt torque-tension applications (18,25-26,28-31,34-35).

$$T = K \cdot F \cdot D \quad \text{Eqn. 4.5}$$

$$K := \frac{Dm}{2 \cdot D} \left[\frac{(\mu_1 \cdot \sec(\beta) + \tan(\alpha))}{(1 - \mu_1 \cdot \sec(\beta) \cdot \tan(\alpha))} \right] + 0.625 \cdot \mu_2 \quad \text{Eqn. 4.6}$$

T=applied torque
 K=torque coefficient
 F=induced preload
 D=nominal bolt diameter

It is important to note that equations 4.5 and 4.6 are applicable only to standard geometry of hexagonal head bolts. For other joint geometry torquing needs, the use of equation 4.2 along with either of equations 4.3 or 4.4 is required.

The torque coefficient K combines the effect of the frictional surfaces and the geometry of the bolt head and thread profile (26). The value of K is highly susceptible to friction coefficients μ_1 and μ_2 , as it is clear that friction constitutes a major portion of its final value. Thus, the torque coefficient varies with different finishes, platings, and lubricant coatings normally found with standard fasteners (28). The usefulness of the equation for practical application is dependent on the user's ability to properly determine the surface conditions (29). Table 3 displays various K values computed from equation 4.6 for common surface finishes of standard bolts.

Surface Condition	K
Non-plated, black finish	0.30
As received, steel	0.20
Zinc-plated	0.20
Unlubricated, dry	0.20
Cad-plated	0.16 - 0.19
Lubricated	0.15 - 0.18
Well lubricated, not smooth	0.13 - 0.15
Moly grease	0.14
Fel-Pro 65A	0.13
Petroleum, light oil	0.12
Anti-seize	0.12
Well lubricated, smooth surface	0.10

Table 3. Torque Coefficient Values for Threaded Fasteners (18,26,28,30-31,34-35).

The theoretical analysis and resulting equation 4.5 suggest that there is a linear relationship between the applied torque and the developed preload for a given fastener geometry (26). It also suggests that the preload is inversely proportional to K (26). Theoretically, for a given bolt geometry and applied torque, the preload can vary by a factor of three. This indicates the extreme sensitivity of bolt preload to friction.

A friction coefficient of 0.15 yields a K value of 0.20. (18,30) For many non-critical bolt preload calculations 0.15 can be used as a rough estimate for both μ_1 and μ_2 .

The value of 0.15 is the friction coefficient for a typical dry surface of a steel fastener as delivered from the manufacturer. (18,26) However, the actual coefficient of friction depends upon smoothness, accuracy, and degree of lubrication of the thread surface. In one study, deliberate oiling of the nut and bolt during tightening was shown to reduce the value of K by as much as 50% (31).

A third and final analytical technique is outlined in Highway Research Record 222. It states the following equation can be used to calculate bolt preload for torque wrench tightening (23).

$$N = K_t * T \quad \text{Eqn. 4.7}$$

where N is the bolt preload, T is the applied torque, and K_t is defined for specific bolt sizes as shown in Table 4.

Nominal Bolt Size	K _t (1/in)
1/2-13 UNC	4.940
5/8-11 UNC	3.870
3/4-10 UNC	3.185

Table 4. K_t Values Defined in Highway Research Record 222 (23)

Although it is not clearly stated, it is assumed the K_t values are empirically derived. As in the previous analytical techniques, there is a linear relation between bolt preload and applied torque. Using the similar equation form, the K_t values defined in Table 4 were compared to the K values in Table 3. It was found that the K_t values in Table 4 correspond to a K value of about 0.41. Plugging this K value into equation 4.6 yields friction coefficients of about 0.33, which is considerably higher than commonly published values (18,26). Intuitively, unreasonably high friction coefficients yield unreasonably low bolt preload values.

4.3.2. Empirical Torque-Tension Relationship

Published results of numerous torque-tension tests, and the subsequent statistical analysis of the data, has provided some insight into the distribution of the torque-tension relation. The preload of identical lubricated and unlubricated bolts was determined using strain gaged bolts. The resulting data indicated that both groups had about the same mean preload of 34 kN. However, the standard deviation of the unlubricated bolts was about 4.9 kN, which is about 15% of the mean, while the lubricated bolts had a standard deviation of 3 kN, or about 9% of the mean. This data revealed a substantial reduction in data scatter with the lubricated bolts. Both of these deviations are quite large, and thus emphasize the necessity for quality-control procedures to control bolt preload (25).

Another test procedure conducted repeated torque-tension tests on the same nut and bolt combination. The data revealed that continued use (reuse) of the same bolt-nut assembly results in lower preload values for the same torque values in as few as five installations. Further cycles revealed preload loss for the same fastener combination varied as much as 30-60% after 10 consecutive cycles. Figure 19 displays the test data (28).

The need for actual torque-tension data for specific applications has resulted in many sources of published data that has been empirically derived. Typically torque-tension data is obtained experimentally using bolts with strain gages installed down the axis of the bolt shaft. This allows for bolt shaft deflection to be translated into bolt preload. One extensive source of experimental torque-tension data was obtained and published by Union Metal. This data is presented in graphical form in Figure 20, and also in Figures 21, 22, and 23 (17).

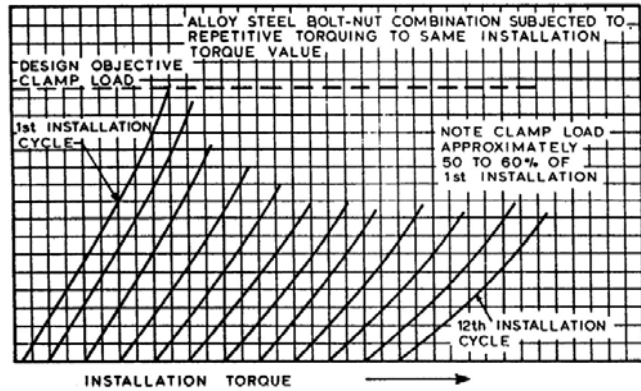


Figure 19. Torque-tension Curves Showing Effect of Repetitive Installation (28)

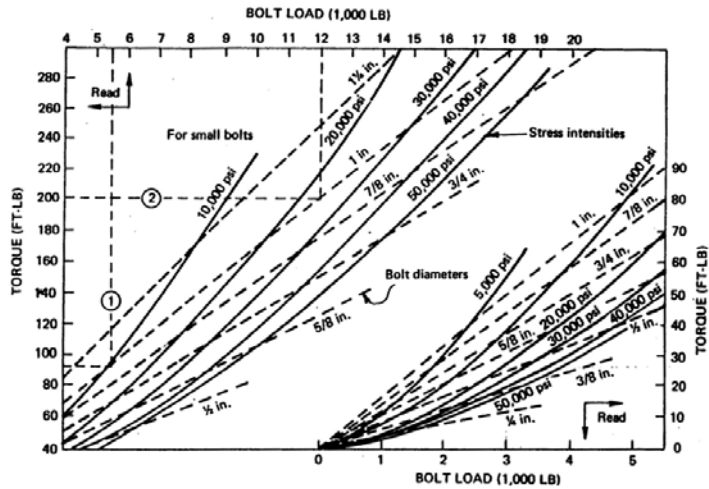


Figure 20. Union Metal Test Data, Applied Torque vs. Bolt Tension (17)

In another test, the Utah Department of Transportation obtained the torque-tension relationship for 1.00-8 UNC bolts. The preload data was read directly off of a force transducer, and was then correlated with the applied torque as measured with a torque transducer. This data is displayed in Figure 21 (32).

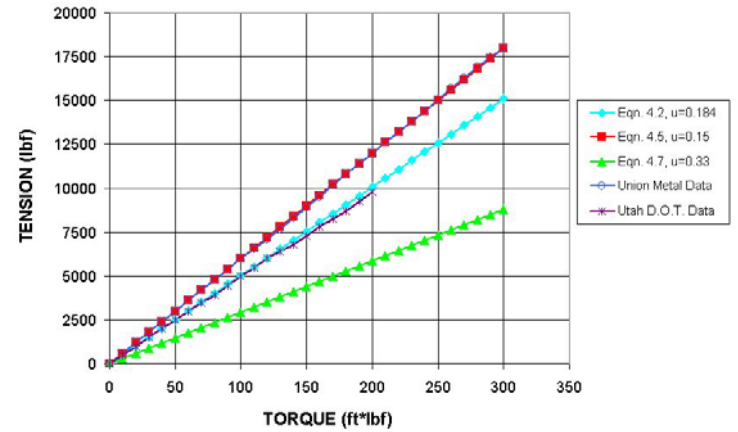


Figure 21. Torque-tension Data Correlation, 1.00-8 UNC Bolt

In a third test procedure, Belter obtained the torque-tension relation for 0.625-11 UNC bolts. In this test, a cylindrical force transducer was placed in compression as the bolt was loaded, and again the torque was measured with a torque transducer. The results of this testing are displayed in Figure 22 (19).

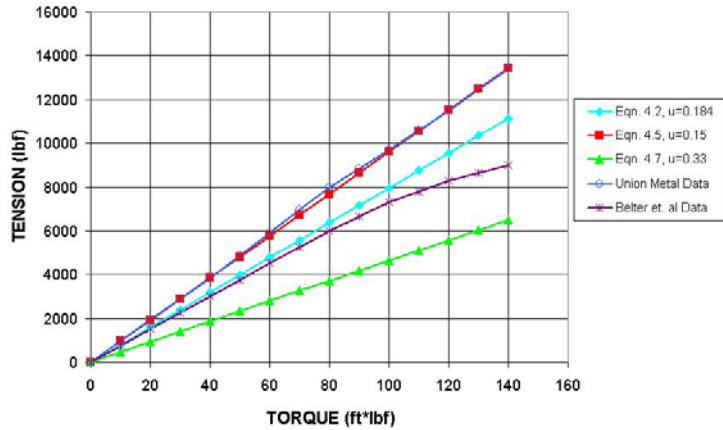


Figure 22. Torque-tension Data Correlation, 0.625-11 UNC Bolt

4.3.2.1. Obtaining Torque-Tension Data using Pressure Paper

Although torque-tension data was not produced formally for this study due to financial constraints, an experimental technique for monitoring bolt preload was investigated. A pressure sensitive paper, called Pressurex, was placed over the shank of a 1/2-13UNC bolt, under the head of the washer, and against the fixed bearing surface. The bolt was then torqued to 310 in-lbf (35 N-m, 25.8 ft-lbf) using a calibrated torque wrench. When the pressure paper is subjected to a load, a permanent visual colorized representation of the pressure variation across the contact area is produced. The color intensity can be directly correlated with the level of pressure applied. The pressure paper sample was then analyzed by Sensor Products, Inc. using the Topaque optical measurement system. This system is used to accurately measure the pressure distribution, the total area of contact, and the resulting net load. Sensor Products, Inc. claims ±1% accuracy when using the Topaque system (33). Only one torque-tension measurement

was taken due to cost prohibitive analysis. Optical analysis revealed a total bolt load of 2232 lbf. This single data point was plotted in Figure 23.

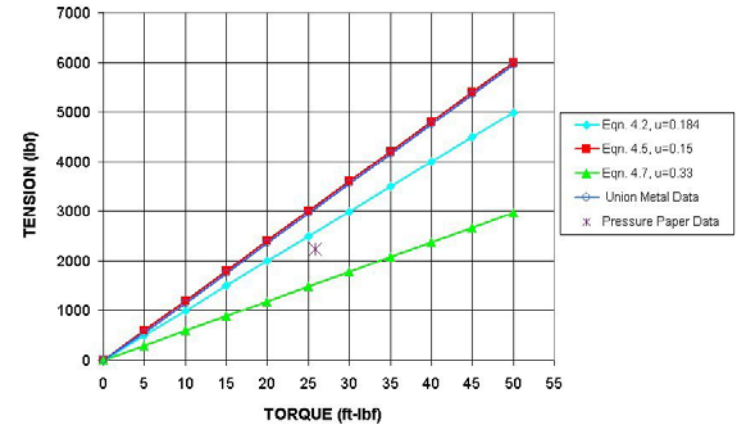


Figure 23. Torque-tension Data Correlation, 0.500-13 UNC Bolt

4.3.3. Analytical-Empirical Data Correlation

For purpose of illustrating the variation inherent in the torque-tension relationship, the three analytical techniques described by equations 4.2, 4.5, and 4.7 are plotted on the same graph as the empirical torque-tension data described above. For this purpose, three bolt sizes were chosen due to the availability of empirical data, and the applicability to slip base structures. Figure 21 displays the torque-tension data correlation for a 1.00-8 UNC bolt. Figure 22 displays the torque-tension data correlation for a 0.625-11 UNC bolt. Figure 23 displays the torque-tension data correlation for a 0.500-13 UNC bolt.

It is clear that there is significant variation within the various analytical and empirical data. The range of preload values is shown to vary by about a factor of two.

This extreme variation undoubtedly results from the erroneous identification of frictional coefficients between bolt threads and clamping surfaces. The data correlation clearly illustrates the problematic nature of using the torque-tension relationship for controlling bolt preload.

4.3.4. Using the Torque-Tension Relationship In Practice

Although obtaining repeatable torque-tension control in bolts has plagued designers for decades, specifying torque values remains the most frequently utilized method of controlling bolt preload (17). With the widespread and longstanding use of this method, and discovery of the potential pitfalls, much information has been passed along concerning practical usage. For a designer it is of utmost importance to fully understand the problem in order to apply it appropriately in specific applications, and thus, published observations and recommendations are summarized herein.

The torque wrench is commonly used as a method to indirectly measure bolt tension. Tests have indicated that the torque-tension relationship for structural bolts may vary by as much as 40-45% when using a torque wrench. (24,34) With special care and control procedures, bolt preload can reasonably be controlled within 15-30% (18). It is important to recognize that the gauge reading on a torque wrench measures nothing more than the resistance of a turning bolt. Because the torque-tension relationship is not a direct correlation, the reading means absolutely nothing unless the corresponding tension is measured directly by a reliable means (29).

The variable that eliminates a direct torque-tension correlation is friction. Friction plays a significant role in final bolt preload (29). It has been fairly well established that as much as 90% of the applied torque is used in overcoming frictional resistance in the

use of threaded fasteners (28). Approximately 50-60% of the torque is consumed by overcoming the friction under the bolt head, 30-40% is due to friction between the mating threads, and only about 10% of the applied torque is providing energy to elongate the bolt and produce preload. (29,34)

Frictional forces on bolts, and the associated resisting torques, vary considerably depending on materials, surfaces finishes, lubrication, cleanliness, and geometrical thread fit. (18,30,34) These variables have been shown to produce variation in bolt tension in certain cases as high as 10:1 (35). Because lubrication dramatically reduces friction, lubrication of bolts typically results in much higher preload values for a given torque. If the parts are lubricated, it is advised to conduct tests in order to avoid overstressing the bolts (30).

The torquing of a bolt or nut imparts a torsional shear stress to the bolt shaft, along with the tensile stress of elongation. (18,25,30) If there is considerable thread friction, a substantial applied torque may be needed for bolt rotation. In some cases the torsional stresses can be so great that yielding occurs at relatively low values of preload (18). If torsional yielding does not occur, the torsional stress is held only by the friction between the bolt head and stationary surface (25). With time the bolt usually unwinds and relaxes, relieving the torsional stress and slightly lowering the bolt tension (18,25,30). Thus, as a general rule, a bolt will either fail during the torquing process or not at all (25).

As time passes, bolts tend to lose additional preload (24). The elastic deflection that produces bolt tension may be a hundredth of a millimeter or less. Bolt preload can be lost due to differential expansion and contraction from temperature variations,

vibrations, and external cyclic loads (24). Creep within the joint, flattening of minute high spots on the surfaces, wear or corrosion of the mating surfaces, and squeezing out of surface films will also potentially result in a loss of tension. Tests have shown that a typical bolted joint loses about 5% of initial tension within a few minutes, and an additional 5% within a few weeks (18).

It is concluded that the relationship between torque and tension is highly variable and must be used with caution (34). The accuracy of the torque wrench method to achieve tensile preload is seriously limited by variations in the friction coefficient of the fastener system. (18,28) If the torque wrench method is used, special care must be exercised if consistent results are to be achieved (35). Above all, do not rely too much on a torque wrench reading. It may a good indicator of preload, but it certainly does not determine preload. Actual bolt elongation should be used to measure bolt tension whenever high reliability is a requirement of the design (25).

5 EXISTING SLIP BASE MODELING IN LS-DYNA

The widespread use of the slip base mechanism on roadside breakaway structures has produced a need for advanced development and analysis tools. Prior to this study, LS-DYNA has been used in two separate cases to model specific slip base mechanisms. The first study was conducted by NCAC in which a 3-inch triangular sign post slip base was modeled. The Texas Transportation Institute conducted the second study in which the Arizona DOT triangular luminaire slip base was modeled. It was the objective of this chapter to investigate and provide detailed model documentation for both LS-DYNA slip base models, including preload and slip behavior when impacted by a rigid cylinder. The intent was to evaluate the modeling techniques and assumptions for use in developing a detailed slip base model for the MwRSF three-strand cable system end terminal.

5.1 NCAC Oregon 3x3 Triangular Sign Post Slip Base

5.1.1 Model History:

- a) HyperMesh Model: none
- b) Original Dyna Model: **3x3_Slip_V03.key**, download from NCAC website ([36](#)).
- c) Working Dyna Model: **3x3_Slip_V03-cylinder-impact.k**
 - i) Modified by Dr.Reid, 3-Sept02.
 - ii) Add cylindrical contact entity for impact simulation.
 - iii) Modify some control/output options.
 - iv) Change density of material 24 (ground) to something realistic.
- d) Modified Dyna Model: **3x3-reid-mod1.k**
 - i) Modified by N. Hiser 5-Sept-02
 - ii) Add cross sections through lower flange and stub.
 - iii) Add force transducers to flanges, keeper plate, post, top washers.
 - iv) Start impact cylinder motion at 0.003 seconds to verify dynamic relaxation.

5.1.2 Model Description:

- a) Units: tonne (1000 kg), mm, s, N, MPa, N-mm
- b) Geometry: 3-bolt, triangular slip base, with keeper plate. Refer to Figure 24.
- c) Material Definitions:
 - i) All washers are *MAT_RIGID.
 - ii) Ground is *MAT_RIGID, single shell element.
 - iii) Bolt shafts are *MAT_PIECEWISE_LINEAR_PLASTICITY.
 - iv) Keeper plate is *MAT_PIECEWISE_LINEAR_PLASTICITY.
 - v) Sign posts are *MAT_PIECEWISE_LINEAR_PLASTICITY.
 - vi) All other slip base and sign components are *MAT_ELASTIC.
- d) Bolt Clamping Load:
 - i) Modeled using 4 discrete spring elements per bolt, attached to the rigid upper washers and lower washers. See Figure 25.
 - ii) Spring material definition is *MAT_SPRING_GENERAL_NONLINEAR. Load curve is shown in Figure 26A.
 - iii) Initial offset of spring elements is not defined. Rather, load curve is translated to the left so that load exists at zero offset. See Figure 26B.
 - iv) Translational joints are defined between the rigid upper washers and the rigid lower washers, along the axis of the bolt shafts. The bolt shaft itself is a deformable body which is attached to the rigid lower washer. Refer to Figure 25.
 - v) Dynamic relaxation is specified within spring load curves to preload bolts.

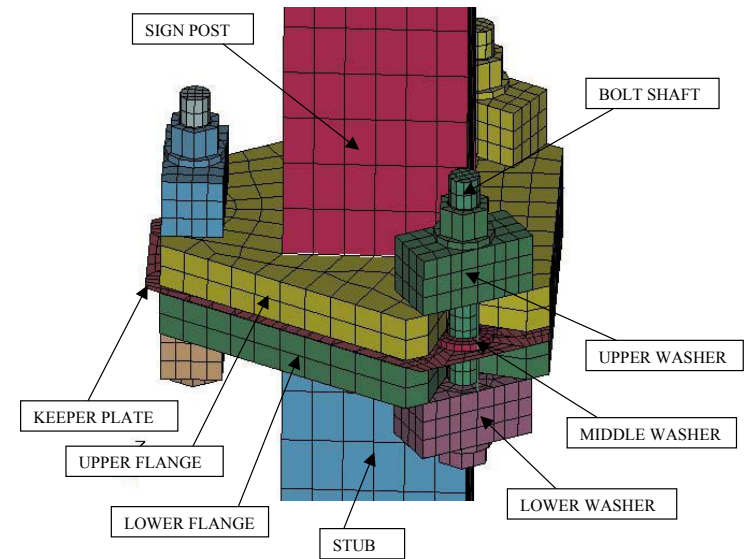


Figure 24. NCAC Oregon 3x3 Slip Base Model Geometry

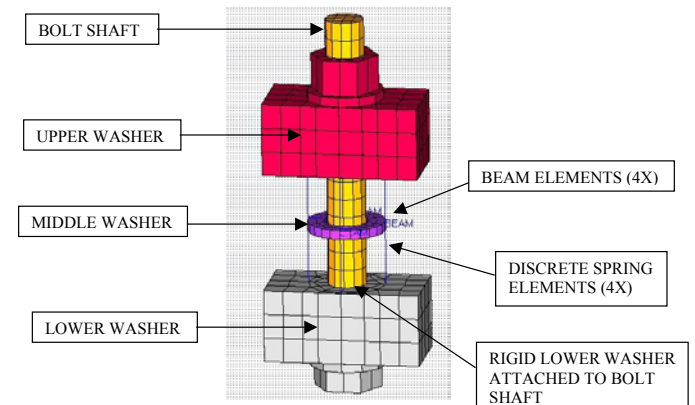


Figure 25. Bolted Joint Model, NCAC Oregon 3x3 Slip Base

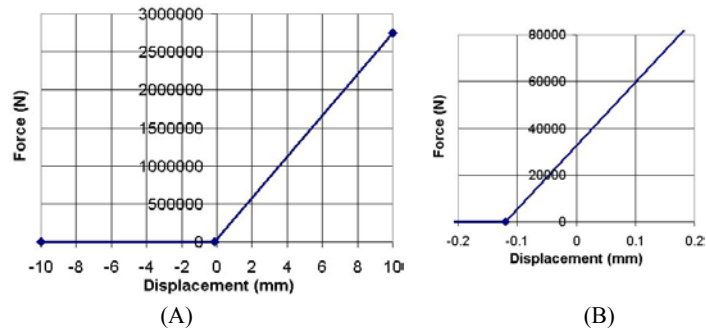


Figure 26. Bolt Spring Load Curve, NCAC Oregon 3x3 Slip Base Model

e) Impact Loading:

- i) Impacting cylinder is rigid and has a prescribed displacement in the negative X-dir.
- ii) *CONTACT_ENTITY is used to define the cylinder geometry and the contact between the rigid cylinder and the sign post. Refer to Figure 27.

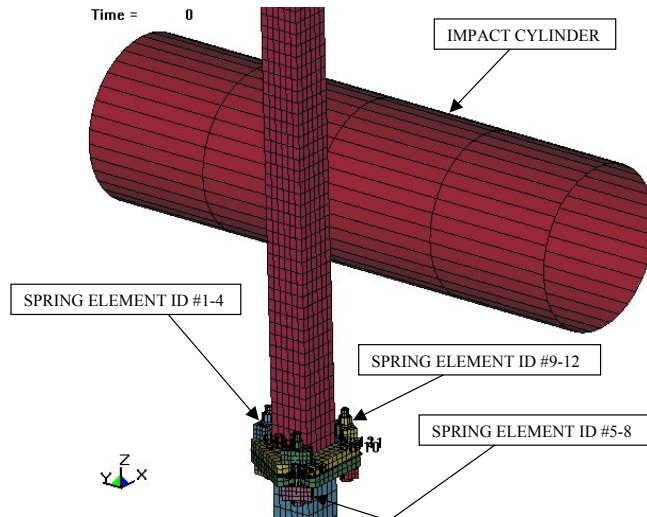


Figure 27. Spring Element Identification, Contact Entity

f) Element formulation:

- i) Slip base flanges (both upper and lower) use fully integrated solids.
- ii) Keeper plate specifies elform=7, S/R co-rotational Hughes-Liu
- iii) All other parts specify elform=0, default, constant stress solids.

g) Part ID's:

(1)	Impact cylinder	3017
(2)	stub	1
(3)	flange-lower	2
(4)	flange-upper	3
(5)	post plate	4
(6)	sign post	5
(7)	sign support bracket	6
(8)	sign blank	7
(9)	sign blank support bars-small	8
(10)	sign blank support bars-large	9
(11)	keeper plate	10
(12)	bolt shaft 1	11
(13)	bolt shaft 2	12
(14)	bolt shaft 3	13
(15)	plate washer 1-lower	14
(16)	plate washer 2-lower	15
(17)	plate washer 3-lower	16
(18)	plate washer 1-upper	17
(19)	plate washer 2-upper	18
(20)	plate washer 3-upper	19
(21)	hardened washer 1	20
(22)	hardened washer 2	21
(23)	hardened washer 3	22
(24)	springs	23
(25)	ground	24
(26)	spring-damper part definition	25
(27)	spring-damper part definition	26
(28)	spring-damper part definition	27

h) Contact definitions, slip base:

- i) Contact interfaces are defined separately and placed in groups using *SET_SEGMENT.
- ii) *CONTACT_SURFACE_TO_SURFACE and *CONTACT_NODES_TO_SURFACE are used.
- iii) Friction is defined in contact, fs = 0.18, fd = 0.14, dc = 0.

- Contact 1: Force transducer, part #2, lower flange
- Contact 2: Force transducer, part #3, upper flange
- Contact 3: Force transducer, part #5, sign post
- Contact 4: Force transducer, part #10, keeper plate

- Contact 5: Force transducer, part #17, top washer
- Contact 6: Force transducer, part #18, top washer
- Contact 7: Force transducer, part #19, top washer
- Contact 8: (surf2surf_1) Contact between lower flange and bolt head.
- Contact 9: (surf2surf_2) Contact between upper flange and nut.
- Contact 10: (surf2surf_3) ?????
- Contact 11: (surf2surf_4) Contact between keeper plate and ??? flange.
- Contact 12: (surf2surf_5) Contact between keeper plate and ??? flange.
- Contact 13: (surf2surf_6) Contact between bolt shaft and flange groove.
- Contact 14: (surf2surf_7) Contact between bolt shaft and flange groove.
- Contact 15: (surf2surf_8) Contact between bolt shaft and flange groove.
- Contact 16: (nodes2surf_9) Contact between bolt shaft and keeper plate.
- Contact 17: (nodes2surf_10) Contact between bolt shaft and keeper plate.
- Contact 18: (nodes2surf_11) Contact between bolt shaft and keeper plate.

i) Contact definitions. impact cylinder:

- i) *CONTACT_ENTITY is used to create a rigid cylinder impacting the sign post.

5.1.3 Discussion of Results:

- a) Upon slip base activation, the bolt shafts tear through the keeper plate as desired. However, there appears to be contact problems revealed by shooting nodes from a portion of the keeper plate that was torn away. These shooting nodes cause the simulation to terminate prematurely during one run. In a second run, the simulation terminated normally. This may indicate a somewhat unstable model. Refer to Figure 28.

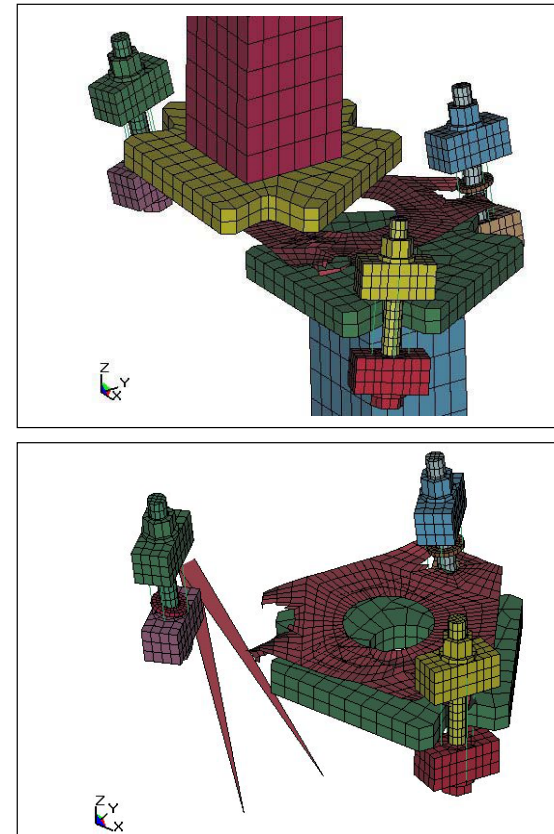


Figure 28. Keeper Plate failure, NCAC Oregon 3x3 Slip Base Model

b) The deforc data shows that each bolt is individually preloaded to 25 kN prior to simulation using dynamic relaxation. The total clamping load at the slip base joint is 75 kN for all three bolts combined. Following impact, the slip base has activated forcing the bolts out of the grooves in the flanges. This orientation allows the bolt tension to relax, reducing the spring deflection, and the spring (bolt) load goes to zero. Refer to Figure 29.

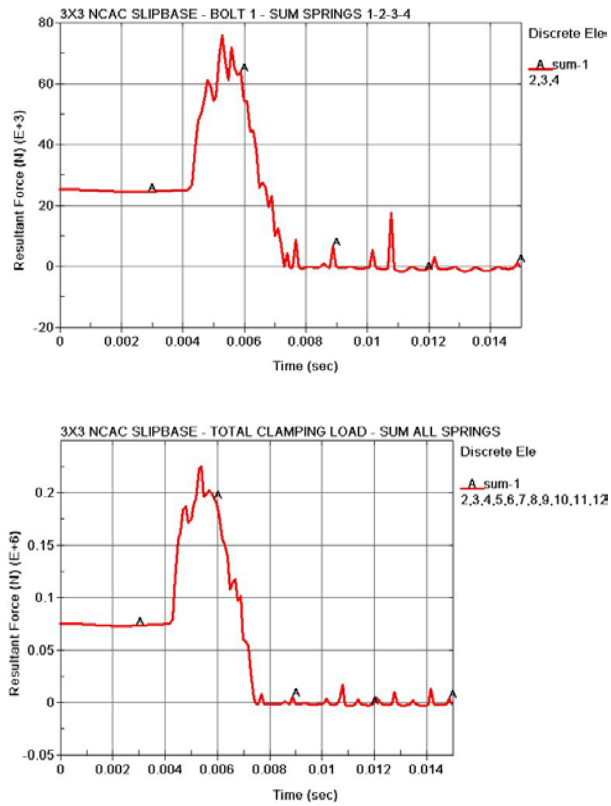


Figure 29. Deforc Data, NCAC Oregon 3x3 Slip Base Clamping Loads

c) The rforc data shows that the maximum contact force on upper and lower flanges during the slip base activation is 75 kN in the X-direction. There is a positive X-direction force resisting movement of the upper flange, and there is a negative X-direction force felt by the lower flange. The upper washers feel an initial contact force of 25 kN in the positive Z-direction, verifying the bolt preload revealed by the deforc data. Refer to Figure 30.

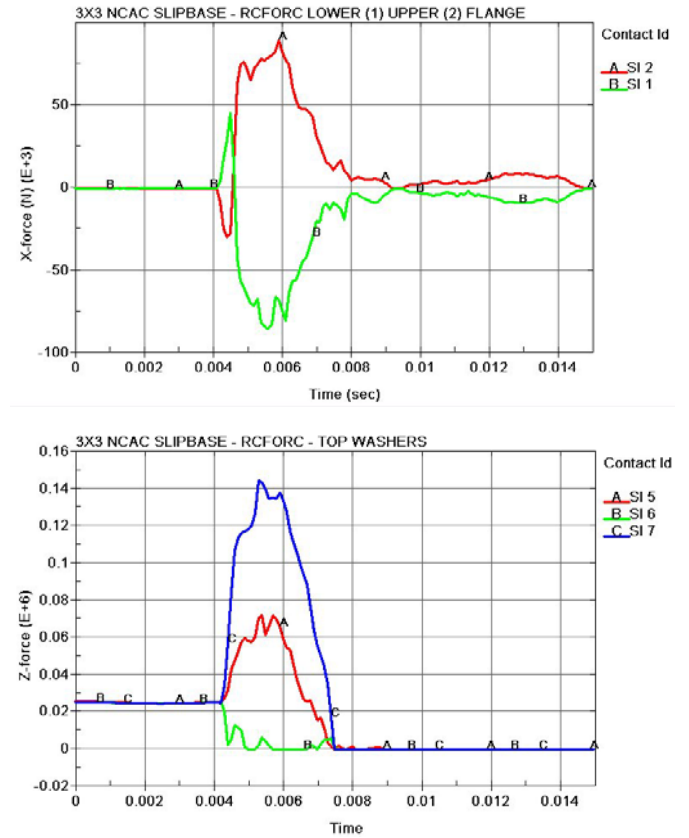


Figure 30. Rforc Data, NCAC Oregon 3x3 Slip Base Model

d) The 2 cross sections were placed in the horizontal plane through the lower flange and through the stub. The maximum X-direction cross sectional forces in both sections are oscillating between 50-100 kN, and appear to coincide pretty well. The initial Z-direction cross sectional force in the lower flange verifies the total slip base clamping load of 75 kN seen in the deforc and rforc data. Refer to Figure 31.

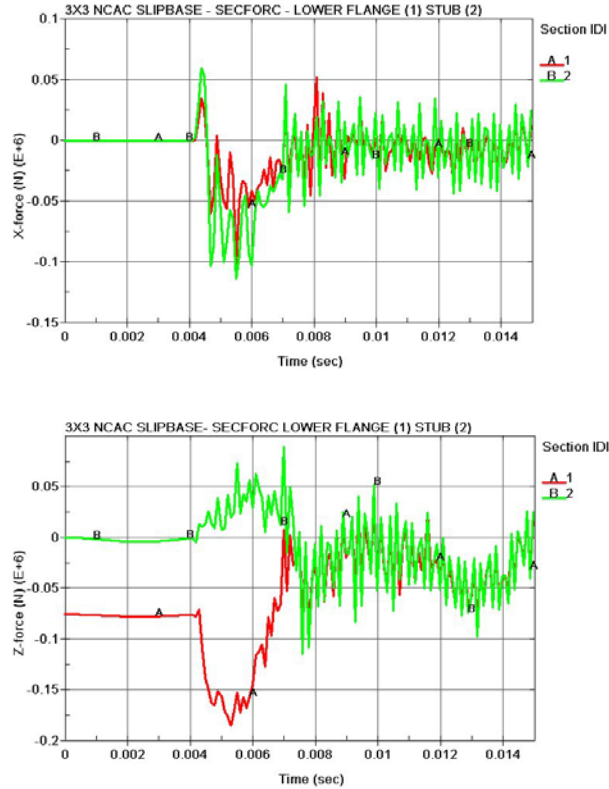


Figure 31. Secforc Data, NCAC Oregon 3x3 Slip Base Model

e) The glstat and matsum energy files indicate that the total hourglass energy is greater than 10% of the total internal energy of the system. However, most of the hourglass energy resides in the part “sign blank” which is not part of the slip base joint. The hourglass energy within the slip base components is negligible, and thus, of no concern. Most of the internal energy is generated from the deformation of the sign post upon impact. The cylinder has velocity of -12000 mm/s (27 mph). Refer to Figure 32 and 33.

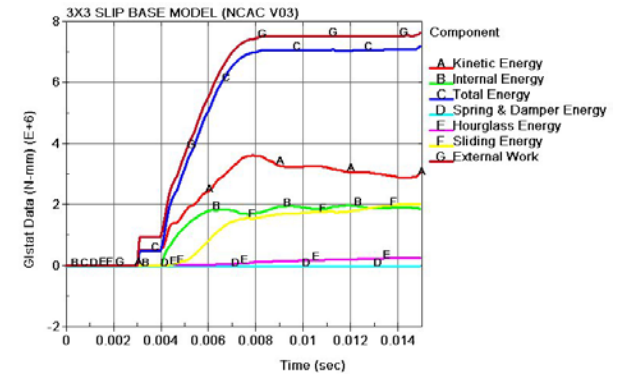


Figure 32: Glstat Data, NCAC Oregon 3x3 Slip Base Model

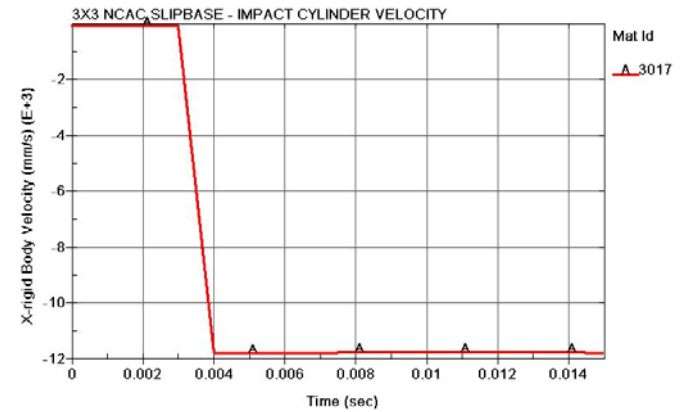


Figure 33. Matsum Data, NCAC Oregon 3x3 Slip Base Model

5.1.4 Model Evaluation:

- a) The bolts are preloaded effectively prior to simulation using dynamic relaxation. This allows the clamping load at the slip base joint to be in static equilibrium prior to any impact simulation, as it would be in reality prior to an actual impact.
- b) The combination of using 4 springs per bolt along with a translational joint between bolt and nut is redundant. The use of 4 springs per bolt was intended to create symmetric clamping load around the head of the bolt and nut. The translational joint alone will effectively force the bolt/nut to have symmetric clamping load because it does not allow out of plane twisting of either the bolt head or nut. Therefore, the use of 4 springs per bolt simply adds unneeded complexity to the model. For a more efficient and clean model, a single centralized spring between bolt and nut, along with a translational joint, could be used.
- c) Part “springs” are beam elements that are coincident with parts “spring-damper-definition” which are discrete spring elements. *MAT_NULL is specified for part “springs”, beam elements 7028-7039. It is likely that the beam elements are present only for visual representation of the springs in an early version of post processor.
- d) *MAT_PIECEWISE_LINEAR_PLASTICITY has undefined stress-strain curves (0.0). This is due to the fact that the tangent modulus ϵ_{tan} is defined, rather than defining a stress-strain curve. The defined value ($\epsilon_{tan} = 20000$) is questionable.

- e) All parts other than flanges specify $elform=0$, 1 point corotational for honeycomb. If the material is not corotational for honeycomb, zero indicates default element formulation, which is $elform=1$, constant stress solids.
- f) Both static and dynamic friction is separately defined in *CONTACT_(option), but decay factor (dc) = 0. The decay factor accounts for the exponential decay that exists between static and dynamic friction, and it is used to calculate the working friction coefficient during simulation. Because $dc=0$ in this model, the dynamic friction coefficient is not utilized, and the working friction is only based on the static friction coefficient.
- g) The need for a deformable bolt shaft is questionable.
- h) Separately defined contact surfaces create very complex contact assignment. It may be possible to use alternate contacts to simplify the model without adversely affecting behavior.
- i) The preliminary analysis of a rigid cylinder impacting the sign post reveals that the slip base model separates as desired. The forces required to activate the slip base and the bolt clamping load data both seem reasonable. While the keeper plate tears apart under loading, there appears to be contact troubles that create shooting nodes, and thus, the potential for an unstable model. Subsequent simulation runs revealed a less-than-robust model, terminating prematurely and terminating normally on separate occasions.

5.2 TTI Arizona D.O.T. Luminaire Slip Base

5.2.1 Model History:

- a) HM Model: none
- b) Original Dyna Model: **pole_only.key**, as downloaded from NCAC website. (36)
- c) Modified Dyna Model: **pole-only-3.k**
 - i) Modified by N. Hiser 12-Sept-02
 - ii) Reorganized and grouped cards, added section headings
 - iii) Modified control output cards to my liking.
 - iv) Add cross sections through middle washer and pole.
 - v) Add force transducers to flanges, pole, bolts, nuts.
 - vi) Add cylindrical contact entity with prescribed motion for impact.
 - vii) Start impact cylinder motion at 0.003 seconds to verify initialization.

5.2.2 Model Description:

- a) Units: tonne (1000 kg), mm, s, N, MPa, N-mm
- b) Geometry: 3-bolt, triangular slip base, without keeper plate. Refer to Figure 34.
- c) Material Definitions:
 - i) Washers are *MAT_PLASTIC_KINEMATIC.
 - ii) Bolts are *MAT_PLASTIC_KINEMATIC.
 - iii) Nuts are *MAT_PLASTIC_KINEMATIC
 - iv) Lower flange and upper flange are *MAT_RIGID.
 - v) Luminaire pole is *MAT_PIECEWISE_LINEAR_PLASTICITY.
- d) Bolt Clamping Load:
 - i) Modeled using 3 discrete spring elements per bolt, attached to the bolt head and nut. See Figure 35.
 - ii) Spring material definition is *MAT_SPRING_NONLINEAR_ELASTIC. Load curve is show in Figure 36A.
 - iii) Initial offset of spring elements is not defined. Rather, load curve is translated to the left so that load exists at zero offset. See Figure 36B.
 - iv) Translational joints are NOT defined between the bolt and nut. Therefore, orientation of the nut relative to the bolt shaft is constrained by small clearances between I.D. of nut, and O.D. of bolt shaft. Refer to Figure 35.
 - v) Dynamic relaxation is NOT specified within spring load curves to preload bolts.

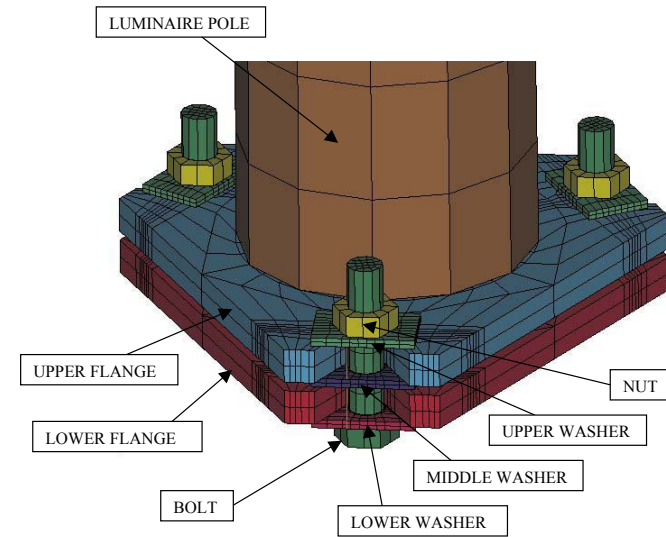


Figure 34. TTI Arizona D.O.T. Luminaire Slip Base Model Geometry

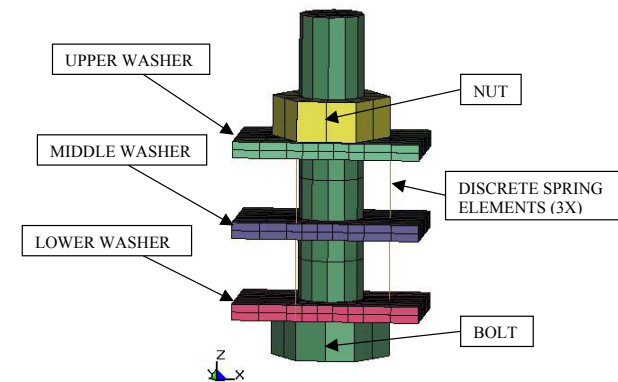


Figure 35. Bolted Joint Model, TTI Arizona D.O.T. Luminaire Slip Base

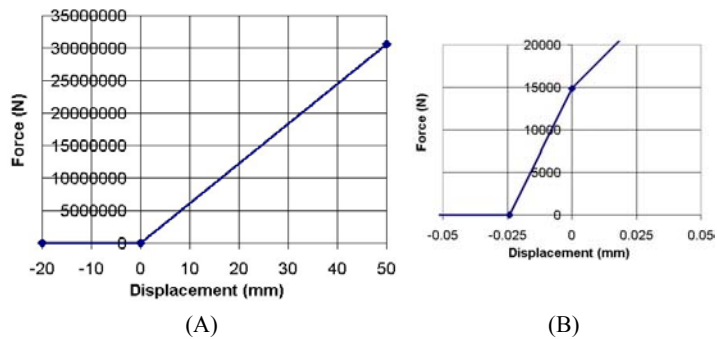


Figure 36. Bolt Spring Load Curve, TTI Arizona D.O.T. Luminaire Slip Base Model

e) Impact Loading:

- i) Impacting cylinder is rigid and has a prescribed displacement in the negative X-dir.
- ii) *CONTACT_ENTITY is used to define the cylinder geometry and the contact between the rigid cylinder and the luminaire pole. Refer to Figure 37.

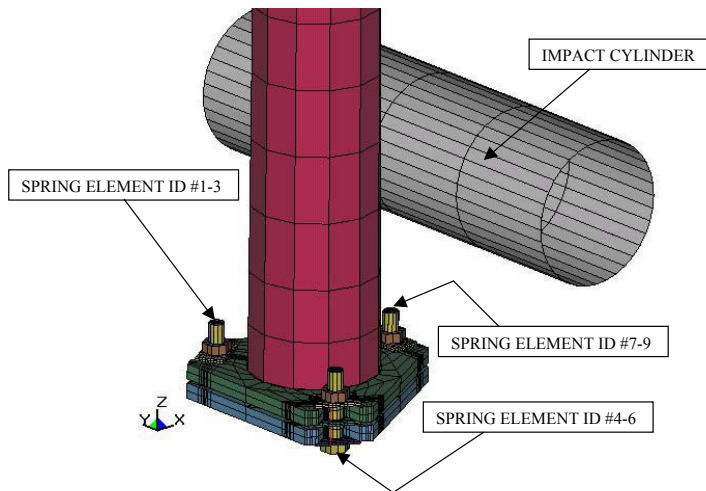


Figure 37: Spring Element Identification, Contact Entity

f) Element formulation:

- i) Bolts, nuts, washer specify elform=2, fully integrated solids.
- ii) Luminaire pole specifies elform=8, Belytschko-Leviathan shell

g) Part ID's:

(1)	Impact cylinder	3017
(2)	lower_flange	100
(3)	upper_flange	101
(4)	bolts	110
(5)	nuts	120
(6)	pole	300
(7)	washer_bottom	310
(8)	washer_middle	311
(9)	washer_top	312
(10)	mast	301
(11)	springs	313

NOTE: All 3 bolts defined as one part "bolts". All 3 nuts defined as one part "nuts". Similar grouping for washers.

h) Contact definitions, slip base:

- i) Contact interfaces are defined separately and placed in groups using *SET_SEGMENT.
- ii) *CONTACT_SURFACE_TO_SURFACE used exclusively.
- iii) Friction is defined in contact, fs = 0.20, fd = 0.15, dc = 0.

- Contact 1: Force transducer, part #100, lower flange
- Contact 2: Force transducer, part #101, upper flange
- Contact 3: Force transducer, part #110, bolts
- Contact 4: Force transducer, part #120, nuts
- Contact 5: Force transducer, part #300, pole
- Contact 6: (tied_shell_edge_to_surface) Contact between mast and pole.
- Contact 7: (surf2surf) Contact between bottom washer and lower flange.
- Contact 8: (surf2surf) Contact between middle washer and lower flange.
- Contact 9: (surf2surf) ?????? uses same segments as 8 and 10.
- Contact 10: (surf2surf) Contact between middle washer and upper flange.
- Contact 11: (surf2surf) Contact between top washer and lower flange.
- Contact 12: (surf2surf) Contact between top washer and nuts.
- Contact 13: (surf2surf) Contact between bottom washer and bolt head.
- Contact 14: ????
- Contact 15: ????
- Contact 16: ????

i) Contact definitions, impact cylinder:

- i) *CONTACT_ENTITY is used to create a rigid cylinder impacting the luminaire pole.

5.2.3 Discussion of Results:

- a) Upon impact, the luminaire pole deforms, the slip base activates, and the bolts are forced from the angled grooves in the plates as desired. Refer to Figure 38.

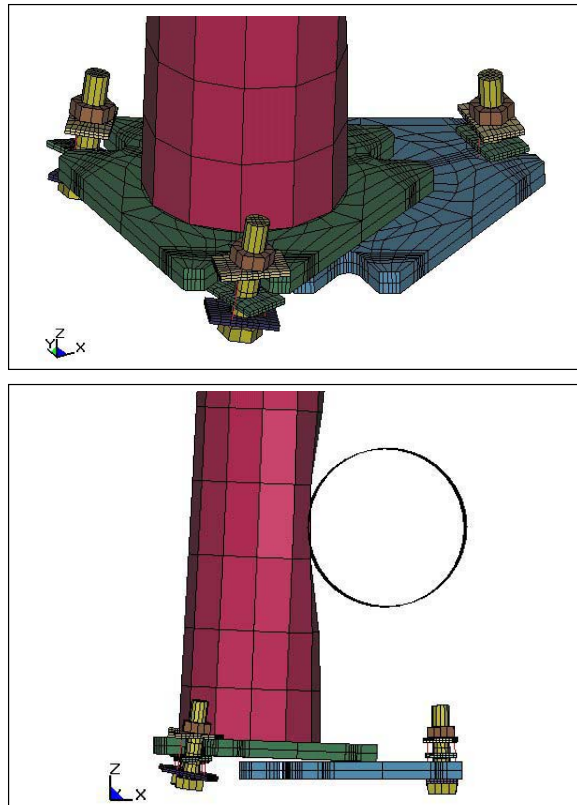


Figure 38. Slip Base Activation, TTI Arizona D.O.T. Luminaire Slip Base Model

- b) The simulation runs to completion and terminates normally. However, there are many initial penetration warnings given in the d3hsp file. In the clamped stack of components (bolt-washer-plate-washer-plate-washer-nut), the interfaces between components are created coincident with one another, rather than creating slight clearances at the interfaces. Upon initialization, some of these interfaces are identified as having initial penetrations, and the penetrating nodes are moved prior to simulation run creating initial deformed geometry. With the nut and bolt geometry deformed, the initial length of the discrete spring elements are altered, affecting the initial preload on the joint. Refer to Figure 39.

NOTE: SIMULATION TIME: $t=0$ → Time = 0

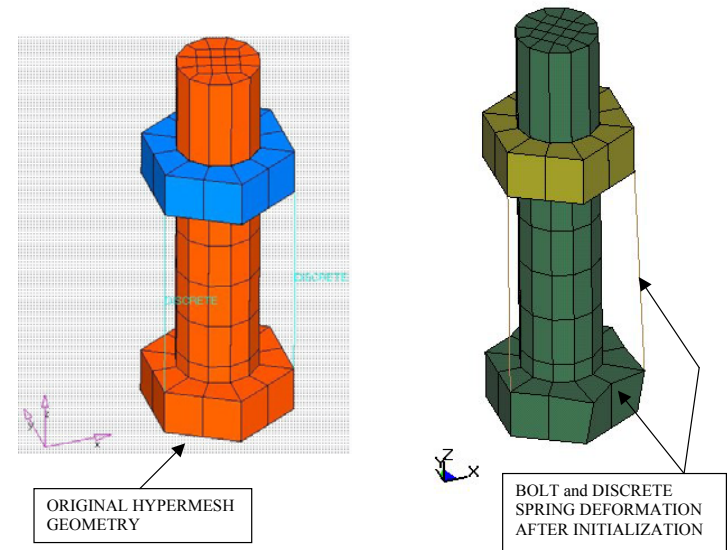


Figure 39. Bolt Deformation due to Initial Penetrations.

c) The deforc data shows that springs 1,3,4,6,7,9 initially have tension of 65 kN each, but the spring load falls to zero immediately, indicating that the joint is not resisting the spring load (i.e., the joint is allowing the spring deflection to decrease, releasing the load.) Following impact, the slip base has activated forcing the bolts out of the grooves in the flanges. The top plate rotates relative to the bottom plate (see Figure 38) causing springs #1-6 to stretch, increasing their load. Springs 2,5,8 each have an initial load of 15 kN. From the original Hypermesh geometry it is determined that 15kN was the intended initial spring load per spring (thus 45 kN per bolt, 135 kN total slip base clamping load), but due to bolt and nut deformations from initial penetrations, the initial spring load was increased in springs 1,3,4,6,7,9 due to increased deflections. Refer to Figure 40.

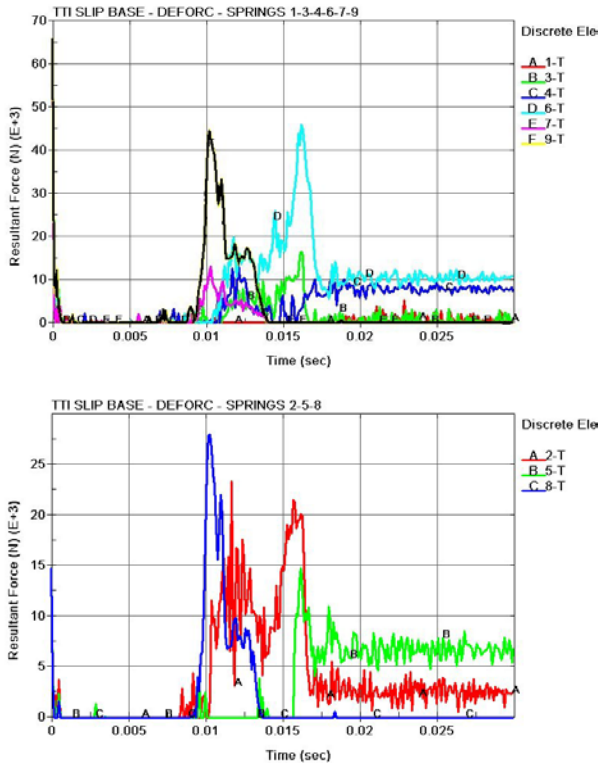


Figure 40. Deforc Data, Clamping Loads, TTI Arizona DOT Luminaire Slip Base Model

d) The rforc data shows that the maximum contact force on upper and lower flanges during the slip base activation is 100 kN in the X-direction. There is a positive X-direction force resisting movement of the upper flange, and there is a negative X-direction force felt by the lower flange. The luminaire pole data shows no contact force in the X-direction felt by the pole during the impact, reason unknown. Refer to Figure 41.

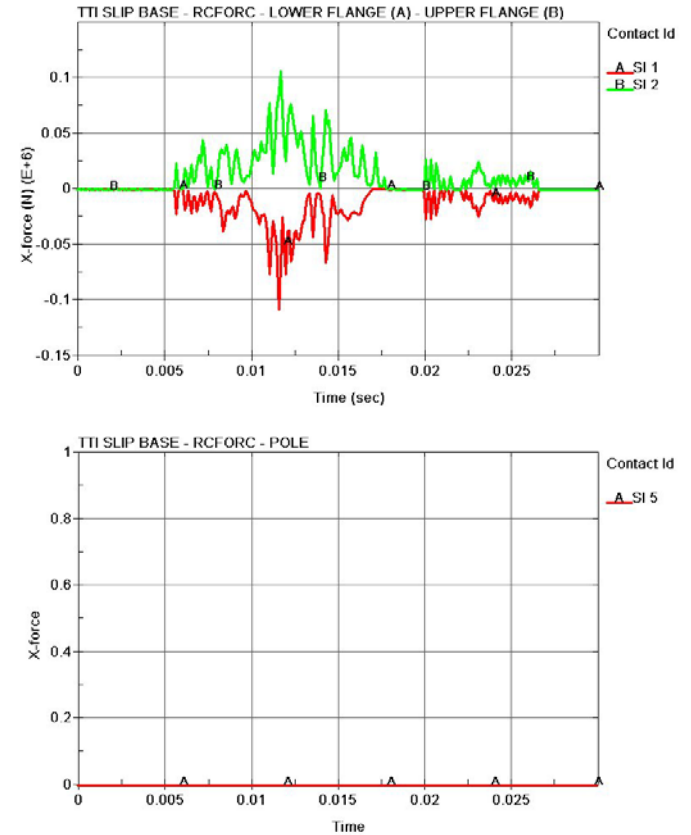


Figure 41: Rforc Data, TTI Arizona DOT Slip Base Model

e) The 2 cross sections were placed in the horizontal plane through the luminaire pole and the middle washer. Sections could not be placed through the upper and lower flanges because they were both rigid. The maximum X-direction cross sectional force in the luminaire pole is oscillating about 100 kN. The initial Z-direction cross sectional force in the middle washer is zero, indicating there is no initial bolt preload or gravity acting on the joint. Refer to Figure 42.

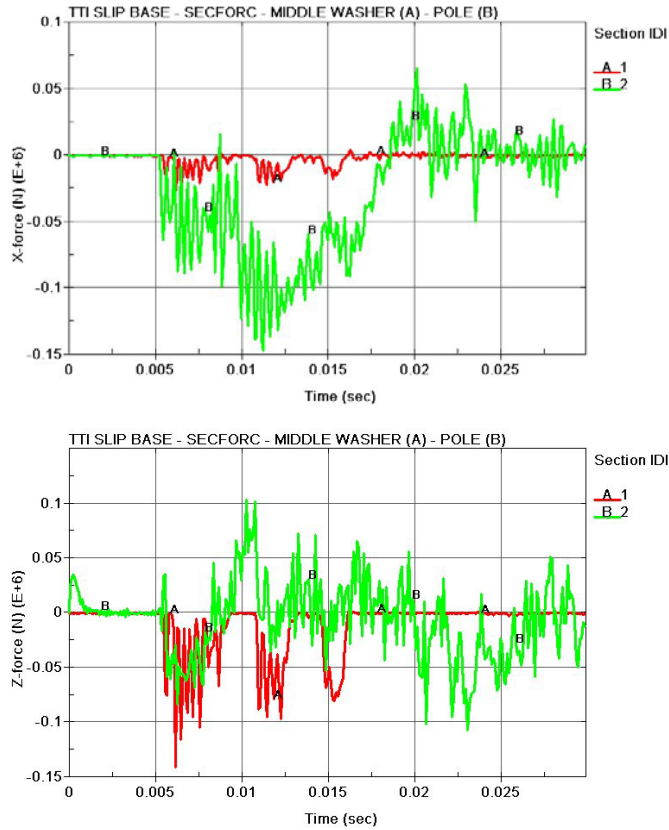


Figure 42: Secforc Data, TTI Arizona DOT Slip Base Model

f) The glstat and matsum energy files indicate that the total hourglass energy is negligible, and thus, of no concern. Most of the internal energy is generated from the deformation of the luminaire pole upon impact. The rbdout file indicates the cylinder has velocity of -11000 mm/s (24.6 mph). Refer to Figures 43 and 44.

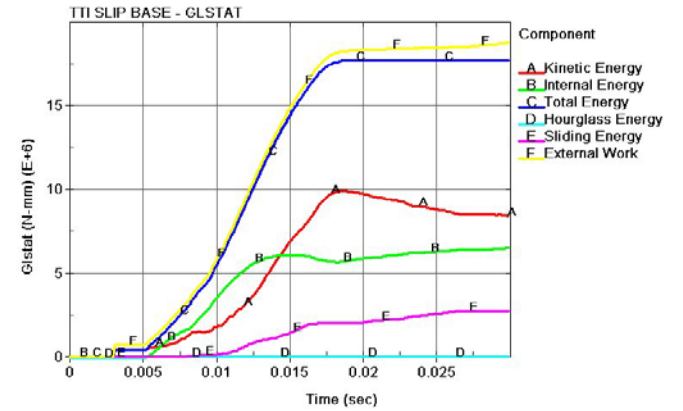


Figure 43. G1stat Data, TTI Arizona DOT Slip Base Model

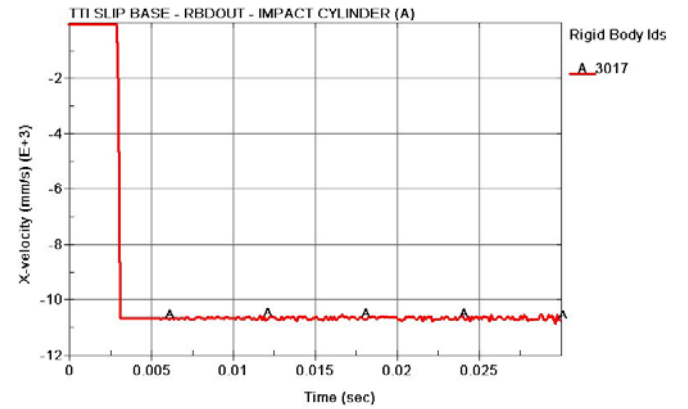


Figure 44. Matsum Data, TTI Arizona DOT Slip Base Model

5.2.4 Model Evaluation:

- a) The bolts are not preloaded effectively prior to or during simulation. Although the discrete springs used to create the bolt load are given a load curve offset to create a preloading effect at time zero, the bolt load falls to zero immediately during simulation, indicating a reduction in spring deflection. The cause of the loss of spring deflection is likely a result of the penetrations required for the penalty contact formulation to work properly. The use of dynamic relaxation and increased load curve offset in the negative X-direction would likely create acceptable bolt preload.
- b) The bolted joint is modeled without slight clearances between component surfaces, which creates initial penetrations and model deformation prior to simulation. The addition of very slight clearances between component surfaces would avoid initial penetrations.
- c) The use of 3 springs per bolt symmetrically about the bolt shaft was intended to create symmetric clamping load around the head of the bolt and nut. The nut and bolt are constrained relative to one another only by the contact between the bolt shaft O.D. and the nut I.D.. If there are extremely tight clearances between bolt and nut, this modeling approach may be sufficient. However, it is noted that in reality, the torqued nut is not allowed to twist out of plane relative to the bolt head due to the physical constraints imposed by the tight fit between the threads.
- d) This model uses deformable fastening components (bolts, washers, nuts) and rigid slip base flanges. It is questionable that this modeling approach is optimal for capturing the slip base behavior because flange deformation has been observed in

- prior slip base testing. An improved method that would be supported by previous testing would include rigid bolt and nut, and deformable washers and slip base flanges. This would then allow for placement of a single discrete spring along the axis of the bolt shaft attached to bolt and nut, and placement of a translational joint constraining the motion of the nut along the bolt shaft.
- e) *MAT_PIECEWISE_LINEAR_PLASTICITY has undefined stress-strain curves (0.0). This is due to the fact that the tangent modulus ϵ_{tan} is defined, rather than defining a stress-strain curve. The defined value ($\epsilon_{tan} = 20000$) is questionable.
 - f) The use of *MAT_SPRING_NONLINEAR_ELASTIC is questionable to model the tensile behavior of a bolt. In reality a bolt's tensile load curve contains an elastic portion and a plastic portion. If the bolt is loaded to within the plastic regime, energy will be absorbed to plastic deformation. The elastic behavior of the specified material will not recognize any energy lost to plastic deformation. A better choice of spring material would be *MAT_SPRING_GENERAL_NONLINEAR.
 - g) Both static and dynamic friction are separately defined in *CONTACT_(option), but decay factor ($dc = 0$). Because $dc = 0$, this model does not take into account the exponential decay that exists between static and dynamic friction, and therefore, the working friction is only based on the static friction coefficient.
 - h) Every component does not have an individual part number. Rather, multiple similar components are grouped. For example, the part "bolts" is made up of elements from all three bolts. The part "nuts" is made up of elements from all three nuts. The part "washer_mid" is made up of elements from all three middle

washers. Etc, etc. The result is that the output data from each part is actually a summation of data from the three separate components that make up that part. It is likely that this modeling practice will create confusion when trying to decipher output data, and sometimes even make output data irrelevant and unuseful for purposes of analysis.

- i) The need for a deformable bolt and nut is questionable.
- j) Gravity is not defined in this model. Because of the large mass of the luminaire pole, it is likely that the weight of the pole, in addition to bolt preload, would have a significant effect on the behavior of the slip base joint during impact. It is therefore concluded that gravity should be present in this model.
- k) Separately defined contact surfaces create very complex contact assignment. It may be possible to use alternate contacts to simplify the model without adversely affecting behavior.
- l) The preliminary analysis of a rigid cylinder impacting the luminaire pole reveals that the slip base model separates as desired. However, the forces required to activate the slip base and the bolt clamping load data are questionable. Bolt preload does not exist during onset of impact, indicating the slip base flanges are not clamped together as they would be in reality. Yet the flange rcfrc data indicates that there are significant loads felt by both flanges during activation. This is possibly due to binding of the slip base joint as the rigid flanges twist out of plane and slip past one another, loading the bolts and creating some resistance to the motion. However, the deforc data shows that there is force in some of the springs even after slip base activation, at which time there should be none.

Collectively, these factors indicate that the slip base model is not capturing reality.

5.3 Conclusions

Further analysis of the NCAC Oregon 3x3 slip base model and the TTI Arizona DOT luminaire slip base model would provide further insight of their respective slip base activation behavior. Isolation of the slip base joint and application of a range of boundary conditions from pseudo-static to fully dynamic would reveal more insight into the slip base modeling techniques, such as the validity of assigning rigid and deformable material properties to various slip base components, as well as activation forces and energy dissipation of the joints. It was concluded that both models displayed unacceptable overall behavior in simplified impacts with a rigid cylinder. The NCAC model proved unstable during keeper plate failure, while the TTI model failed in the area of providing adequate clamping forces between the flanges. Because of these shortcomings, improved slip base modeling techniques in LS-DYNA will be pursued in the remainder of this study.

6 FRICTION MODELING IN LS-DYNA

6.1 LS-DYNA Theory

Sliding friction in LS-DYNA is based on a Coulomb formulation, in which frictional forces are applied as the equivalent of an elastic-plastic spring to the slave nodes that make contact with and penetrate the master surfaces. The magnitude of the resulting frictional forces are a result of the assigned values of static and dynamic friction, f_s and f_d respectively, which are assigned in the contact cards, or alternatively, in the individual part cards (37).

Generally, LS-DYNA computes the frictional slip force and applies it to the slave nodes for every time step based on the relation:

$$F_s := \mu \cdot N \quad \text{Eqn. 6.1}$$

where F_s is the frictional slip force, μ is the instantaneous coefficient of friction, and N is the normal force. The instantaneous coefficient of friction is computed by the relation:

$$\mu := f_d + (f_s - f_d) e^{-dc \cdot |v|} \quad \text{Eqn. 6.2}$$

where f_s is the static friction coefficient, f_d is the dynamic friction coefficient, dc is the decay coefficient, and v is the relative velocity between the slave node and the master segment (1, 37-38). For a more detailed description of the frictional contact algorithm used in LS-DYNA, refer to the LS-DYNA theory manual (38). As illustrated in Figure 45, the instantaneous friction coefficient is plotted against relative velocity, v , to illustrate the effects of decay factor on the instantaneous friction coefficient.

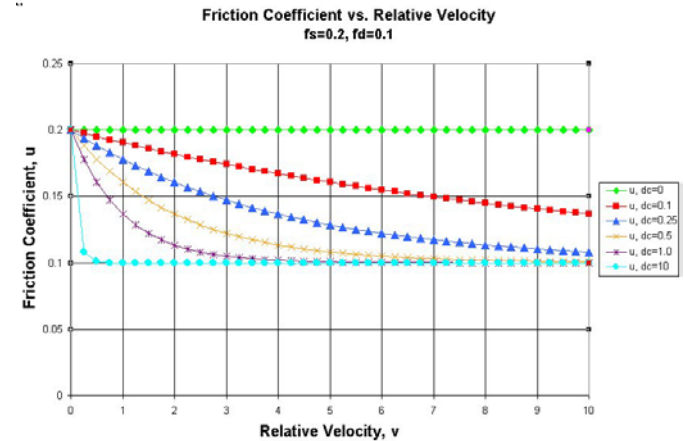


Figure 45. Friction Coefficient vs. Relative Velocity, Calculated by Eqn. 6.2

For computation of the instantaneous friction coefficient in LS-DYNA to work as intended, the static coefficient of friction (f_s) must be larger than the dynamic coefficient (f_d), and the decay coefficient (dc) must be non-zero. For this illustration the static friction coefficient was specified as 0.2, and the dynamic friction coefficient was specified as 0.1, and the decay factor is set at 1.0. As is evident in Figure 45, the decay coefficient determines the rate at which the instantaneous friction coefficient transitions from f_s to f_d with increasing slip velocity. If a decay coefficient of zero is specified, the instantaneous coefficient of friction (μ) is equal to the static friction coefficient (f_s) for all slip velocities. On the contrary, if a very large decay coefficient is specified, the result is an instantaneous, or step, transition between f_s and f_d , which could potentially result in an undesired and unrealistic dynamic system response. From the data shown in Figure 45, it is apparent that the instantaneous friction coefficient, and thus the slip force

computed by LS-DYNA, is highly dependent on the user specified decay factor, as well as the relative velocity between the contacting surfaces.

It must be recognized that the physical phenomenon of friction which includes the molecular interaction of two surfaces is in no way equivalent to the mathematical computation of friction in LS-DYNA which uses the penalty method at the contact interface of two meshed surfaces. Because of this, it is expected that the computed frictional forces in LS-DYNA may not match the physical frictional forces if the physically obtained coefficients of friction are directly specified. For practical use in LS-DYNA, it is recommended to initially set frictional coefficients based on published physical values as a starting point, with a non-zero decay factor, and then adjusting the values accordingly to obtain a useful and accurate simulation. Experience in LS-DYNA suggests using a friction coefficient of about 0.10 - 0.15 for steel-to-steel contact for most impact simulations. It is also noted that the static and dynamic friction coefficients are frequently assigned equal values in crash simulations to avoid the creation of additional noise in the data (37).

6.2 LS-DYNA Friction Simulations

A simplified LS-DYNA model, as displayed in Figure 46, was created to further investigate and verify the behavior of sliding friction in LS-DYNA. The main objective was to verify that the magnitude of the slip force follows the relation in equation 6.1, as well as to verify the effect of the friction coefficients and decay factor as they relate to the computed slip force with increasing slip velocity, per the relation in equation 6.2.

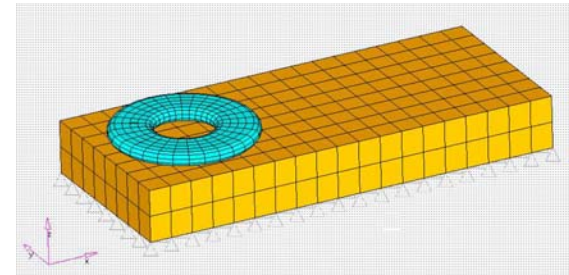


Figure 46. LS-DYNA Friction Investigation Model

The LS-DYNA model consisted of a rigid washer, as used in subsequent slip base simulations, loaded against a plate of deformable solid elements with a rigid body loading of 10 kN. The plate was constrained in all six degrees-of-freedom using single point constraints on all nodes on the bottom face of the plate, and the washer was given a prescribed velocity motion along the top face of the plate. The frictional coefficients were assigned in the automatic single surface contact.

In order to gather some meaningful data to illustrate the frictional behavior computed by LS-DYNA, three parameters were isolated and studied in detail. Based on the frictional algorithm previously described and detailed in the LS-DYNA Theoretical Manual (38), the three parameters determined to likely have significant effect on the frictional slip behavior, and thus chosen for this investigation, were element size, element formulation, and slip velocity.

The effects of element size was investigated first. During the model development process, snagging between the washer and the plate produced unacceptably high slip forces and component stresses. Simply by refining the washer mesh size and radiusing the washer edges, the snagging problem was eliminated. The washer geometry and mesh

size, as shown in Figure 46, was thus used in all subsequent simulations. The plate mesh size was also investigated. It was determined that an increasingly fine plate mesh resulted in a decrease in the noise present in the slip force data from the cross-sectional secforc data file, and conversely, a courser plate mesh increased the noise in the secforc data. However, it was apparent that both the fine and course plate mesh had equal ability to capture the slip forces in the reforc data file. Thus, it was determined that the slip forces as captured by the reforc data is relatively unaffected by the plate mesh size. Therefore, the courser mesh was chosen for use due to its ability to accurately capture slip forces with decreased computational time. The final washer and plate mesh sizes used in subsequent simulations are illustrated in Figure 46.

The effects of element formulation was investigated next. The reforc simulation results indicated that both constant stress and fully integrated solids similarly capture frictional slip forces. Correlation of the reforc data revealed it is relatively unaffected by element formulation. Although the constant stress solid elements created less noise in the cross-sectional secforc data, hourglass energy was unacceptably high, limiting the usefulness of the constant stress solid elements. Therefore, it was determined that fully integrated solid elements would be required to accurately capture friction and slip forces, and thus, fully integrated solid elements were used for the slip base flanges in all subsequent simulations.

Finally, the effects of slip velocity were investigated. Initially the static and dynamic friction coefficients were specified as $f_s=f_d=0.2$. They were initially set equal to eliminate the effects of the decay coefficient in order to verify the relation between slip force, normal force, and coefficient of friction: $F_s=\mu*N$. With a normal force of 10 kN

and a friction coefficient of 0.2, the resulting slip load should be 2.0 kN. The washer velocity was varied from 0.1 mm/ms, to 1.0 mm/ms, and finally to 10.0 mm/ms. The results are displayed in Figure 47. The simulation data generally revealed a slip force of 2.0 kN as expected. Note that the slip force at the lowest velocity of 0.1 mm/ms is about 1.8 kN, which is about 10% below the expected value, and with increased velocity the slip force is exactly 2.0 kN. Although the cause of the reduced slip force at the lowest velocity was not immediately apparent, the slip velocity was unrealistically slow (0.1 mm/ms = 0.22 mph) relative to actual crash simulations. Because the slip force behaves as expected at the higher velocities that are relevant to automobile crash simulations, it was determined that the unexplained slip behavior at the slowest speed is not worthy of further investigation at this time.

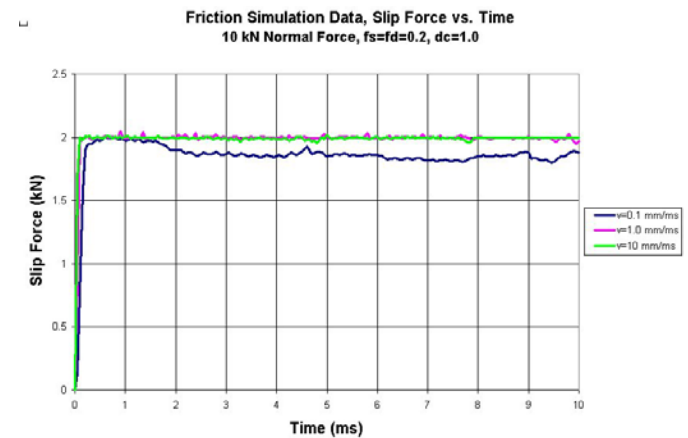


Figure 47. Slip Force vs. Time, Friction Constant $f_s=f_d=0.2$, Velocity Varies

Once the $F_s = \mu * N$ relation was verified, the factors that affect the instantaneous coefficient of friction (μ) in LS-DYNA were introduced into the simulations. The static friction coefficient, the dynamic friction coefficient, and the decay factor were specified as 0.2, 0.1, and 1.0 respectively. Six separate simulations were run with various prescribed velocities assigned to the washer. The washer velocity varied between 0.001 mm/ms up to a maximum velocity of 10.0 mm/ms. In all simulation runs the normal force between the washer and plate was 10 kN. The simulation results are shown in Figure 48. It is apparent from Figure 48 that the instantaneous coefficient of friction, and thus the slip force, is directly related to the slip velocity by the relation in equation 6.2. As the velocity increases, the instantaneous coefficient of friction decreases by the relation in 6.2, and thus, the slip force, F_s , decreases in direct proportion. Note at the lowest velocity of 0.001 mm/ms, the slip force is nearly at 2.0 kN, which indicates an instantaneous friction coefficient of about 0.2, while at the highest velocity of 10.0 mm/ms the slip force is exactly 1.0 kN, indicating an instantaneous friction coefficient of about 0.1. The slip behavior over the range of slip velocities verifies that the simplified model is capable of capturing accurate and predictable slip behavior.

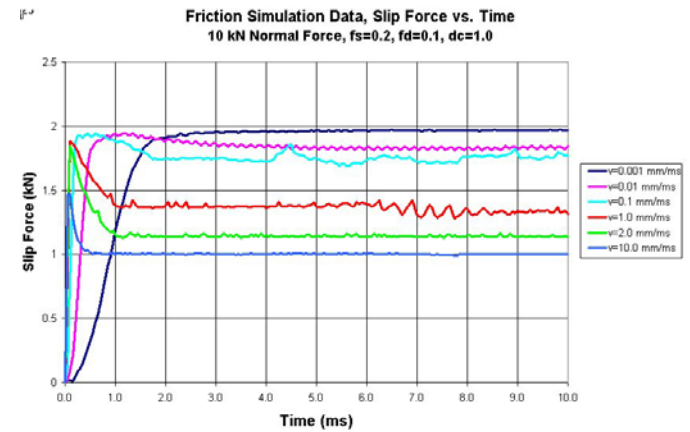


Figure 48. Slip Force vs. Time, Friction Varies $f_s=0.2$, $f_d=0.1$, Velocity Varies

6.3 Conclusions

The finite element model shown in Figure 46 was used to investigate slip behavior in LS-DYNA. Through a model development process, the element size and element formulation of both washer and plate were investigated and modified to accurately capture the slip phenomenon, and a parameter study was conducted on slip velocity and friction coefficients in order to verify the final model's slip behavior. It was thus concluded that the model shown in Figure 46 is capable of accurately and consistently capturing the slip behavior as described by equations 6.1 and 6.2. The model geometry, element formulation, and friction coefficients verified herein will be used in subsequent, and more complex, slip base simulation models.

7 SLIP BASE CLAMPING TECHNIQUES

In Chapter 5, two previously developed slip bases, and their clamping techniques, were described in detail. In both cases discrete spring elements were placed between the bolt head and nut to simulate the clamping load. However, aside from the similar usage of discrete spring elements, few of the remaining slip base modeling details were similar. In the end, both models were shown to have limitations and shortcomings that greatly affected the ability of the model to accurately capture the slip base impact event.

Because of the observed inadequacies of the existing models, the next phase of this study involved developing and refining multiple clamping methods in LS-DYNA for application to the simulated impact of slip base structures. It has been shown that the clamping load, and thus resulting slip force, is one of the primary factors affecting the behavior of a slip base mechanism. It is therefore crucial to this study to create methods that enable the user to accurately and consistently specify clamping loads between the slip base plates. Prior to testing the various slip base clamping techniques on a fully detailed slip base model under impact conditions, these techniques were first validated only for obtaining desired preload. It is desirable for these clamping methods to be thoroughly understood, consistently behave in a stable manner, and be user friendly for use in other applications. Three clamping techniques/models of varying complexity were developed within this study.

7.1 Jnt-1 Bolted Joint Model

The first, and most simplified, clamping technique was developed during prior research conducted by Paulsen, and was reproduced in a similar fashion for this study (39). The model consisted of two slip base flanges modeled with shell elements, between

which bolt tension was simulated using a nonlinear discrete spring placed in the location of the bolts. As in the previous work, the springs were given a non-linear load curve that corresponded with the desired bolt preload due to torque. Steel-on-steel friction was defined between the steel plates. Upon simulation initialization, the springs create a normal clamping force of 5.33 kN between the steel plates. Refer to Figure 49 and Figure 50 which displays the model and preload.

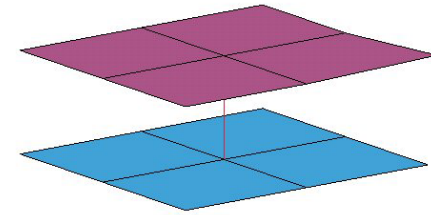


Figure 49. Jnt-1 Bolted Joint Model

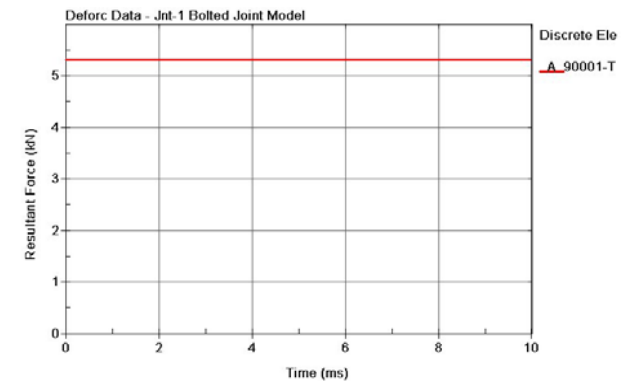


Figure 50. Deforc Clamping Data, Jnt-1 Bolted Joint Model

While this first clamping technique works well for forcing two plates together with a prescribed initial load, it does not in any way simulate the mechanical interactions

between the bolt and the clamped members which take place in an actual bolted connection. Therefore, it is concluded that a more complex clamping technique/model should be investigated for use in slip base mechanisms.

7.2 Jnt-2 Bolted Joint Model

A second, and more detailed, clamping technique was developed based on previously conducted modeling research performed by NCAC and TTI (36). The modeling approaches taken in the NCAC and TTI slip base models were previously analyzed and evaluated in Chapter 5, and various changes and improvements were made in order to simplify the model while improving upon the clamping behavior. The second clamping technique was investigated using model Jnt-2, of which the geometry is shown in Figure 51.

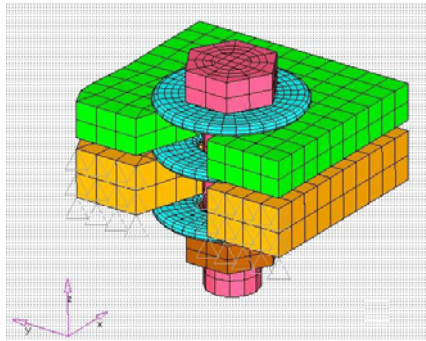


Figure 51. LS-DYNA Model Jnt-2, Clamping Technique #2

The Jnt-2 model consisted of two plates, with the V-notch geometry and thickness of the actual slip base plates, clamped together with a single bolt model. Like the NCAC and TTI bolt models, the Jnt-2 bolt model utilized discrete spring elements to preload the bolt and generate the clamping force between the slip base plates. The slip base plates

were modeled with deformable fully integrated solid elements. The bolts, nuts, and washers were modeled after the actual component geometry with rigid solid elements. Based on physical test results of cable guardrail systems in end on impacts, it has been shown that the slip base plates plastically deform, and the bolts, nuts, and washers do not plastically deform. Refer to Figure 52. Also, previous laboratory testing has revealed improved slip behavior with the use of hardened steel washers (22). Therefore, the use of deformable material properties for the slip base plates, and rigid material properties for the fastener components as a simplifying assumption was initially justified.



Figure 52. Bolt, Nut, and Washers Following Slip Base Activation (CT-2)

During the friction investigation discussed in Chapter 6 and the Jnt-2 model development process, it was determined that the washer mesh size with radiused edge geometry as indicated in Figure 51 was required to prevent snagging on the slip base plates during the slip process. The refined washer mesh needed for contact purposes, was thus, most practical for use when rigid material properties were assigned to the washer.

The use of deformable fully integrated solid elements would result in a significantly reduced time step, and increased computational cost.

In an attempt to eliminate some of the complexity and redundancy of the NCAC and TTI models, as well as to more accurately model the physical behavior of a bolted connection, a number of significant modeling changes were implemented. First, a single centrally located discrete spring element was used for joint preloading purposes. The spring was defined to act along the axis of the rigid bolt shaft, connecting the head of the bolt to the center of the nut. Secondly, a translational joint was placed between the nut and bolt shaft in order to constrain the nut to movement only along the bolt shaft. Adding this constraint is justified by two things: (1) in reality the torqued nut is not allowed to twist out of plane relative to the bolt head due to the physical constraints imposed by the tight “wedging” fit between the threads of a torqued nut and bolt; and (2) the translational constraint eliminates contact between nut and bolt for reduced computational time. This bolt modeling technique was similar to the method previously used by Belter (19). The global contact algorithm assigned was *CONTACT_AUTOMATIC_SINGLE_SURFACE, replacing the multiple contact definitions in the NCAC and TTI slip base models. Dynamic relaxation was also applied to the discrete spring load curve to eliminate the dynamic response of the joint as it was initially preloaded and clamped together. By using dynamic relaxation, the dynamic reaction between the bolts and flange plates took place during simulation initialization, and therefore, the joint attained a state of static equilibrium prior to any further simulation.

The single discrete spring element was assigned elastic properties, and thus, the load in the spring follows the linear relation:

$$F=K*X \quad \text{Eqn. 7.1}$$

The bolt shaft stiffness, K, is a function of the tensile stress area, A, the elastic modulus of the shaft material, E, and the length of the loaded shaft, L, per the relation:

$$K=(A*E)/L \quad \text{Eqn. 7.2}$$

For the ½-13 UNC bolt used in the cable system slip base, the bolt shaft stiffness is 455.7 kN/mm. Refer to Figure 53 for the force-deflection characteristics of the discrete spring element used in the Jnt-2 model for simulated bolt clamping. In order to produce a desired preload, the spring was given an initial offset or deflection, X, which induced an initial force within the spring. However, other factors besides initial spring offset contributes to the final spring load. The slip base plates in the Jnt-2 model are separated by very slight clearances to avoid initial penetrations, and the slip base plates are deformable and compress slightly when clamped under load. These two factors together generate some very small displacements in the discrete spring element at onset of simulation. Because the bolt stiffness is very large, these minute displacements cause a significant reduction in clamping load. Thus, a few iterations are required in order to generate the desired preload within the bolted joint.

For example, to attain a final bolt preload of about 11 kN, an initial offset of 0.1162 mm was required. From Figure 53 it is apparent that an offset of 0.1162 mm will produce a spring load of about 50 kN. However, after the clearances between the plates are eliminated, and the plates deform under the load, a final state of static equilibrium is attained at a preload of about 11 kN. Refer to Figure 54 which illustrates the defore data from LS-DYNA indicating the load within the discrete spring element in the Jnt-2 model.

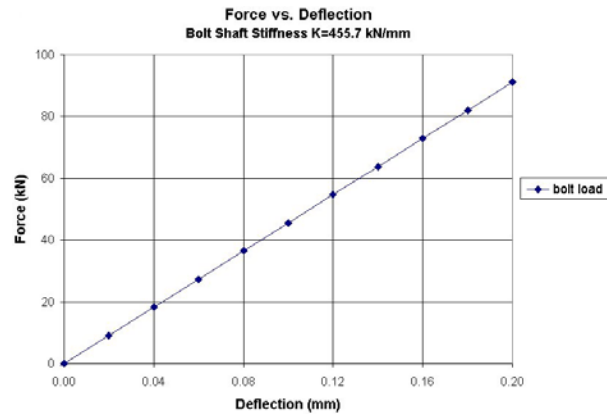


Figure 53. Force vs. Deflection, Discrete Spring Element Used in Jnt-2 Model

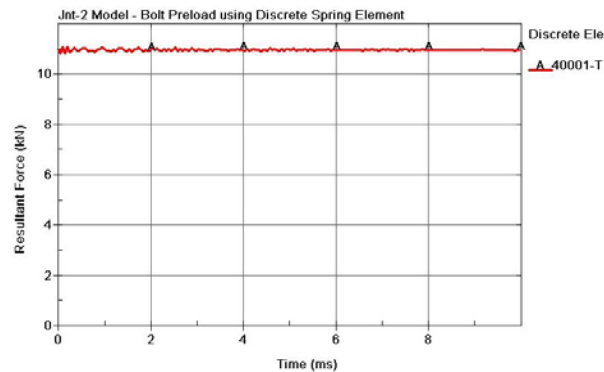


Figure 54. LS-DYNA Deforc Data, Preload Verification of Model Jnt-2

Based on the Jnt-2 preload simulation results, it is concluded that this clamping technique has demonstrated its ability to accurately and consistently produce the desired preload for the clamping of a slip base mechanism. It does require a few iterations in

order to attain a final desired preload within the joint. The Jnt-2 model is an improvement over the NCAC and TTI slip base models, as it incorporates many of the previously developed modeling techniques, but it eliminates those aspects that hinder its performance, or are excessively complex or redundant. The assumptions and simplifications made in the Jnt-2 model were based on actual slip base impact tests in which the slip base was forced to activate in the slip direction. In a longitudinal impact these assumption may often be valid, resulting in acceptable behavior of the Jnt-2 model. However, it is conceivable that uncommon impact conditions may result in excessive loading of the bolts, causing them to fail. The bolt shaft in the Jnt-2 model is rigid and will not fail under any circumstances.

7.3 Jnt-3 Bolted Joint Model

A third and final slip base clamping technique was developed for this study. The objective of this portion of the study was to develop a bolt model that would capture a higher sense of realism regarding the bolt preload method and the physical behavior of the bolt shaft itself. This clamping technique would require a bolt model that utilized deformable solid elements with the material properties of steel, which when stretched through an initial deflection, would produce the desired preload in a manner consistent with an actual bolt. The justification in developing such a model is that an improved bolt model would be able to capture more realistic slip base behavior in both common and uncommon impact events.

When an actual bolt is torqued, a tensile stress is developed within the bolt shaft as it stretches or deflects axially. The stress in the shaft is defined as:

$$\sigma = F/A \quad \text{Eqn. 7.3}$$

where F is the bolt tension, and A is the tensile stress area (40). The strain in the shaft is defined as:

$$\epsilon = \delta / L \quad \text{Eqn. 7.4}$$

where δ is the deflection, and L is the original shaft length (40). The elastic modulus, E , is a physically measured property of the material that relates stress and strain using Hooke's Law as in the following relation (40):

$$E = \sigma / \epsilon \quad \text{Eqn. 7.5}$$

Further simplification of Hooke's Law leads to a relation that yields bolt elongation from a given tensile stress level of a particular bolt geometry:

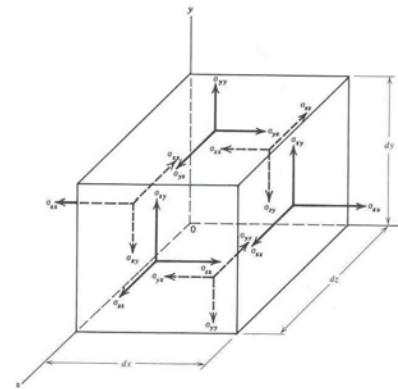
$$\delta = (\sigma * L) / E \quad \text{Eqn. 7.6}$$

With the knowledge of the previous relations, it is apparent that it is physically possible to generate a tensile load, and the corresponding tensile stress, within a material simply by stretching it through a given deflection. It may thus be possible in the realm of finite element analysis to "prestretch" a modeled bolt shaft to induce the desired preload for clamping together the slip base plates. Although prestretching the FE bolt shaft from an initial relaxed length was not accomplished in this study, an alternate, and equally effective method of prestressing the bolt shaft was developed.

7.3.1 Stress-1 Solid Element Prestress Model

LS-DYNA has a keyword card called *INITIAL_STRESS_SOLID that allows the user to assign initial stress within solid elements (1). The use of this keyword requires the user to assign values for the six principal stress components at each integration point within the solid element. These six principle stress components are

derived in classical mechanics texts by summing forces and moments on the faces of a cubic volume element, as shown in Figure 55 (41).



9 component stress tensor:

$$\mathbf{T} = \begin{bmatrix} \sigma_{xx} & \sigma_{xy} & \sigma_{xz} \\ \sigma_{yx} & \sigma_{yy} & \sigma_{yz} \\ \sigma_{zx} & \sigma_{zy} & \sigma_{zz} \end{bmatrix}$$

Summation of moments produces:

$$\sigma_{yz} = \sigma_{zy}, \quad \sigma_{zx} = \sigma_{xz}, \quad \sigma_{xy} = \sigma_{yx}$$

6 component stress tensor:

$$\mathbf{T} = \begin{bmatrix} \sigma_{xx} & \sigma_{xy} & \sigma_{xz} \\ \sigma_{xy} & \sigma_{yy} & \sigma_{yz} \\ \sigma_{xz} & \sigma_{yz} & \sigma_{zz} \end{bmatrix}$$

Figure 55. Six Principal Stress Components on a Volume Element (41)

If the stress states at all points within a body are known, those stresses can be defined at all of the integration points within the corresponding FE model. Therefore, the goal was to assign an initial stress state to all of the solid elements that make up the bolt shaft, so that the prestressed shaft will generate a clamping load between the slip base flanges by the relation $\sigma = F/A$.

A very simple four-element model, dubbed Stress-1, was developed to investigate the solid element prestressing keyword in LS-DYNA. As shown in Figure 56, four cubic elements were stacked in the z direction, with edge lengths of 1mm. The top and bottom elements are constrained in all six degrees of freedom with single point nodal constraints. The elements are fully integrated elements with 8 integration points each. Stress components were defined at every integration point using the

*INITIAL_STRESS_SOLID keyword. The zz stress component was defined as 0.200 Gpa (29,000 psi), while the remaining five stress components are all assigned zero stress. A cross-section was placed through the middle of the elements to monitor the induced tensile force.

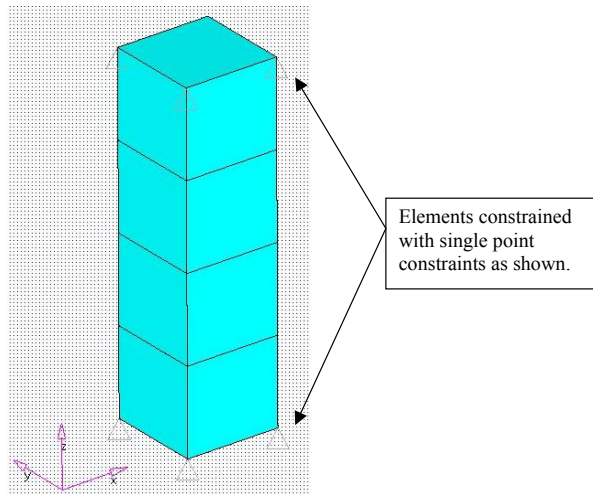


Figure 56. Stress-1, Element Prestress Investigation Model

The stress fringe plots displayed in Figure 57 make it clear that the stress induced in the element stack is a tensile stress in the z-direction only, as both the x and y plots show zero stress present in the elements. As the secforc data shows in Figure 58, the prestressing of the elements created an induced tensile load of 0.2 kN. Checking the DYNA results against the relation $\sigma=F/A$ reveals that the LS-DYNA model exactly matches the anticipated tensile load of 0.2 kN.

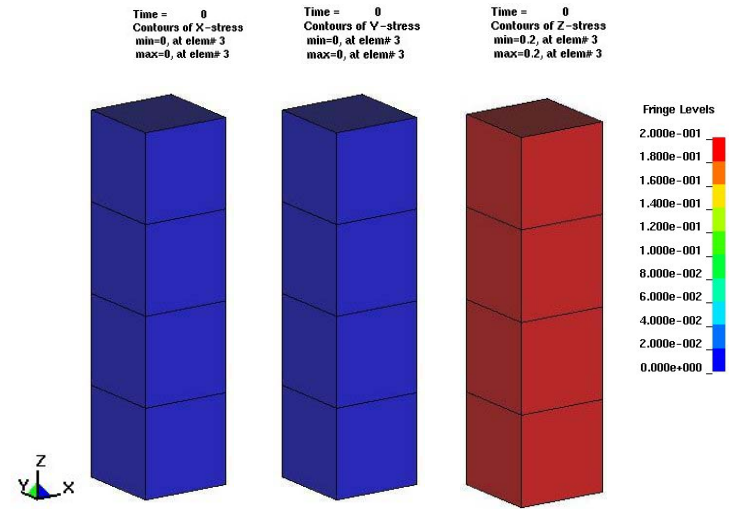


Figure 57. Element Stress Fringe Plots

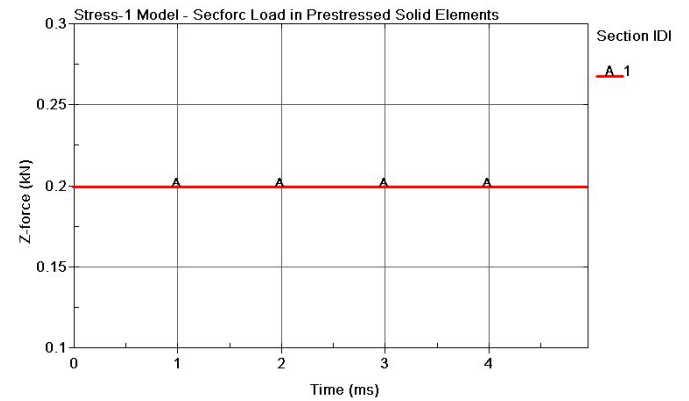


Figure 58. LS-DYNA Secforc Data, Tensile Load due to Prestress in Solid Elements

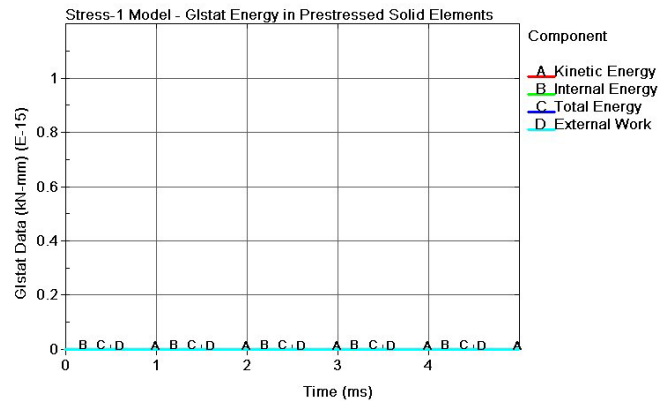


Figure 59. LS-DYNA Gstat Data, Energy due to Prestress in Solid Elements

It is important to note the data from the glstat file, as seen in Figure 59, which indicates that there is no energy of any kind present in the prestressed element model. This is due to the fact that there is absolutely no motion or element deformation taking place as the simulation progresses. By prestressing the elements, the elements are essentially deformed prior to simulation, so LS-DYNA does not recognize any internal energy. In other words, the initial prestressed state of the elements is a state of zero energy. In reality, there would be some internal energy within the bolts due to the elastic deformation during preloading, and would be equal to:

$$I.E. = (1/2) * K * X^2 \quad \text{Eqn. 7.7}$$

where K is the bolt shaft stiffness, and X is the deflection of the bolt shaft. Because the bolt deflection is so small, it was concluded that the amount of internal energy in a preloaded bolt can be neglected when considered relative to the amount of energy present during an actual impact event. From the results of this simplified prestress simulation

Stress-1, it was concluded that the *INITIAL_STRESS_SOLID keyword could be effectively used to induce a desired preload in a bolt model.

For more complex models with many solid elements applying the *INITIAL_STRESS_SOLID card to every integration point of every prestressed element becomes more involved. It is not feasible to create all element prestressing by entering the values manually; it is simply too time consuming and inefficient. Rather, a FORTRAN program was created in which the six principal stress components are input by the user, and the program then writes all the DYNA cards for a given input element number data file. The use of this program allows for quick and efficient prestressing of a large number of solid elements. Refer to APPENDIX A to view the FORTRAN program.

7.3.2 Using Prestressed Solid Elements for Bolt Preload

The next step in the process involved applying prestress to the bolt shaft elements of a simplified single-bolt model. A new FE bolted joint model, designated Jnt-3, was created in HyperMesh that incorporated the bolt head, bolt shaft, and nut as an integrally meshed solid body. The bolt shaft itself was given the diameter of the thread root, or thread minor diameter, because this is the tensile stressed area of an actual bolt. The bolt shaft length was modeled at its installed length with the slip base plates and washers stacked between the bolt head and nut. In this model the mating surfaces of the bolt head, washers, slip base plates, and nut were placed coincident with each other to minimize the gaps or “slop” between the components. Refer to Figure 60 to view the Jnt-3 model geometry.

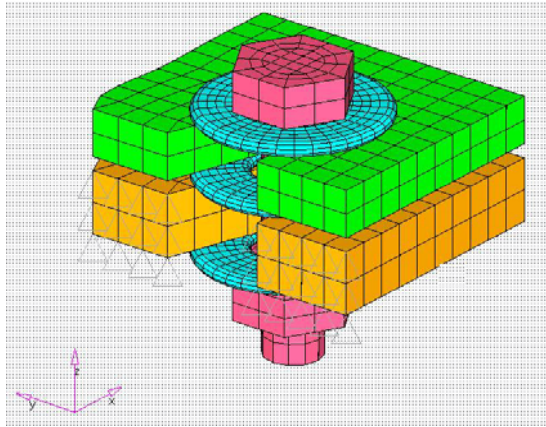


Figure 60. LS-DYNA Model Jnt-3, Clamping Technique #3

As in the Jnt-2 validation, the Jnt-3 joint clamping model consisted of a single bolt clamping together the slip base plates. The FORTRAN program was used to apply a prestress of 0.335 GPa to every integration point of every solid element in the bolt shaft. 0.335 GPa is a stress level just under the yield stress defined in the material model of 0.37431 GPa. The cross-sectional area of the shaft is 87.5 mm². Using the $\sigma=F/A$ relation, the resultant tensile load in the bolt shaft should be about 29.3 kN. During the Jnt-3 simulation the load in the bolt shaft was initially 29.3 kN, but decreased as the deformable plates compressed allowing the bolt shaft to contract slightly. As the bolted joint reached a state of static equilibrium, a final bolt preload of about 11 kN was obtained. Figure 61 displays the bolt preload as recorded in the secforc data file.

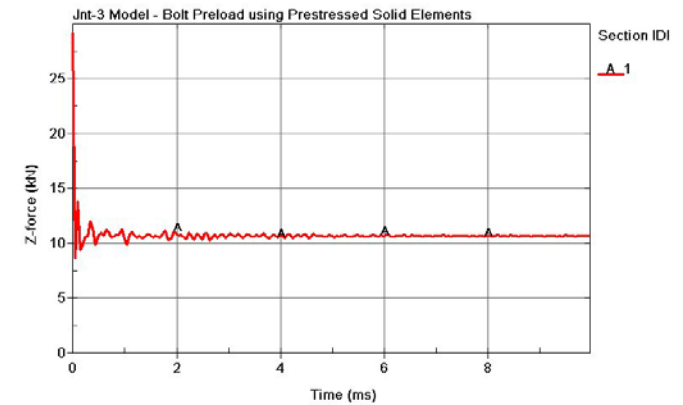


Figure 61. LS-DYNA Secforc Data, Preload Verification of Model Jnt-3

It is noted that in cases where deformable members are being clamped together, it is possible that the deformation of the members may result in an unacceptable loss of preload. In these cases, a higher initial stress may be required. However, the user must be aware that assigning prestress higher than the yield of the material will create initial yielding of the material. In this case, the user must either increase the yield strength of the material model, or change the material definition to a material that can handle higher initial stresses.

It is also important to note that the Jnt-3 model requires iteration in order to obtain the desired preload. Like the Jnt-2 model, the clamping force causes the slip base plates to compress slightly, creating very small bolt shaft deflections. Due to the high stiffness of the bolt shaft material, this small deflection translates into significant loss of tensile load. Therefore, iteration of the prestress values may be required in order to converge on the desired preload value.

Based on the Jnt-3 preload simulation results, it was concluded that this third and final clamping technique has demonstrated its ability to accurately and consistently produce the desired preload for the clamping of a bolted joint. Like the Jnt-2 model, the Jnt-3 model will likely require a few iterations in order to attain a final desired preload. Using prestressing of solid elements for achieving joint preload is a theoretical improvement over the Jnt-2 model, as well as the NCAC and TTI slip base models, because it captures the actual physics and material mechanics which take place in the components of a bolted joint.

8 SLIP BASE COMPONENT TESTING and SIMULATION

8.1 MTS Pull-test Data

The MTS tensile testing machine, as displayed in Figure 62, was used to gather physical force-deflection data for a bolted connection. A jig having the slip base geometry and surface characteristics was constructed to fit in the MTS machine. The jig consisted of two galvanized steel plates with a V-notch for a single bolt to slip through. The plates were separated by a zinc-coated washer, and bolted together with a 0.500-13 UNC bolt which was torqued to 25.8 ft-lbf (35 N-M) using a calibrated torque wrench. Refer to jig drawing in Figure 63 and the jig photographs in Figure 64. As the tests ran, a load cell recorded the resisting slip force generated between the mating surfaces of the slip base jig, and a displacement transducer recorded the position of the moving head. The tensile testing of the slip base jig was intended to provide the actual shear characteristics of a one-quarter model of the actual slip base.



Figure 62. MTS Machine with Slip Base Jig

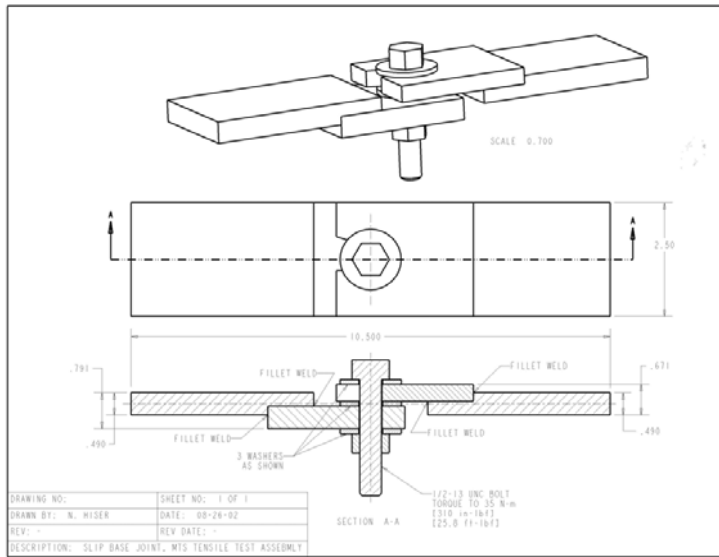


Figure 63. CAD Drawing of Slip Base Jig

The heads of the MTS machine were programmed to separate with a prescribed velocity. Tests were conducted at two velocities; one to simulate quasi-static slip behavior, the other to simulate dynamic slip behavior. The quasi-static test velocity was set at 0.1 in/sec (0.00254 mm/ms). The MTS machine has safety switches that limit its maximum velocity, so the maximum velocity attainable for the dynamic test condition was 10 in/sec (0.254 mm/ms). Once the slip base plates had fully separated, the resisting load fell to zero, and the test was terminated. Figure 68 shows the test sequence.

The jig was reused in each pull-test, however, the bolts, nuts, and washers were replaced after every test. Because of the importance of the galvanized surface finish on the slip base jig flange plates, after each test the plates were sprayed with a cold

galvanizing spray and allowed to fully dry prior to conducting the next test. The use of cold galvanizing spray is very important because it deposits a fine layer of zinc particles on the surface of the steel, which like an electroplated zinc coating, is generally known to significantly reduce the friction coefficient. Note the silver zinc coating in the slip base jig photographs shown in Figure 64.



Figure 64. Slip Base Jig, Front and Side Views

In chapter 4.3 the torque-tension relation was discussed. Because it was not possible to obtain the actual torque-tension relationship for a ½-13 UNC bolt, a preload value was estimated using existing data and engineering judgment. The final judgment was based on the empirical results obtained for other sized bolts, along with analytical calculations, and time-tested industry experience. As seen in Figure 21 and Figure 22, the data sets from Belter et al, and the Utah Department of Transportation are most closely approximated using equation 4.2. The main difference between this and other analytical methods deals with the coefficient of friction specified during calculation. As previously stated, the analytical techniques are extremely sensitive to changes in coefficient of friction. Over the years, a friction value of 0.184 has proven to give the most consistent preload results for as-delivered bolts in a high production environment.

For a 0.500-13 UNC slip base bolt torqued to 25.8 ft-lbf (35 N-m), equation 4.2 yields a preload of 2567 lbf (11420 N). The empirical data taken by Belter et al., and the Utah Department of Transportation shows that the actual preload values for slightly larger sized bolts is about 5-10% below the analytical values obtained by equation 4.2. Also, the optical image analysis from the pressure paper test revealed a preload of about 2235 lbf (9940 N). Furthermore, previous testing has shown that the standard deviation of actual preload test values was at best 10%. Thus, the value obtained from equation 4.2 of 2567 lbf (11420 N) was reduced by 5%, and given a tolerance of about 10%, yielding a final preload value of 2439 ± 225 lbf ($10,850 \pm 1,000$ N). This is the nominal value of preload that will be used in the remainder of this study for 0.500-13 UNC slip base bolt torqued to 25.8 ft-lbf (35 N-m).

In Figure 65 the force-deflection curves for the quasi-static test case are displayed. The data shows an initial peak load that decreases with initial displacement, where the curves appear to momentarily flatten out at what is assumed to be the dynamic slip load value before decreasing to zero in a somewhat linear fashion. It is believed that the initial peak force values correspond with the static coefficient of friction, and the subsequent reduction and momentary flattening of the curve (between 5 and 10 mm) corresponds to the transition from static to dynamic friction. The curves then decrease to zero in a generally linear fashion as the bolt slides out of the groove, losing preload as the washers slowly deflect and lose contact with the V-notched flange surfaces. It is speculated that if the V-notch had parallel sides and were considerably longer, the bolt would not lose preload as the plates slipped relative to one another, and the force-displacement curves would not decrease to zero, but rather flatten out and remain constant at the dynamic slip load value.

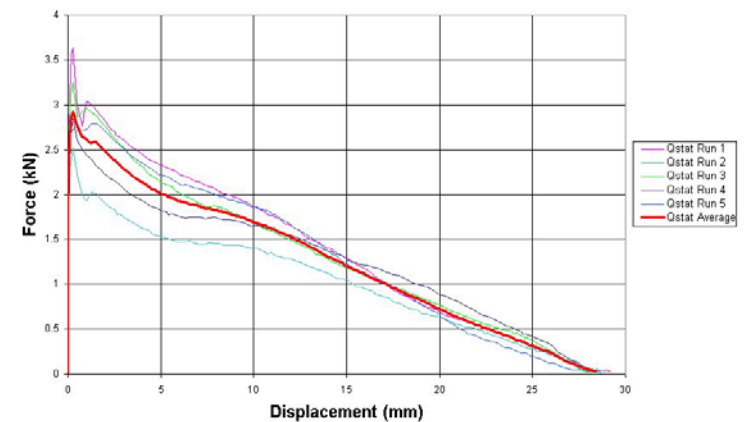


Figure 65. Force vs. Displacement, Quasi-static MTS Pull Test Data

The quasi-static curves of the various test runs generally follow the same trend and coincide well, with the variation reasonably explained by the inherent variation in bolt preload and surface characteristics. As displayed in the graph, the averaged force-deflection curve has a peak load of about 2.9 kN. Knowing that frictional load is calculated $F_s = f_s * N$, where the preload $N = 10.85$ kN, the static friction coefficient is calculated to be $f_s = 0.134$. Also displayed on the graph, the somewhat flattened slip load is about 1.8 kN. Calculation of the dynamic coefficient of friction from $F_d = f_d * N$ yields a dynamic coefficient of friction of $f_d = 0.083$. These averaged values for static and dynamic friction coefficients correspond reasonably well with previously published values (18-19).

In Figure 66 the force-deflection curves for the dynamic test case are displayed. The data shows an initial peak, followed by a generally linearly decreasing slip load until the slip base jig flanges have completely separated. Again, these curves coincide reasonably well, with the discrepancy logically explained by the inherent variation in bolt preload and surface characteristics. Unlike the smooth data in the quasi-static case, the test data recorded in the dynamic case is uneven and choppy, which likely resulted from the rapid plate separation. Because the event happens so rapidly, there does not appear to be a flattening of the slip load after the peak load, indicating that the data did not capture the static to dynamic transition. Therefore, only a single friction coefficient can be found. Using the peak slip load value of about 3.9 kN from the averaged data curve, and the estimated preload value of 10.85 kN, the friction coefficient f_s can be calculated from $F = f_s * N$. The calculation yields a static friction coefficient of 0.180, which corresponds reasonably well with published friction values (18-19). This value is about 35% higher

than that obtained from the quasi-static case above. At this increased velocity it can be reasonably inferred that other factors, such as instantaneous misalignment of the bolt or galling of the surfaces, may cause an increase in the slip load. Note that previous laboratory testing has yielded “effective” coefficients of friction in the vicinity of 0.5 for actual slip base activation, which accounts for various mechanical interactions of the slip base components, such as bending moments and mechanical binding. (16).

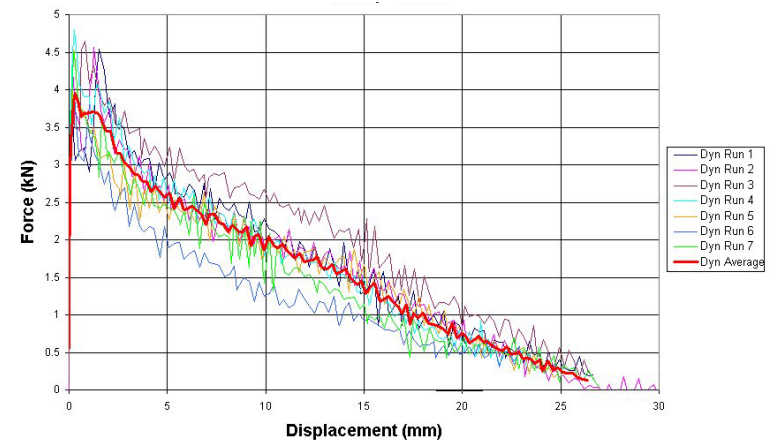
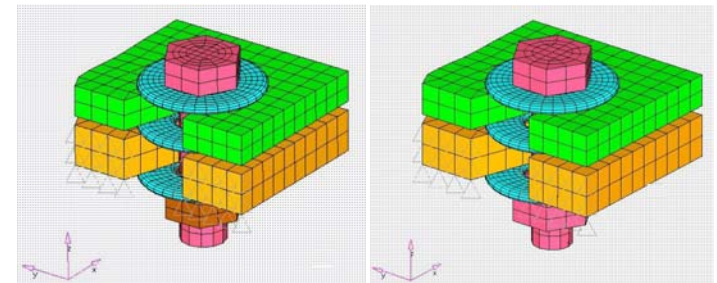


Figure 66. Dynamic MTS Pull Test Data, Force vs. Displacement

8.2 LS-DYNA Pull-test Simulations

Following the MTS pull testing, LS-DYNA was used to simulate the dynamic pull test previously described. Because the quasi-static case takes place at 0.1 in/sec over a time span of about 15 seconds, it was not possible to reproduce this event with simulation in LS-DYNA. The dynamic case, however, takes place at 10 in/sec over a time span of approximately 0.1 seconds, which is well within LS-DYNA’s capability.

Two of the validated joint preload models, Jnt-2 and Jnt-3, as previously described and validated in Chapter 7, were used in the pull test simulations. The simulated bolts were tensioned to about 11,000 kN as previously verified using the secforc data in Chapter 7. Average friction values of $f_s=f_d=0.15$ were initially specified for the pull test simulations. This is the approximate average friction value obtained from the actual pull test data previously discussed, and it is also a commonly published empirical friction value for zinc-plated steel on steel. The bottom plate of both the Jnt-2 and the Jnt-3 models were constrained with single point constraints at all nodes along the face in the $-X$ direction, and the top plate was given a prescribed velocity of 10 in/sec (0.254 mm/ms) in the $+X$ direction to replicate the actual MTS pull test. Figure 67 displays the quarter slip base joint models that were used for the pull test simulations. Note that the Jnt-2 model utilizes an independent nut, whereas the nut is an integral member of the bolt in the Jnt-3 model. Figure 68 illustrates both the the actual and simulated pull test sequence, which proved to be very similar. The slip force vs. displacement data for both the Jnt-2 and Jnt-3 simulations are displayed in Figure 69. It is apparent from the similarly shaped curves that the Jnt-2 and Jnt-3 models, with their different clamping methods, are very similar in terms of force vs. displacement slip behavior in a parallel pull test.



Jnt-2 Model

Jnt-3, Jnt-4 Model

Figure 67. Pull Test Simulation, Slip Base Joint Models

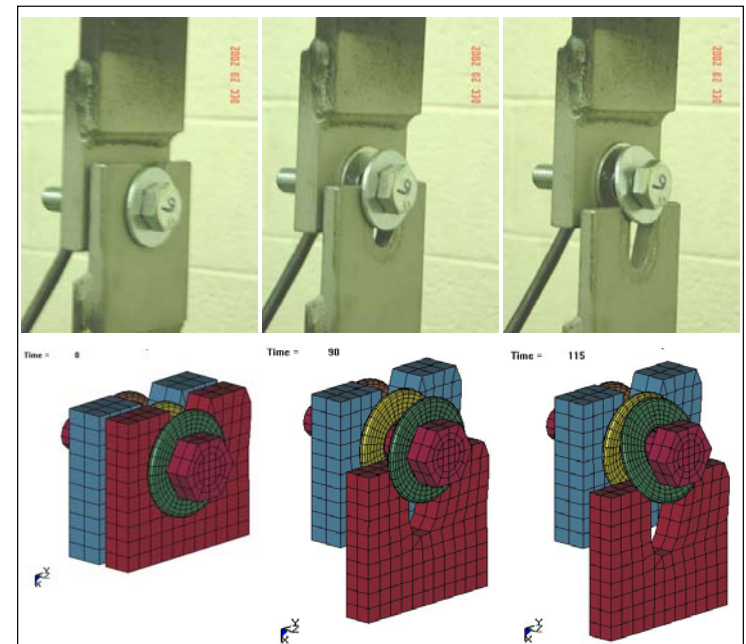


Figure 68. MTS Pull-test and Simulation Sequences

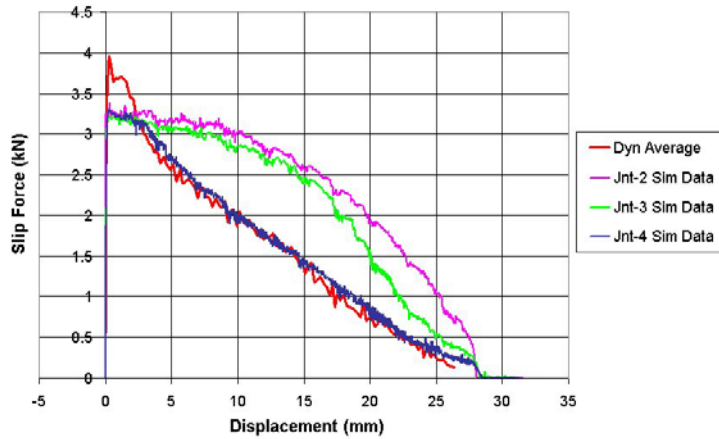


Figure 69. Slip Force vs. Displacement Simulation Data

As is evident in Figure 69 of the reforc data, the peak slip force resisting the motion of the top plate is seen to be about 3.25 kN. This is verified with the knowledge that a frictional force follows the following relation:

$$F_s = \mu * N$$

where F_s is the slip force, μ is the coefficient of friction, and N is the normal force, or clamping force. In the case of the top plate, there are two normal forces, N , which act on top and bottom of the plate due to contact with washers on both sides. Thus the theoretical frictional force is:

$$F_s = 2 * (\mu * N) = 2 * (0.15 * 11) = 3.3 \text{ kN}$$

It was noted that the Jnt-2 and Jnt-3 slip force data did not exactly coincide with the actual pull test averaged data curve. While the actual pull test data generally followed a linearly decreasing trend, the simulated slip force data followed a somewhat parabolic

trend. Further insight determined that the difference in the shape of the physical and simulated slip force curves could reasonably be explained by the fact that the simulations used rigid washers, while in reality the washers are deformable. Consider the following theory: As the washer slips out of the gradually widening V-notch groove, the cross-section of the washer is subjected to an increased bending moment from the preloaded bolt. This increased bending moment in the washer causes the washer to deflect at its center, in turn allowing the bolt to contract, losing preload in the bolt. With loss of bolt preload (normal force), the frictional slip force decreases proportionally. However, because the simulations used rigid washers, the loss of preload due to washer deflection was not considered, and therefore, only the preload loss due to deflection of the plates was present.

To test the above theory, the Jnt-3 pull simulation was repeated with designation Jnt-4, and the top washer was assigned deformable steel material properties identical to the plate material properties. All other variables were identical to Jnt-3. As is apparent in Figure 69, the deformable top washer greatly improved the correlation between the physical pull test data and the simulated pull test data. The slip force curve for the Jnt-4 simulation generally displays a linearly decreasing trend that overlays the average dynamic slip force data. The average dynamic slip force data displays an initial peak slip force that was not captured by the simulation. Recall that the friction coefficients were specified as $f_s = f_d = 0.15$ for the simulated pull tests of Jnt-2, Jnt-3, and Jnt-4.

In an attempt to capture the peak slip force observed in the actual pull test data, the Jnt-4 model was given a static coefficient of friction of $f_s = 0.20$, while the dynamic friction coefficient remained at $f_d = 0.15$. The resulting slip force data curve had the same

shape as the previous run with $f_s=f_d=0.15$; however, there was a significant increase in noise within the data, verifying a previous claim by Bala in an LSTC contact modeling publication (37). Because the increased static friction coefficient did not capture the peak force seen within the dynamic test data, and also increased the amount of noise in the data, it was concluded that equal static and dynamic friction coefficients would be used in all subsequent slip base simulations.

Although the use of a deformable washer greatly improved the slip behavior of the simulated pull test model Jnt-4, its use is not practical for this study due to the increase in computational time. The computational time increased by a factor of 1.91 (from 9979 sec to 19075 sec) due to the decrease in computational time step from 0.2 micro-sec to 0.1 micro-sec. The increase in computational time resulted from the washer's deformable material specification and the small element mesh size. The washer's mesh size and geometry has previously been developed and validated in terms of contact stability and its ability to accurately capture frictional slip forces. Therefore, at this point in the development of a slip base model, a compromise was made. The finely meshed washer must be rigid in order to remain practically useful for LS-DYNA simulations during this study. Although a time step of 0.2 micro-sec is significantly below the generally desired time step of 1.0 micro-sec, its use was deemed practical to achieve the overall goals of this study. For future studies which utilize hardware having greater computational speeds, or studies which require highly accurate results, the use of the deformable washer model, having a time step of 0.1 micro-sec, may be beneficial.

Even though the use of rigid washers in the LS-DYNA pull test model creates some discrepancy in the force-displacement slip force curve relative to the actual data,

the force required to initiate slip (3.25 kN) is the same. The energy dissipated due to the overall slip event is also of some interest. The energy dissipated during the pull test event is the area under the force-displacement curve. The actual energy dissipated during the MTS pull test was estimated by measuring the area under the average dynamic slip force curve, which was calculated to be about 50 kN-mm. LS-POST was used to perform the integration for the Jnt-2 and Jnt-3 simulations, and the result was a total energy dissipation of 65 and 60 kN-mm respectively, which was in reasonable agreement with the test data. It is noted that the energy dissipation values can be altered in simulation by either modifying the friction coefficients or the preload values.

It was concluded that the simulated pull-test models Jnt-2 and Jnt-3 reproduced the force-displacement characteristics, and thus energy dissipation, of the bolted joint with acceptable results using friction coefficients of $f_s=f_d=0.15$ and rigid washers. These models will be used in subsequent slip base simulations. Although exceptional force-displacement correlation was attained with the Jnt-4 model using deformable washers, their use may be unwarranted in most circumstances due to increased computational cost.

9 SLIP BASE MODELING – RIGID CYLINDER IMPACT

9.1 Sb-1 Post and Slip Base Model

The first, and most simplified, slip base model was developed during prior research conducted by Paulsen et al, and reproduced in a similar fashion by Hiser and Paulsen for reference in this study (42). The Jnt-1 clamping technique was integrated into the Sb-1 post and slip base model. The Sb-1 model consisted of two slip base flanges modeled with shell elements, between which bolt tension was simulated using four nonlinear discrete springs placed in the location of the bolts. The springs were given a non-linear load curve to coincide with the bolt preload due to torque, and was given a failure displacement of 20 mm, which is the slip distance of the actual slip base. Steel-on-steel friction was defined between the slip base plates.

The Sb-1 slip base model was not independently pursued in this study, as are the subsequent Sb-2 and Sb-3 models. Rather, it was previously developed in conjunction with an entire cable guardrail end terminal system simulation which will be discussed in detail in Chapter 10. The main focus of this study was to develop highly detailed slip base models that would capture the actual mechanical interactions of the unidirectional slip base and behave appropriately for a host of impact conditions. Therefore, the remainder of this study will be dedicated to the development of new slip base modeling techniques rather than refinement of the existing Sb-1 model.

The Sb-1 slip base model theory has several limitations. Most notably, the modeling simplifications of the Sb-1 model results in multi-directional slip base behavior, that is, it acts the same if impacted from all directions. The actual slip base mechanism is unidirectional in that its design allows it to activate in the weak direction (slip), but puts

forth significant resistance along the strong post axis (non-slip). Therefore, it is concluded that the Sb-1 model would require additional development to add features to make it behave in a unidirectional manner.

9.2 Sb-2 Post and Slip Base Model

The Jnt-2 clamping model was first developed and tested in Chapter 7.2, and then tested in a pull-test simulation with the results presented in Chapter 8.2. Based on the results of these two tests, it was concluded that the Jnt-2 model exhibited acceptable clamping and slip behavior. The Jnt-2 clamping technique was then integrated into a larger 4-bolt post and slip base model of the cable system end terminal for further validation. This model was designated Sb-2.

The Sb-2 model was modeled after the actual cable support post and slip base shown in Figure 5 in Chapter 2. The model consisted of two steel slip base flanges modeled with deformable solid elements and bolts for clamping as in the Jnt-2 model as developed in Chapter 7.2. The slip base flanges were connected to the support and base I-beam posts using *CONTACT_TIED_NODES_TO_SURFACE. The I-beam post was modeled with shell elements per a previous study by Fating (43). The lower base post was constrained at ground level using single point constraints. The cable hanger was modeled with solid tetrahedron elements, and it was given rigid material properties because deformation of this component was not observed in actual impact testing. The Sb-2 post and slip base model is displayed in Figure 70.

The Sb-2 post and slip base model was first used to verify the individual bolt preload and the total clamping force on the slip base flanges. Following bolt preload

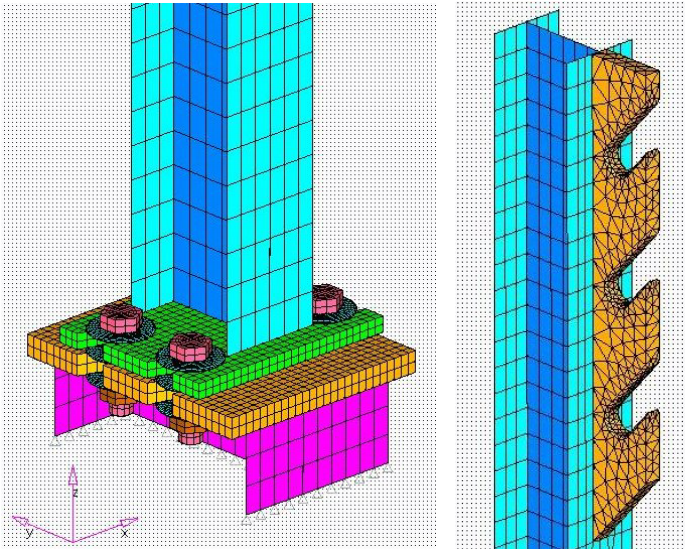


Figure 70. Sb-2 Post and Slip Base FEA Model.

verification, the post was impacted with a rigid cylindrical contact entity traveling at 10.5 mm/ms (23.5 mph) at the base of the post at a height of 136.5 mm above the slip plane. The rigid cylinder was given a prescribed displacement motion resulting in constant cylinder velocity throughout the impact event. The location and size of the impact cylinder are displayed in Figure 71. The low impact height was initially deemed necessary to minimize the moment produced on the slip plane in order to isolate the shear/slip behavior. The influence of a moment on slip base behavior is investigated at a later time.

Figure 72 shows the clamping force due to each individual discrete spring element from the deforc data as the simulation progressed, as well as the total clamping load from

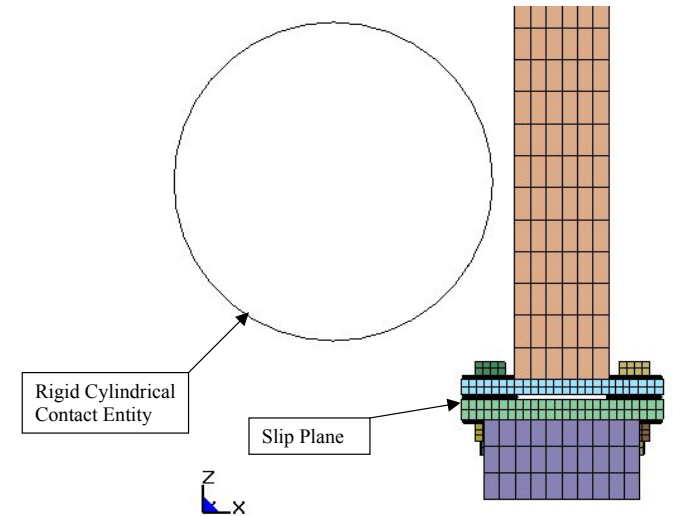


Figure 71. Sb-2 Post and Slip Base and Rigid Impact Cylinder

the secforc data as recorded with a horizontal cross-section through the lower slip base flange. It is apparent that each spring is preloaded to about 11 kN which results in a total slip base clamping force of 44 kN. The impact takes place after 4 ms, making it possible to verify the preload prior to impact. As is evident in Figure 73, the rigid cylinder impacts the post and the slip base activates and separates as desired.

The energy dissipated during the slip base activation is the area under the force vs. displacement curve. LS-DYNA computes the energy in the glstat energy file. Figure 74 is the LS-DYNA output from the glstat energy file, and it clearly shows that the total system energy due to the impact event at time 10 ms was about 1367 kN-mm. Also note that the total energy is the sum of the kinetic energy (504 kN-mm), internal energy (290 kN-mm), and sliding energy (573 kN-mm). Prior to impact the total system energy is the

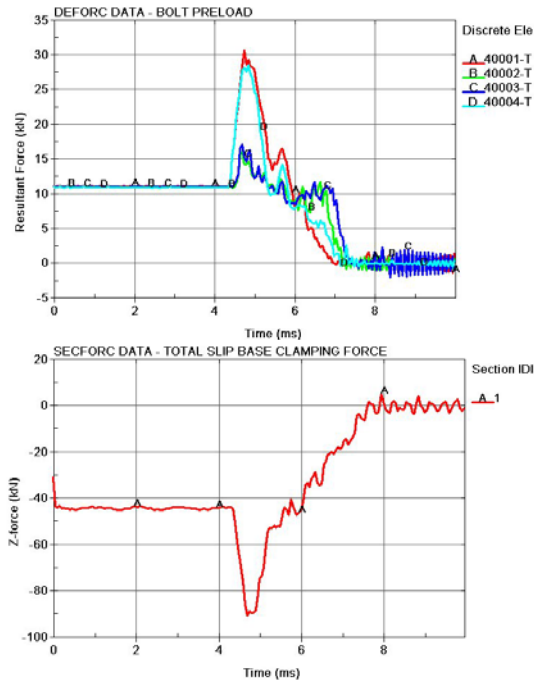


Figure 72. Model Sb-2, Bolt Clamping Load and Total Slip Base Clamping Load

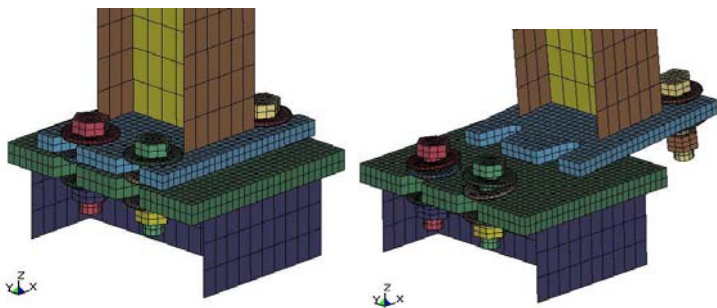


Figure 73. Sb-2 Slip Base Activation when Impacted by Rigid Cylinder

kinetic energy of the rigid cylinder, which was 135 kN-mm. When the total system energy at time 10ms is subtracted from the initial system energy, the result is the energy dissipated due to the impact event, also called the base fracture energy. The base fracture energy for this impact was found to be 1232 kN-mm.

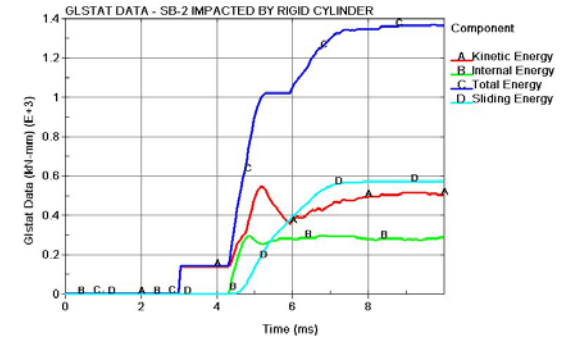


Figure 74. Gstat Energy Data, Sb-2 Post and Slip Base Impacted by Rigid Cylinder

9.3 Sb-3 Post and Slip Base Model

The Jnt-3 clamping model, which used prestressed solid elements to develop bolt preload, was first developed and tested in Chapter 7.3, and then tested in a pull-test simulation with the results presented in Chapter 8.2. Based on the results of these two tests, it was concluded that the Jnt-3 model exhibited acceptable clamping and slip behavior. The Jnt-3 clamping technique was then integrated into a larger 4-bolt model of the three-strand cable guardrail end terminal post and slip base for further validation. This model was designated Sb-3.

The Sb-3 FEA model was nearly identical to the Sb-2 model previously described and displayed in Figure 70, with the exception of the slip base clamping technique. As

opposed to the use of a discrete spring element to develop clamping load, the Sb-3 model utilized prestressed bolt shaft elements to develop preload, as in the Jnt-3 model.

The Sb-3 post and slip base model was first used to verify the individual bolt preload and the total clamping force on the slip base flanges. Following bolt preload verification, the post was impacted with a rigid cylindrical contact entity traveling at 10.5 mm/ms (23.5 mph) at the base of the post at a height of 136.5 mm above the slip plane. The location and size of the impact cylinder are displayed in Figure 71. As before, the low impact height was initially deemed necessary to minimize the moment produced on the slip plane in order to isolate the shear/slip behavior of the full slip base model.

Figure 75 shows the clamping force due to each individual prestressed bolt shaft from the secforc data file as the simulation progressed, as well as the total clamping load as recorded with a horizontal cross-section through the lower slip base flange. It is apparent that each bolt shaft is preloaded to about 11 kN which results in a total slip base clamping force of 44 kN. The impact takes place after 4 ms, making it possible to verify the preload prior to impact. As is evident in Figure 76, the rigid cylinder impacts the post and the slip base activates and separates as desired.

The energy dissipated during the slip base activation is the area under the force vs. displacement curve. LS-DYNA computes the energy in the glstat energy file. Figure 77 is the LS-DYNA output from the glstat energy file, and it clearly shows that the total system energy due to the impact event at time 10 ms was about 1108 kN-mm. Also note that the total energy is the sum of the kinetic energy (476 kN-mm), internal energy (259 kN-mm), and sliding energy (373 kN-mm). Prior to impact the total system energy is the kinetic energy of the rigid cylinder, which was 135 kN-mm. When the total system

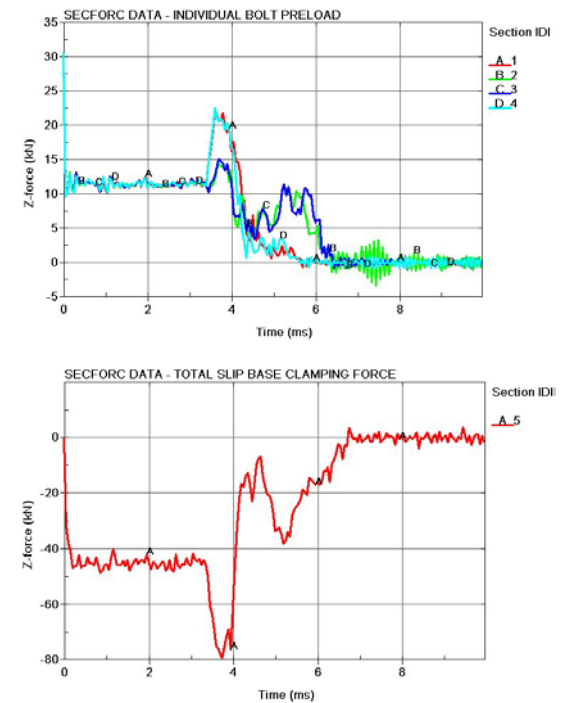


Figure 75. Model Sb-3, Bolt Clamping Load and Total Slip Base Clamping Load

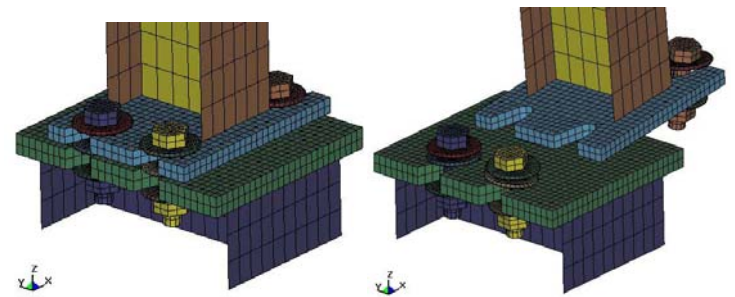


Figure 76. Sb-3 Slip Base Activation when Impacted by Rigid Cylinder

energy at time 10ms is subtracted from the initial system energy, the result is the energy dissipated due to the impact event, also called the base fracture energy. The base fracture energy for this impact was found to be 973 kN-mm.

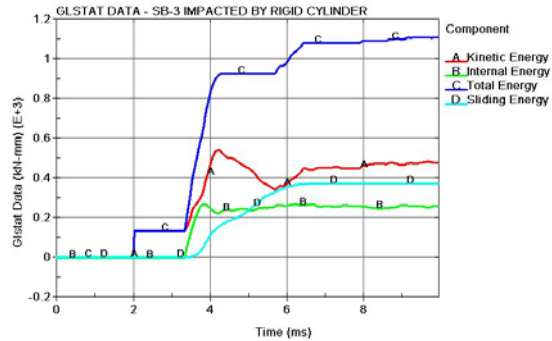


Figure 77. GJstat Energy Data, Sb-3 Post and Slip Base Impacted by Rigid Cylinder

Both the Sb-2 and Sb-3 post and slip base models were impacted at height of 136.5 mm above the slip plane with a rigid cylindrical contact entity traveling at a constant 10.5 mm/ms (23.5 mph). Other critical modeling factors such as clamping load, friction coefficients, contact definitions, material model specifications, and model geometry were identical. The only difference in the models was the clamping techniques. In both cases the slip bases activated as desired, cleanly slipping free of the base, revealing very similar impact behavior. However, comparison of the gjstat files indicates that the Sb-3 slip base model dissipated about 20% less total energy during slip base activation as compared to the Sb-2 model. Even with the energy discrepancy, both models exhibited acceptable slip behavior and were pursued further.

9.4 Comparison of Sb-2 and Sb-3 Slip Base Models

Both Sb-2 and Sb-3 post and slip base models have shown potential for accurately modeling the cable system end terminal slip base impact behavior. These two models were then subjected to bumper height impacts in both the weak (slip) and strong (non-slip) directions with a rigid cylindrical contact entity in order to validate one model for further investigation.

9.4.1 Weak Axis Impact

In the first simulation run both Sb-2 and Sb-3 models were impacted in the weak axis direction (slip direction) at bumper height of 436.5 mm above the slip plane with a rigid cylindrical contact entity traveling at a prescribed velocity of 20 mm/ms (45 mph). The static and dynamic friction coefficients were specified as $f_s=f_d=0.15$. In both cases, the slip base mechanisms “locked-up”. For a second run the friction coefficients were set to $f_s=f_d=0.1$, and the results are as seen in Figure 78 and Figure 79. After some initial slip, the Sb-2 model again locked-up, not allowing the post to break free of the base. The Sb-3, however, activated and cleanly slipped free of the base.

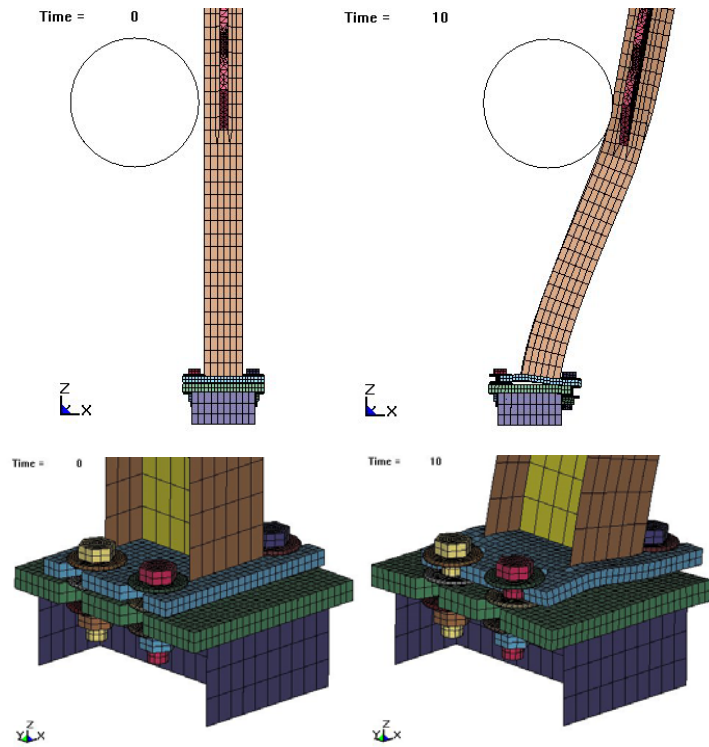


Figure 78. Sb-2 Model Exhibiting Slip Base Lock-up, Weak Axis Bumper Height Impact

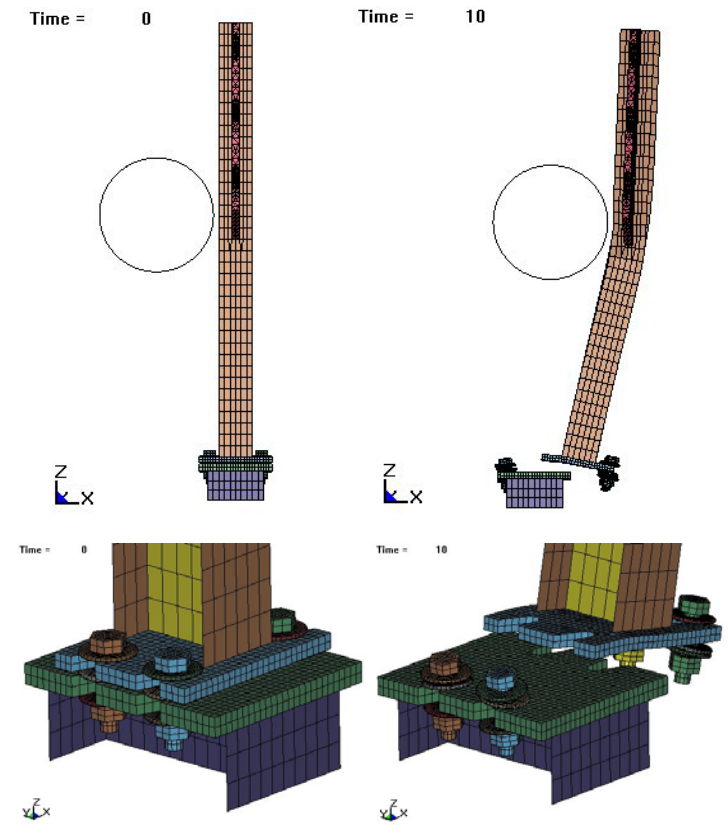


Figure 79. Sb-3 Model, Weak Axis Bumper Height Impact

Upon close inspection of the bolt geometry and the stress fringe plots, it is apparent that the Sb-2 slip base model locked up due to a wedging action, or mechanical interlocking, resulting from the inability of the rigid bolts to deform. On the contrary, slight bolt deformation near the bolt head allows the top plate to cleanly separate without wedging in the Sb-3 slip base model. Figure 80 shows the deformation in the Sb-3 bolt which allows the plate to slip free, while the rigid bolt in Sb-2 binds the plate between the washers. The stress fringe plots in Figure 81 also clearly indicate that the upper flange edges are wedged between the two rigid washers as the upper flange twists out of plane.

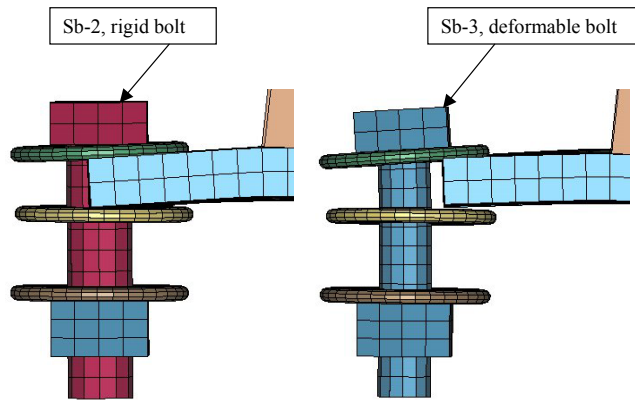


Figure 80. Bolt Comparison During Slip Base Activation, Rigid vs. Deformable

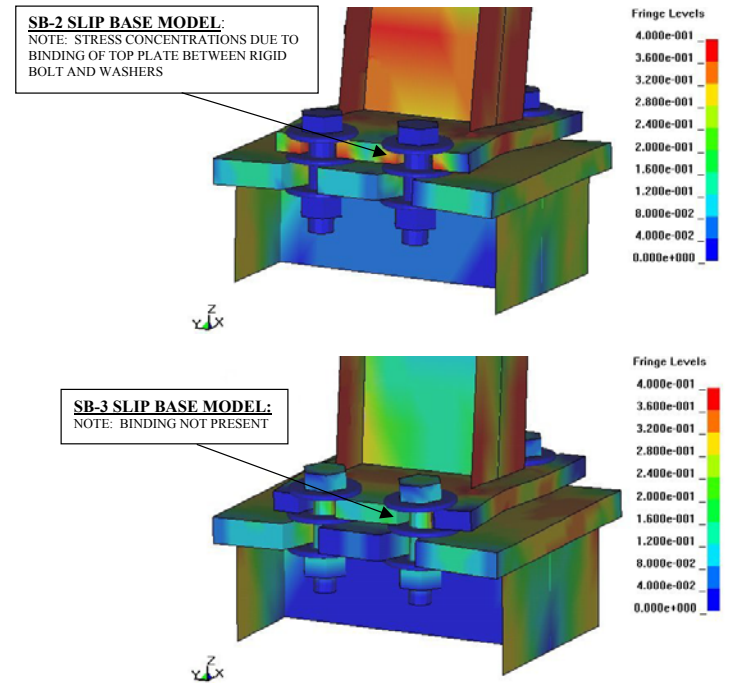


Figure 81. Stress Fringe Plots Indicating Binding of Sb-2

From the previously described simulations, it is apparent that the Sb-2 and Sb-3 models are not equivalent in terms of impact behavior in the weak axis direction. Although both models exhibit similar behavior at the lower impact height at 136.5 mm above the slip plane, at the higher impact height of 436.5 mm above the slip plane, which is typical bumper height, the models exhibit significantly different slip behavior.

The increased impact height produced a significant bending moment on the slip plane, thus changing the loading condition at the slip plane from a pure shear between the flanges to a combination of shear and bending moment. The bending moment on the slip plane caused the upper flange to deform and twist out of plane with the lower flange. It was this bending moment that created additional mechanical interactions in the slip base mechanism, and created mechanical interlocking in the Sb-2 model.

It is apparent that impact height is a major factor that must be considered in slip base impact behavior. An increased impact height subjects the slip plane to an increased moment, which increases the potential for mechanical interlocking of the components. It is apparent that the Sb-2 model which uses rigid bolts is more sensitive to, and not compatible with, the effects of mechanical interlocking. The unrealistic binding/wedging displayed by the Sb-2 rigid bolt model became more apparent as the impact height increased. At the lower impact height, the effects of mechanical interlocking was revealed by an increase in slip energy required to fully activate the slip base. However, at higher impact heights the effects of mechanical interlocking of the flanges resulted in slip base lock-up. It is therefore concluded that the Sb-3 slip base model, which utilizes prestressed deformable bolts, allows for the most realistic overall slip base activation behavior when impacted in the weak axis (slip) direction.

It must be noted that the time step of the Sb-3 model was significantly decreased, nearly doubling the computational cost as compared to the Sb-2 model. It should also be noted that the Sb-2 model could likely be modified to eliminate the lock-up behavior by either decreasing the friction coefficient or the bolt preload for acceptable slip base behavior. However, doing so would limit the ability of the Sb-2 model to accurately

capture the actual mechanical interactions of the slip base mechanism, and thus may render it unsuitable for some impact scenarios.

9.4.2 Strong Axis Impact

In the second round of comparative simulation runs both Sb-2 and Sb-3 models were impacted in the strong axis direction (non-slip direction) at bumper height of 436.5 mm above the slip plane with a rigid cylindrical contact entity traveling at a prescribed velocity of 20 mm/ms (45 mph). The purpose of impacting the two models in the strong axis direction was basically for verification of the bolt behavior when subjected to an extreme loading condition.

As was expected, the Sb-2 model displayed significant deformation in the post and upper flange due to the inability of the rigid bolts to deform or fail. On the contrary, the Sb-3 model resulted in bolt deformation and overload failure of the bolt shafts. Refer to Figure 82 and Figure 83 for the Sb-2 and Sb-3 strong axis impact.

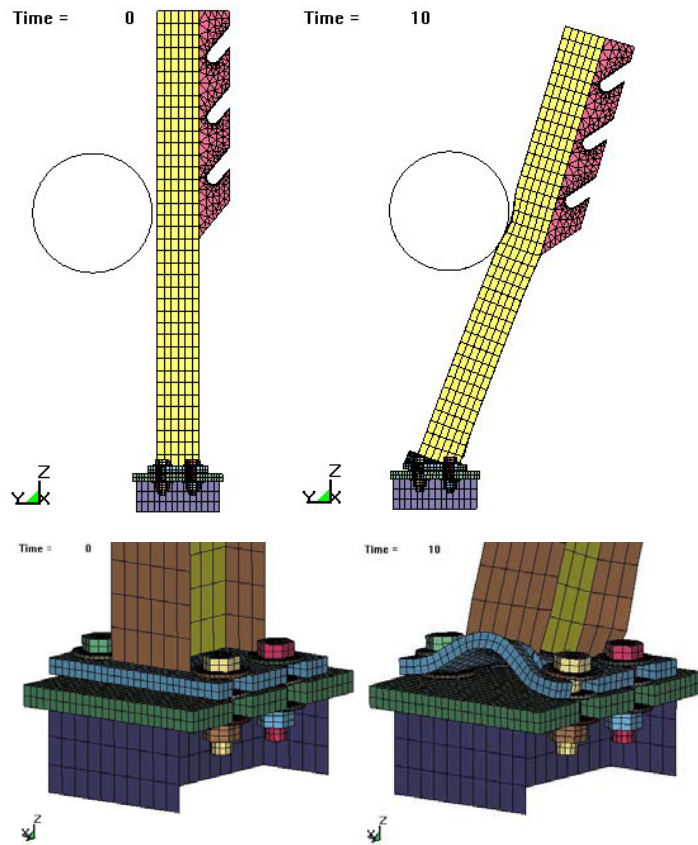


Figure 82. Sb-2 Model, Bumper Height Impact with Rigid Cylinder, Strong Axis

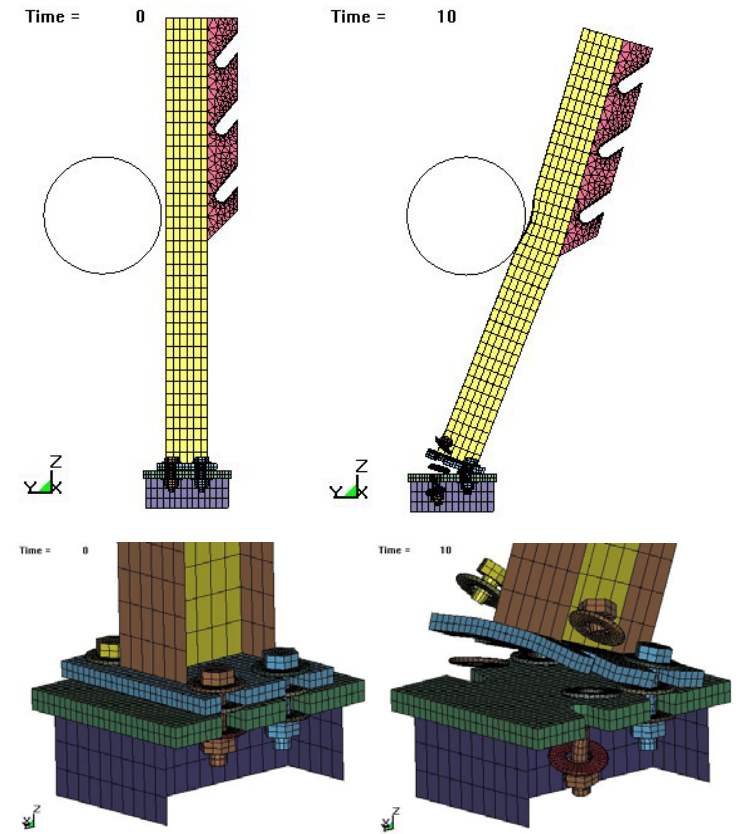


Figure 83. Sb-3 Model, Bumper Height Impact with Rigid Cylinder, Strong Axis

Figure 84 is an illustration of the Sb-3 bolt overload failure which resulted from the use of deformable solid elements. Although the bolt exhibits deformable behavior, it is noted that the bolt appears to have significant plastic deformation uncharacteristic of actual bolt failure. Actual bolts typically fail in a brittle manner. A review of the ASTM material specification for grade 2 bolt steel, as specified in the cable guardrail system, verified that the post steel material model developed by Fating (43) was acceptable for application to the deformable bolts in the Sb-3 slip base model in terms of yield strength and ultimate strength. However, the plastic strain to failure, or ductility, of the LS-DYNA material model is assumed to be significantly higher than would be observed in actual bolt material. Thus, without a validated bolt steel material model, the post steel material model was deemed acceptable.

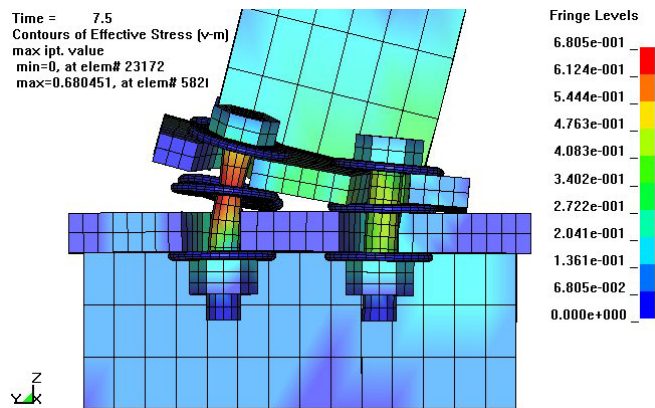


Figure 84. Sb-3 Model Bolt Failure, Bumper Height Impact, Strong Axis

9.4.3 Conclusions

From the results of both the weak and strong axis impacts at bumper height, it is concluded that the assumptions and simplifications made in the Sb-2 model resulted in a model with limitations regarding its ability to reproduce the physical mechanics of the actual slip base mechanism. The limitations imposed on the Sb-2 slip base model resulted in unrealistic slip base lock-up, and bolts that do not deform when subjected to an extreme loading condition. In weak axis impacts the simplifying assumptions may often be valid and result in acceptable overall slip behavior. However, it is conceivable that uncommon strong axis impacts may produce extremely unrealistic results with the Sb-2 model. The Sb-3 model, which utilizes prestressed deformable bolt elements, captures a higher sense of realism regarding the bolt preload method and the physical behavior of the bolt shaft itself. The justification in using such a detailed model is in its ability to capture realistic slip base behavior in both common and uncommon impact events. Thus, the Sb-3 slip base model was chosen for use in subsequent full scale impact simulations for further model validation.

10 END TERMINAL IMPACT SIMULATIONS

In the previous chapter it was determined that the Sb-3 post and slip base model exhibited the most realistic overall slip base behavior, both in theory and during simplified impact simulation. The Sb-3 model was then incorporated into the three strand cable guardrail end terminal model that would be used to validate the Sb-3 post and slip base model in a full-scale end-on impact simulation.

The end terminal model was initially developed by Hiser and Paulsen in a prior study along with the Sb-1 post and slip base model (42). As was indicated in Chapter 9.1, the further development of the Sb-1 model was not pursued in this study in lieu of the more detailed Sb-2 and Sb-3 slip base models. However, the development of the end terminal system model using the Sb-1 model will be presented herein for completeness.

10.1 Sb-1 End Terminal Development and Simulation

As previously described in Chapter 2, the Midwest Roadside Safety Facility is currently developing a crashworthy end terminal for the common three-strand cable guardrail. The design goal was to disengage the pretensioned cables at the end anchor point upon impact with a vehicle, activating the end post and slip base, and thus allowing the vehicle to pass through the system virtually unobstructed. Refer to Figure 5 in Chapter 2.5 for an illustration of the end terminal design.

In order to test the initial end terminal design concept, the CTB-4 bogie crash test was conducted. A 3-strand cable system was built with a prototype crashworthy end terminal design, and was impacted longitudinally with a 900 kg bogie vehicle traveling at 20.1 m/s (45 mph). The bogie vehicle bumper contacted the cable release lever at 400 mm above the ground. The CTB-4 crash test was conducted without any data acquisition

equipment other than the use of high-speed film, and still photographs prior to and following the impact. Refer to Figure 85 for photos of the 3-strand cable system, prototype end terminal, and bogie vehicle used in bogie test CTB-4.



Figure 85. CTB-4, Prototype End Terminal and Bogie Vehicle

It was the objective of this portion of the study to simulate the cable terminal bogie test CTB-4 using LS-DYNA and validate the simulation results with that of the physical test. The LS-DYNA end terminal model was initially developed using the Sb-1 slip base model previously described in Chapter 9.1. The Sb-3 slip base model was later integrated into the end terminal system for model validation.

In order to simulate the CTB-4 crash test in LS-DYNA, the cable system end terminal had to first be modeled in HyperMesh and LS-DYNA, during which many approximations and simplifications were made. Refer to Figure 86 for an illustration of the final end terminal system FEA model.

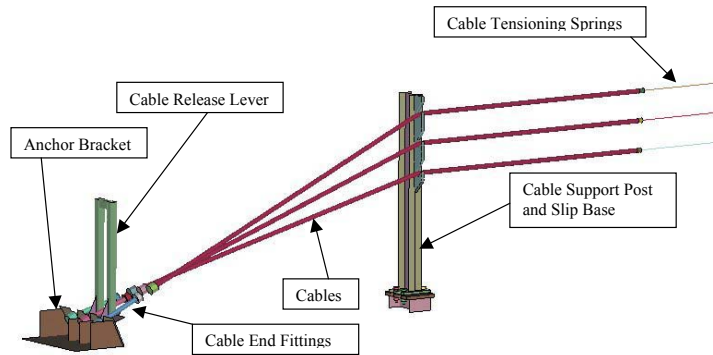


Figure 86. Three-strand Cable Guardrail End Terminal FEA Model

First to be modeled was the cable anchor bracket, which was modeled exclusively using deformable shell elements to represent the grade 250 steel plate from which the actual bracket was constructed. All of the nodes on the base-plate of the anchor bracket model were constrained in all 6 degrees-of-freedom to simulate a rigid anchor bracket base. In LS-DYNA, fillet welds were added to the anchor bracket at the top two nodes of the vertical gussets where weld failure was observed in the physical tests.

The cable release lever was also modeled entirely with deformable shell elements to represent the grade 250 rolled steel tube and steel plate from which the actual lever

was constructed. The lever was placed upright on the anchor bracket gussets without any constraints present.

A cable model, provided by Dr. John Reid, was utilized in this study. Both solid and discrete beam elements were used to model the cable. A circular cross-section was cut into eight pie-shaped elements, and was then extruded to create solid, 6-node elements. Discrete beam elements were placed at the center of the solid elements, and each beam element spanned the length of one solid element. The beam elements were used to resist a majority of the tensile load in the cable model, and the solid elements were used to provide mass distribution, bending stiffness, and improved contact with other components.

Discrete spring elements, with a spring rate of 80 N/mm and an initial offset of 50.8 mm, were attached to the end of each cable downstream of the end post to simulate the compensating springs which tension the cables. The compensating springs are to induce a specified load of 4064 N per cable. The cables were extended 3 feet past the end post in order to obtain acceptable global system behavior while limiting computational time.

The cable end fittings were modeled with deformable solid elements and a pie-shaped cross-section consistent with the cable. Additional solid elements were added to represent the volume and mass of the threaded rod, nuts, washers, and shackle which make up the cable end fitting. Using LS-DYNA, a rigid body spherical joint with 20° rotation was placed between the cable and the cable end fitting to simulate the actual degrees of freedom allowed due to the presence of the shackle. In order to incorporate a spherical rigid body joint between the cable and cable end fittings, rigid elements were

required at the ends of both cable and end fittings. Figure 87 illustrates the cable end fitting modeling approximation.

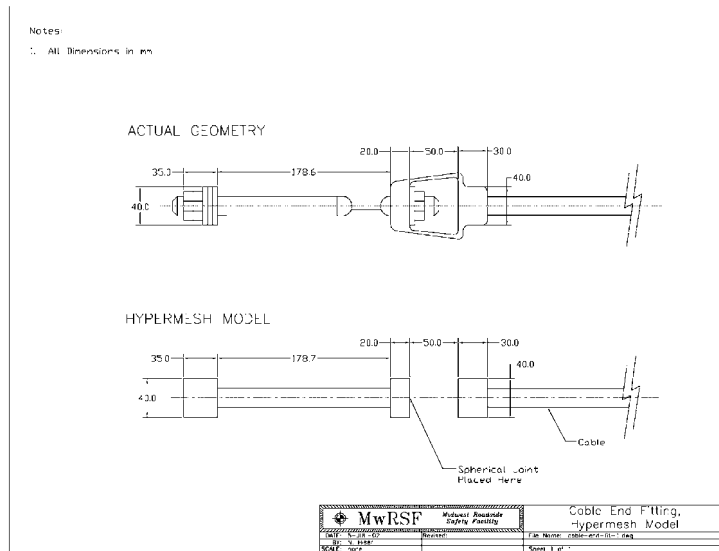


Figure 87. Cable End Fitting Modeling Approximation

The bogie model, acquired from Dr. John Reid, required a bumper modification. The bumper used in CTB-4 was constructed of HDPE, and it was mounted at a height of 400 mm to match that of a small car bumper, such as a Geo Metro. The majority of the bumper was modeled with rigid, solid elements primarily for mass and geometric correlation. Deformable, solid elements with the *MAT_ELASTIC material definition were placed along the leading edge of the bumper. The presence of relatively soft, deformable elements on the leading edge of the bumper helped to reduce the peak contact

forces that typically occur upon impact. A photograph of the bogie used in CTB-4 is shown in Figure 85.

Finally, the Sb-1 post and slip base model as described in Chapter 9.1 was incorporated into the end terminal system.

Visual comparison of simulation results with photographs and high-speed video from the bogie test was used to validate the simulation. The cable end fittings were properly released from the anchor bracket with the cable release lever, thus eliminating the tension in the cables, and preventing the vehicle from ramping up the tensioned cables. The Sb-1 slip base model constrained the post from slipping and twisting until activation by bogie impact, failing in manner consistent with observed behavior from the test film. In short, it was concluded that the LS-DYNA end terminal model with the Sb-1 slip base produced acceptable overall system behavior in the end on bogie impact. Please refer to *Simulation of Cable Terminal Bogie Test CTB-4* by Hiser and Paulsen for a detailed end terminal model validation (42).

10.2 Sb-3 End Terminal Simulation

The Sb-1 model in the previously validated cable system end terminal model was next replaced by the more detailed Sb-3 post and slip base model. Automatic single surface contact was again used for all contacts in the simulation, however, they were assigned separately in order to allow for various friction coefficients. From previous validation the slip base components required friction coefficients of $f_s=f_d=0.10$, the anchor bracket required coefficients of $f_s=0.74$ and $f_d=0.57$, and there was no friction specified between the cables and cable hanger. All other modeling details were consistent with the end terminal impact using the Sb-1 slip base model. The end terminal

simulation using the Sb-3 slip base was conducted, and an identical validation was performed using the new simulation results. The end terminal and slip base validation is outlined below.

Ideally, accelerometer data would be used to compare energy loss in the actual bogie to the simulated bogie, however, since this data was not recorded, the next best validation technique is visual comparison. Time comparison between digital video of CTB-4 and the simulation is the main validation used for this model. Plastic deformation of the cable end fittings, end post, and anchor bracket was a second method used to validate the CTB-4 simulation.

The cable end fittings were released from the anchor bracket with the cable release lever, thus eliminating the tension in the cables, and preventing the vehicle from ramping up the tensioned cables. The Sb-3 slip base model constrained the post from slipping and twisting until activation by bogie impact. Upon impact with the bogie, the slip base activated and failing in manner consistent with observed behavior from the test film.

Certain physical characteristics of the CTB-4 bogie test were chosen and used for validation of the simulation. Rotation of the cable release lever, the time of fillet weld failure, and the time of contact with the post can all be closely inspected using high-speed film. In a more subjective manner, the global impact behavior of the cable end fittings, cables, and post were used as secondary validation techniques. Figure 88 shows time comparisons of the actual and simulated end terminal test CTB-4.

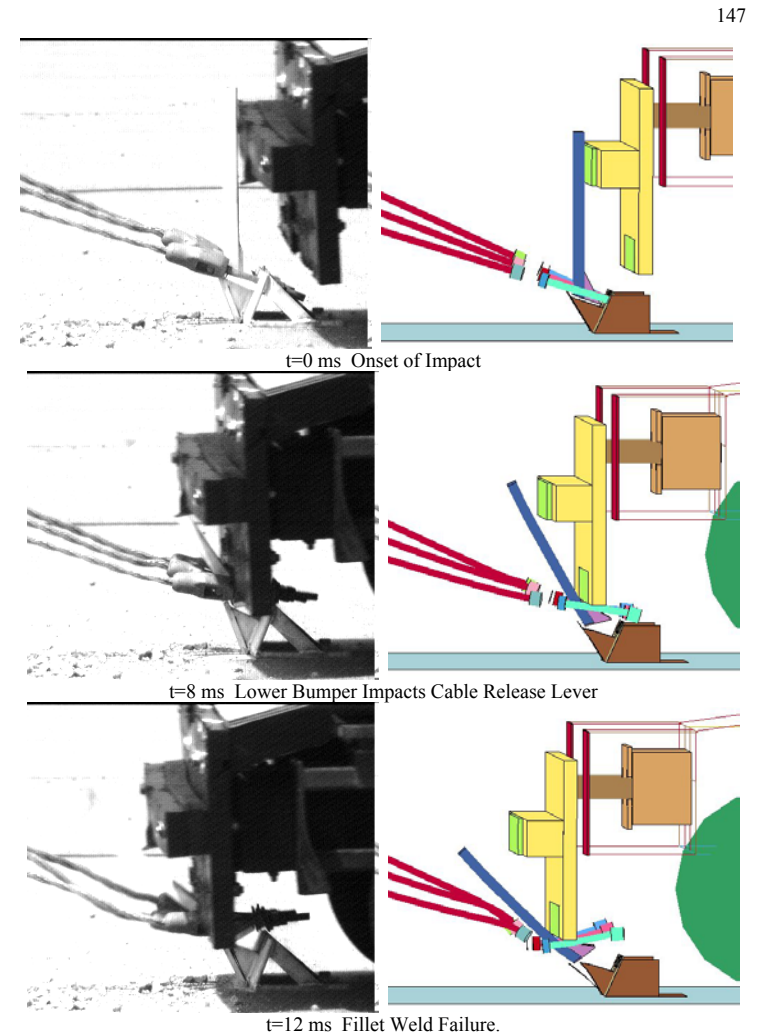
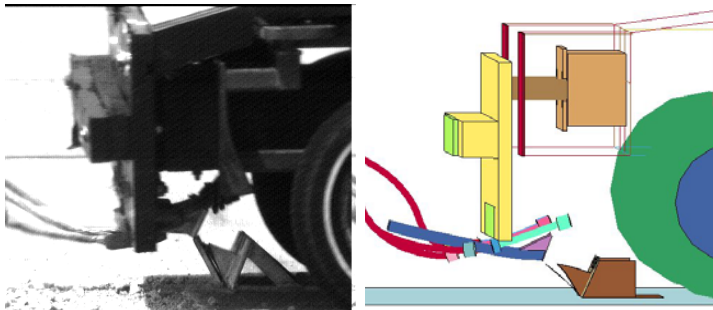
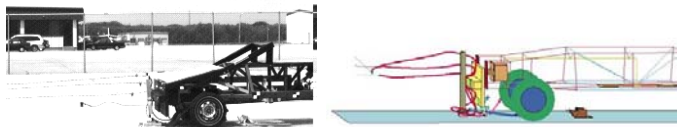


Figure 88. Time Comparison, High-Speed Film vs. LS-Dyna Simulation



t = 18 ms Cable Release Lever Loses Contact with Anchor Bracket



t=70 ms Post impact



t=80 ms Post Releases from Slip Base

Figure 88 (Continued). Time Comparison, High-Speed Film vs. LS-DYNA Simulation

When viewing the time comparisons, certain details were inspected for simulation validation. The lower part of the bumper contacts the cable release lever at 8 ms in both the simulation and the video. The fillet welds fail at 9 ms into the simulation, but they did not fail in the video until 12 ms. However, the video was recorded at 500 frames per second, so it is possible that the weld failed within the range of 10 to 12 ms. At 18 ms, the cable release lever has almost lost contact with the anchor bracket, and it was nearly

parallel with the ground, which is evident in both the simulation and the video. The simulation accurately shows that the bogie made contact with the post at approximately 70 ms. Following the bogie impact with the post and the slip base activation, the post trajectory in both the simulation and video corresponds reasonably well.

The bolt preload clamping forces from the secforc data files also verified that the slip base performed as intended. Note in Figure 89 that the impact occurs at about 70 ms, separating the slip base flanges and eliminating the 11 kN tensile loads in the bolt shafts. A single cross section through all three cables, as displayed in Figure 90, revealed that the sum of the cable tension was initially about 12 kN, indicating the cables were properly tensioned to about 4 kN each prior to the release of cable tension at about 5 ms.

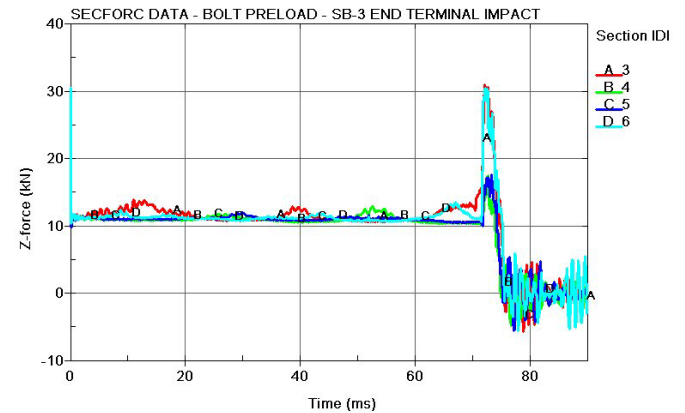


Figure 89. Individual Bolt Preload During Sb-3 End Terminal Impact

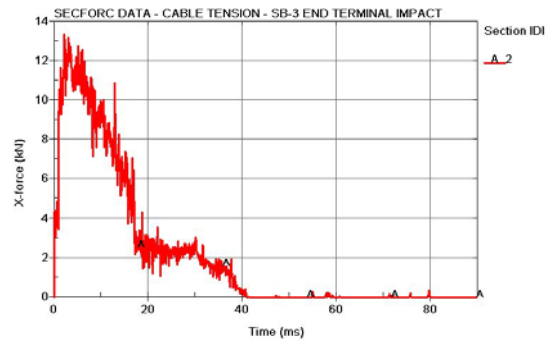


Figure 90. Total Cable Tension During Sb-3 End Terminal Impact

The slip base was also closely inspected to ensure it exhibited acceptable activation behavior. Figure 91 shows the Sb-3 slip base activation and separation during the impact. There was not dedicated video on the slip base, so a step-by-step validation was not possible. However, visual verification of the slip base behavior indicated the slip base was performing as intended.

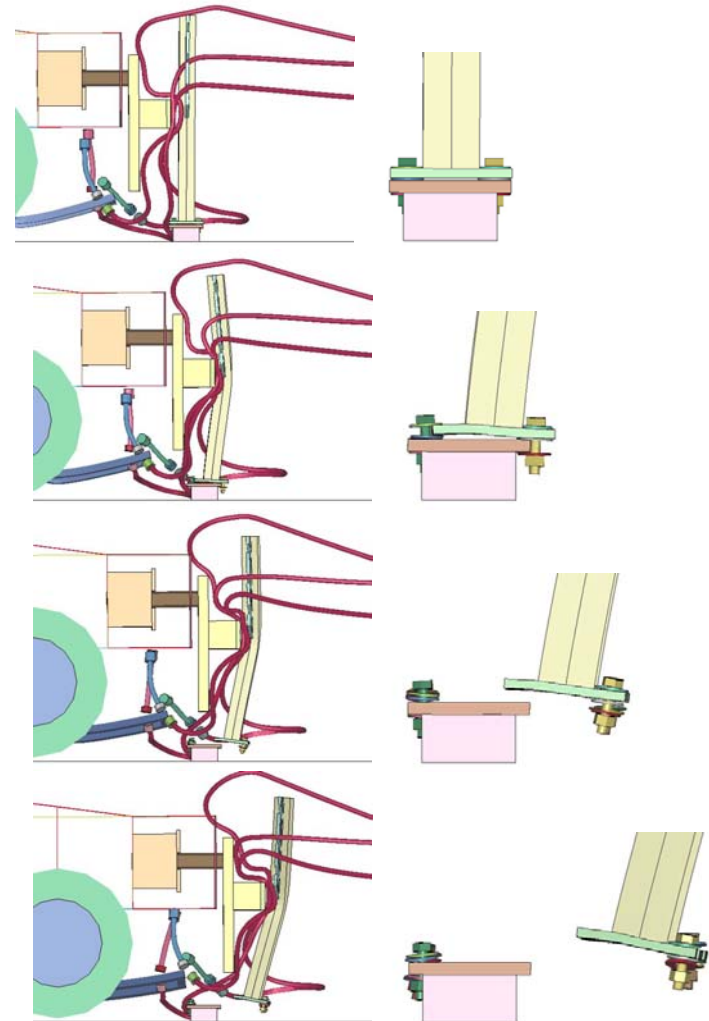


Figure 91. Sb-3 Slip Base Activation Sequence, End Terminal Impact

Permanent post, cable end fitting, and anchor bracket deformations were also compared for simulation validation, as shown in Figure 92. It is apparent from the visual comparison that the deformations observed in the damage photos coincides reasonably well with the simulation results.

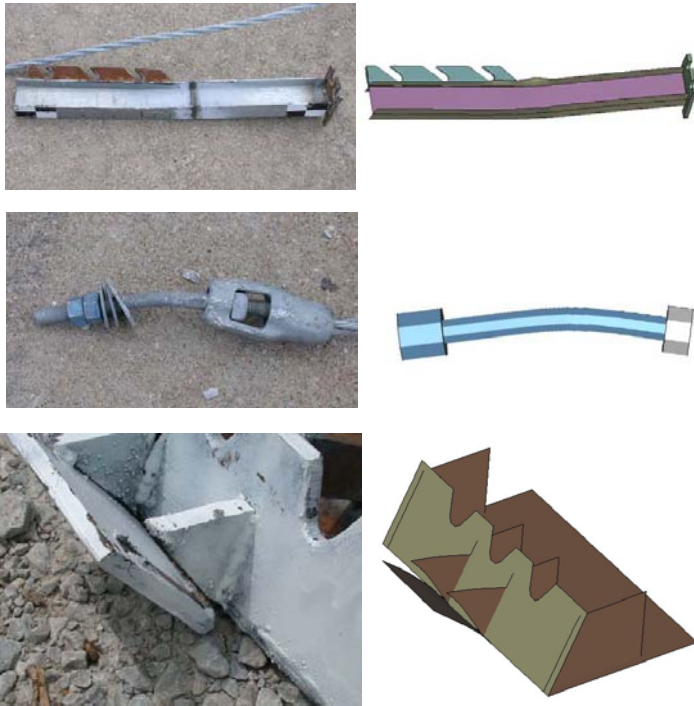


Figure 92. Deformation Comparison - Post, Cable End Fitting, and Anchor Bracket

From the previous detailed evaluation of the end terminal impact, it is concluded that the LS-DYNA end terminal model produced acceptable overall system behavior in the end terminal bogie impact. More importantly for this study, the Sb-3 post and slip base model performed as intended in the end terminal impact. A slip base clamping force of 11 kN per bolt was properly applied by the prestressed bolt models. The Sb-3 slip base model constrained the post during the simulation until activation by bogie impact, failing in manner consistent with observed behavior from the test film. A significant moment was produced on the slip plane due to the high impact location on the post. This moment caused the upper slip base flange to deform and twist out of plane relative to the bottom flange, as seen in Figure 91. Even so, the ability of the bolts to deform minimized the potential for mechanical interlocking of the slip base components, allowing the upper flange to slip free and fully separate as it would in reality. It is concluded that the Sb-3 slip base model performed acceptably in the end terminal impact, and further validation with a length-of-need impact should be pursued.

11 LENGTH-OF-NEED IMPACT USING SB-3 SLIP BASE MODEL

The Sb-3 slip base model has previously been incrementally validated from an initial joint clamping simulation, to a tensile pull-test simulation, to both a strong and weak axis impact with a rigid cylinder, and finally in a full-scale end terminal bogie impact. The final validation for the Sb-3 post and slip base model came in a full-scale length-of-need impact on the MwRSF cable guardrail system.

11.1 CT-1 Test Results

The length-of-need impact is typically conducted on the section of guardrail system that is immediately downstream of the system end terminal. The length-of-need impact is intended to demonstrate the guardrail system's ability to adequately contain and redirect the impacting vehicle, as well as test the system's anchorage system for structural integrity. The MwRSF cable guardrail system was subjected to a length-of-need impact in the CT-1 full-scale test for validation of the end terminal design. The CT-1 test was conducted with a 2000 kg pickup truck impacting the cable guardrail system at a 20° angle and traveling at a velocity of 63 mph (28 m/s). Figure 93 shows the CT-1 test setup and impact location on the cable guardrail system.



Figure 93. CT-1 Length-of-Need Test Setup and Impact Location

During the CT-1 test, the pickup impacted the system at post number 3, which is the first standard system post. Upon weak axis impact, the line posts fail as intended without snagging the vehicle, and the cables separate from the line posts with failure of the J-bolts. Tension in the cables increased as the truck penetrated behind the face of the system, and the cables properly captured the front end of the vehicle. When the tension in the cables increased to sufficient levels, the truck was smoothly redirected. The end terminal adequately anchored the system during the impact and subsequent vehicle redirection. The cable support post and slip base provided sufficient strength in the strong axis direction to assist in redirection, and the bearing strut provided sufficient vertical load resistance. It was concluded that the cable guardrail system end terminal with slip base provided adequate anchorage for length-of-need impacts. Figure 94 shows the cable system following the CT-1 test.



Figure 94. Aftermath of CT-1 Length-of-Need Crash Test

The only forces that acted on the cable support post and slip base resulted from the tension in the cables. The cable tension supplied three components of force on the cable hanger. First, there was a force component acting in the longitudinal (slip) direction due to friction between the cable and cable hanger. Second, there was a force component acting in the lateral (non-slip) direction due to penetration of the vehicle behind the face of the cable system. Finally, there was a force component in the vertical direction due to the sloping of the cables to the anchor bracket. The magnitude of each component is dependent upon the resultant cable tension and direction of action, where direction is primarily dictated by vehicle penetration distance. Figure 95 is a plot of the

total cable tension, as recorded by load cells during the CT-1 crash test. It is apparent that the maximum load generated in all of the cables during impact was about 25 kips (110 kN).

Test No. CT-1: Load Cell Data Total Load Versus Time

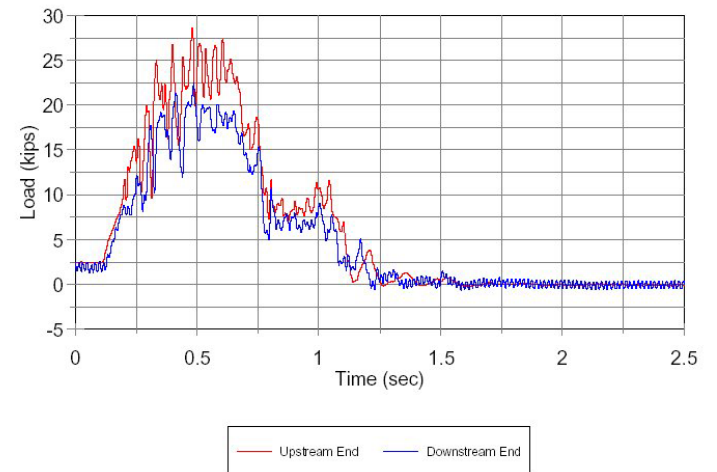


Figure 95. CT-1 Cable Tension Load Cell Data

Close inspection of the slip base revealed bolt and washer damage on the outboard side of the slip base flanges. This damage indicated that the cable tension produced a significant moment on the slip plane about the post's strong axis, causing some overloading of slip base mechanism in the non-slip direction. Figure 96 shows the slip base damage resulting from the CT-1 crash test.



Figure 96. CT-1 Slip Base Damage

11.2 Lon-1 Length-of-Need Impact Simulation

The Sb-3 post and slip base model, along with the cable system end terminal model, were then inserted into a larger cable system model by Dr. John Reid. The larger model consisted of a long stretch of cables mimicking the length of the actual cable system, as well as model of system post number 3. All the remaining downstream system posts were not included in the model because they have minimal influence on the ability of the end terminal and cable support post and slip base to anchor the system during redirection of the impacting vehicle. However, it is noted that the absence of line posts reduces the resistance of the cable system to vehicle penetration, and thus reduces the ability of the system to dissipate impact energy during redirection.

The first length-of-need simulation, designated Lon-1, was conducted using a rigid bogie vehicle with mass of 800 kg, traveling at 34 mph (15 m/s), and impacting the cable system at a 20° angle. The bogie vehicle impacted the cable system at the same impact location as the CT-1 test. Refer to Figure 97 which displays the Lon-1 model. The simulation was terminated when the vehicle was fully redirected.

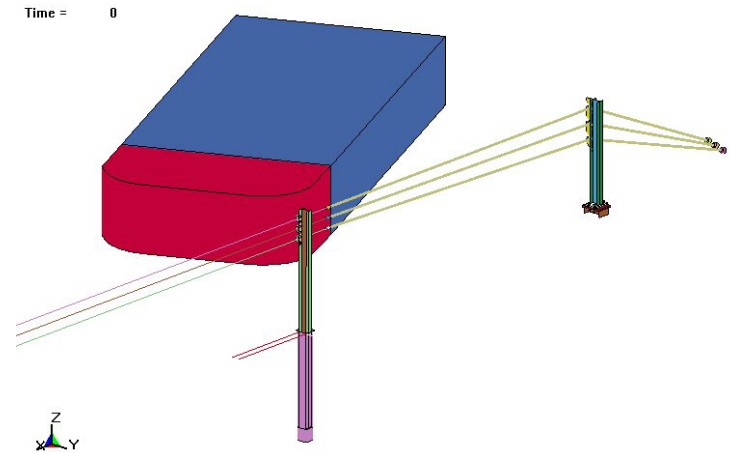


Figure 97. Model Lon-1 and Lon-2, Cable Guardrail System Length-of-Need Impact

The length-of-need simulation results of primary concern for this study was the cable tension and direction of action, and the resulting slip base behavior. Because the direction of cable action is nearly identical for all simulations in this study, as well as the CT-1 crash test, it is considered a constant for all cases within this investigation, and will be neglected for the remainder of this study. Therefore, the only variable of concern for this study is the magnitude of the cable tension. Figure 98 is the secforc data which reveals the cable tension during the impact, and Figure 99 shows the Sb-3 slip base model at time 400 ms following the bogie redirection.

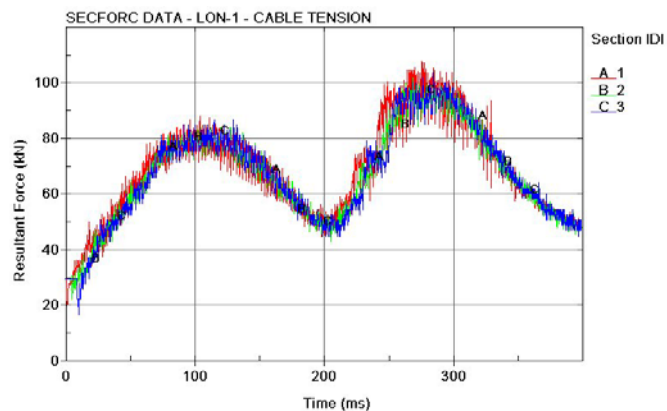


Figure 98. Model Lon-1, Secforc Data, Cable Tension

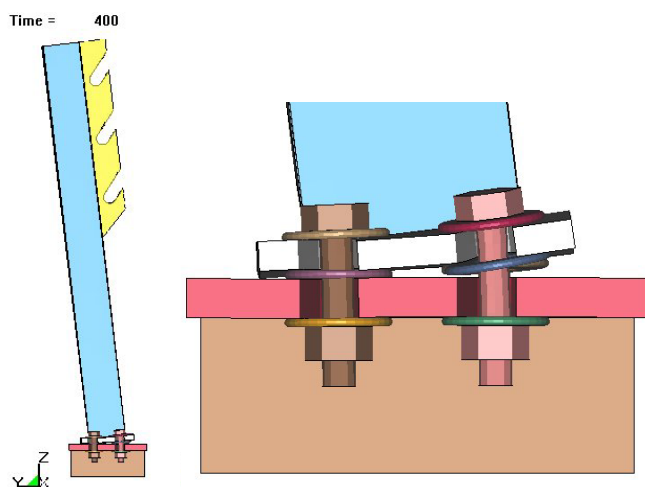


Figure 99. Model Lon-1, Sb-3 Post and Slip Base Following Impact

As is evident in Figure 98, the maximum cable tension resulting from the Lon-1 impact was about 100 kN, which was very near the 110 kN maximum tension as recorded during the CT-1 crash test. The double peaks in the load curve correspond to the initial impact of the front of the bogie vehicle, and the “tail slap” from the rear as it is redirected. Although the Lon-1 simulation has significantly less energy during the impact due to reduced vehicle mass and velocity, the cable tension, and thus, the loads as felt by the Sb-3 post and slip base model were comparable. The comparable tensile cable loads generated at reduced energy levels in simulation likely resulted from the removal of the standard line posts. Without the line posts there is less resistance to vehicle penetration and minimal energy dissipation to the system posts, resulting in higher energy transfer to the cables themselves, and higher cable tension. Other factors may include accelerated loading behavior of the cable model, and unrealistically high frictional forces generated between the bogie and the cables.

The Sb-3 slip base model retained the post, and thus the cables, throughout the impact. As the bogie penetrated behind the system, a force component of the cable tension created a moment about the strong post axis, and also on the slip plane. As is evident in Figure 99, this moment highly loaded the bolts on the outboard side of the slip base flanges causing permanent deformation, and similarly to the CT-1 crash test, caused some overloading of the slip base mechanism in the non-slip direction. However, because the washers are not deformable in the LS-DYNA model as they are in reality, the failure mode was transferred to the bolts, rather than the washers. Overall, the Lon-1 impact was successful, as it validated the usefulness of the Sb-3 slip base model.

11.3 Lon-2 Length-of-Need Impact Simulation

The second length-of-need simulation, designated Lon-2, was identical to Lon-1 except that the velocity of the bogie vehicle was increased to 28 m/s (63 mph). Refer to Figure 97 which displays the Lon-2 model and impact location. As before, the simulation was terminated when the vehicle was fully redirected.

The tensile load generated in the cables, as well as the slip base behavior, was investigated. Figure 100 is a graph of the secforc data, which revealed a maximum cable tension of about 175 kN. This is significantly higher than the actual tensile cable loads from the CT-1 crash test, as shown in Figure 95. This is evidence that the Sb-3 post and slip base model were subjected to excessively high loads during the Lon-2 simulation.

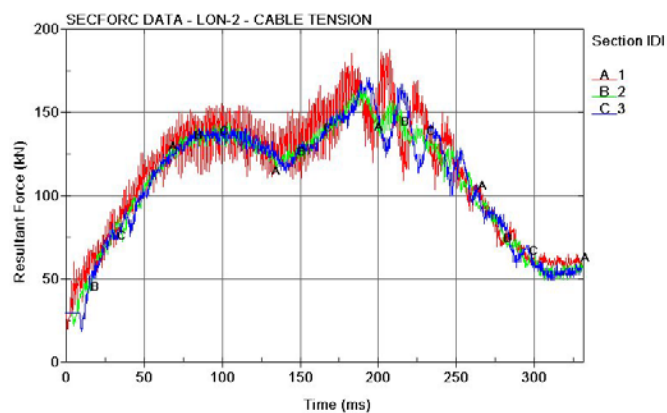


Figure 100. Model Lon-2, Secforc Data, Cable Tension

Figure 101 displays the results of the excessively high cable tension in the Lon-2 simulation. The moment created by the cable tension about the strong post axis resulted in overload and failure of the slip base bolts. Because of the high cable loads, and the

resulting moment produced on the slip plane, it was determined that the Lon-2 simulation represented an extremely severe loading condition. The results of the Lon-2 simulation reveal that there does exist an upper limit of impact severity that the Sb-3 slip base model can withstand. Although this result does not directly validate the Sb-3 slip base model, it does illustrate its potential benefit as a predictive tool.

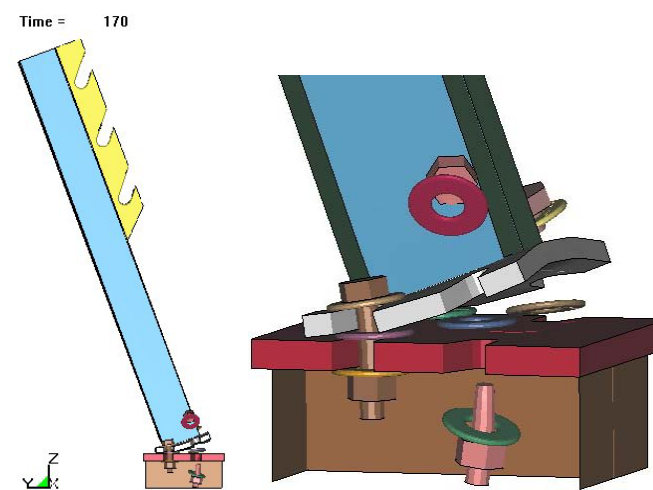


Figure 101. Model Lon-2, Sb-3 Slip Base Failure Following Impact

11.4 Lon-3 Length-of-Need Impact Simulation

The third and final length-of-need impact simulation conducted was designated Lon-3. Because of the limitations inherent in the rigid bogie vehicle used in Lon-1 and Lon-2, it was determined that an impact with an actual pickup truck model would be beneficial. Dr. John Reid of the University of Nebraska-Lincoln has developed a detailed C-2500 pickup model in LS-DYNA, and it was this model that was used for the Lon-3

simulation. It has previously been shown that the cable system model produces higher cable loads at lower impact energy levels due to the absence of the line posts. Because of this, the Lon-3 pickup truck simulation was conducted at 34 mph (15 m/s), rather than the CT-1 crash test velocity of 63 mph (28 m/s). Figure 102 illustrates the Lon-3 model and impact location.

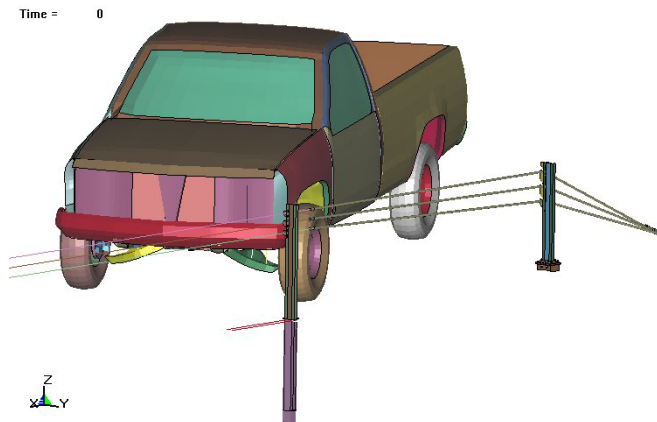


Figure 102. Model Lon-3, Cable System Length-of-need Impact, Pickup Truck Model

Figure 103 displays the Lon-3 impact sequence. Time zero shows the initial impact location and the impacting angle. Note that the impact point is at post three, which is the first standard system post. As the impact progresses, post three deflects rearward, but retains the cables and continues to supply lateral resistance during the redirection. Post number two, which is the cable support post and slip base, also deflects somewhat, but remains anchored to the slip base, providing redirection resistance as well. At time 300 ms the cables have captured the vehicle's bumper, and redirection has begun. The simulation was terminated at time 500 ms once redirection was complete.

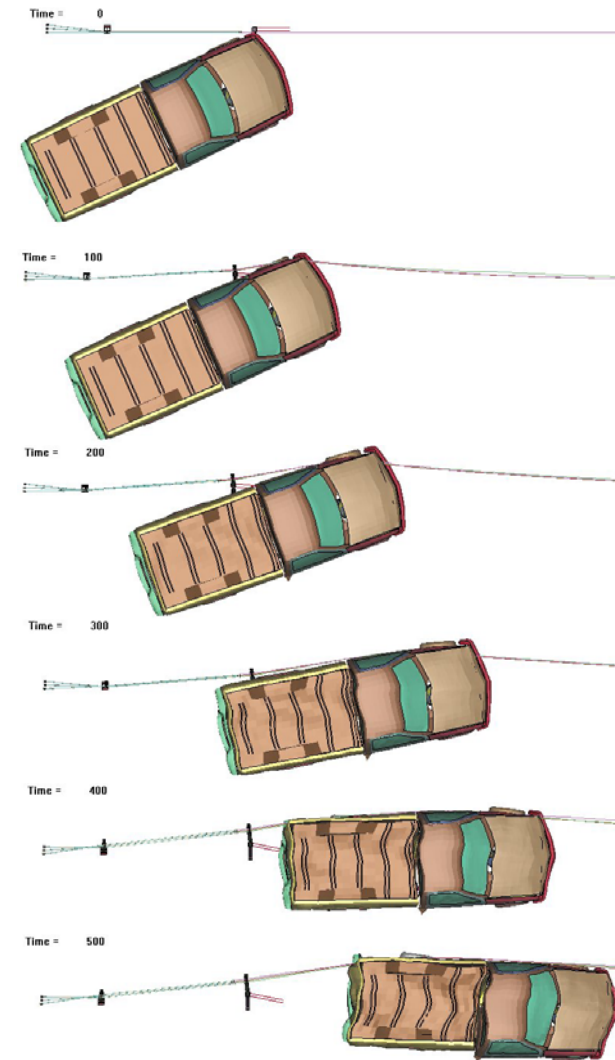


Figure 103. Model Lon-3, Cable System Length-of-need Impact Sequence

Figure 104 is a plot of the secforc data through the cables. The data indicates a maximum tensile load of approximately 130 kN was generated in the cables at time 500 ms. The flattening of the load curve at 500 ms indicated that redirection is complete, which justified termination of the simulation. Although the Lon-3 simulation has significantly less impact energy than the CT-1 crash test due to reduced vehicle velocity, the cable tension, and thus, the loads as felt by the Sb-3 post and slip base model are about 20% higher. The increased tensile cable loads in the Lon-3 simulation produce a more extreme slip base loading condition than was present during the CT-1 crash test.

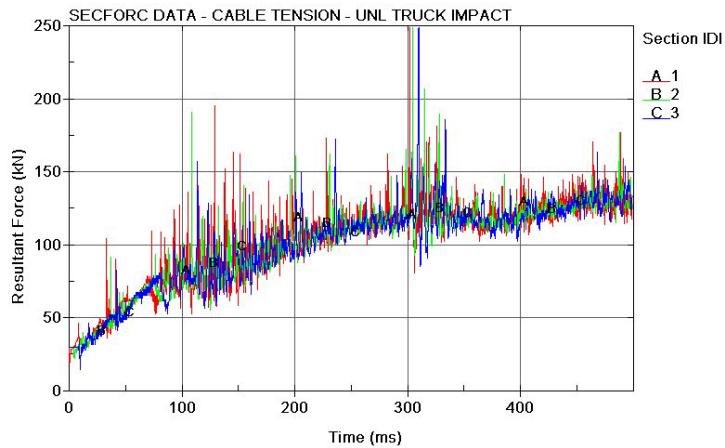


Figure 104. Model Lon-3, Secforc Data, Cable Tension

As the pickup truck penetrated behind the system, the moment created by the cable tension about the strong post axis resulted in loading of the slip base bolts on the outboard side of the slip base flanges. As is evident in Figure 105, this loading condition caused permanent bolt deformation, and similarly to the CT-1 crash test, caused some

overloading of the slip base in the non-slip direction. However, because the washers are not deformable in the LS-DYNA model as they are in reality, the failure mode was transferred to the bolts, rather than the washers. However, the Sb-3 slip base model retained the post, and thus the cables, throughout the Lon-3 impact.

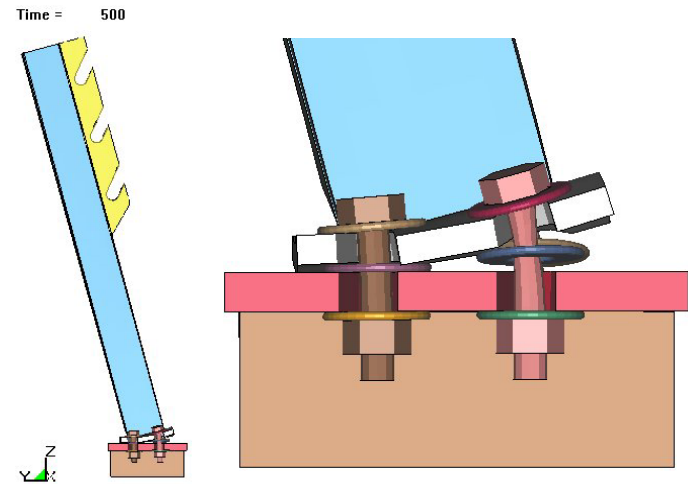


Figure 105. Model Lon-3, Sb-3 Post and Slip Base Following Impact

11.5 Conclusions

When comparing the simulated impact severity to that of the CT-1 crash test, the variables of interest are the cable tension and direction of action, because those are the variables that generate loads on the Sb-3 post and slip base model. Because the direction of cable action is nearly identical for all the simulations, as well as the CT-1 crash test, it was considered a constant for all cases within this study. Therefore, the only variable of concern for this study was the magnitude of the cable tension. So although the impact

energy in all the simulations are significantly below that of the CT-1 crash test, the simulations can be evaluated with regard to the tensile cable loads for validation of the Sb-3 slip base model. When a comparison between simulation and crash testing is conducted in this manner, it is apparent that the Lon-1 simulation most closely reproduces the crash test conditions, generating maximum cable tensions of about 100 kN per cable. The Lon-3 pickup truck simulation produced cable tensions about 20% higher than the CT-1 crash test, and the Lon-2 simulation produced cable tensions about 60% higher than the CT-1 crash test.

The results of the Lon-1 simulation generally indicated that the Sb-3 post and slip base model performed adequately in the length-of-need impact, with very similar behavior as observed in the CT-1 crash test. The Sb-3 post and slip base remained fixed to the base post, resisting the redirection of the vehicle, with slight permanent deformation to the slip base mechanism. Although the Lon-3 pickup truck simulation was about 20% more severe than the CT-1 crash test, it was concluded that the Sb-3 post and slip base model performed adequately in this simulation as well. Even though the bolt deformation was more severe, the post was restrained at the slip base during vehicle redirection.

The Sb-3 slip base model failed dramatically in the Lon-2 impact, with bolts failing and post detaching completely from the slip base. However, because the cable tension was about 60% higher than the measured values from the CT-1 crash test, it was concluded that this simulation produced an excessive loading condition on the slip base, and thus revealed that there exists an upper limit to the strength of the slip base mechanism. Rather than providing validation for the Sb-3 slip base model, the Lon-2

simulation supports the use of the Sb-3 slip base model as a predictive tool in slip base impact events.

From the analysis of the length-of-need simulations and the CT-1 crash test results, two main conclusions were drawn. First and foremost, it was concluded that the Sb-3 post and slip base model has been validated for use in full-scale impact simulations, as it exhibits acceptable behavior in both end-on impacts and length-of-need impacts. Secondly, the Lon-3 simulation revealed acceptable slip base performance for loads 20% greater than the CT-1 crash test, and the Lon-2 simulation revealed bolt overload failure for loads 60% greater than the CT-1 crash test. Based on these results of the Lon-2 and Lon-3 simulations, it was concluded that the actual slip base mechanism maintains a reasonable margin of safety at the CT-1 test conditions.

An apparent weakness of the Sb-3 slip base FEA model was revealed in the failure mode. In the CT-1 crash test the washers partially failed when the slip base was loaded with a moment about the strong post axis. However, the simulations produce bolt shaft failure due to the rigid washer material definitions. Even so, the Sb-3 slip base model produced a high level of realism in its ability to capture slip base behavior in a wide range of impact conditions.

12 SUMMARY AND CONCLUSIONS

The need for cable guardrail systems in shielding roadside hazards has produced various system designs over the years, many of which have proven extremely effective in redirective impacts. However, few have been approved for end terminal impacts. To remedy this problem, the Midwest Roadside Safety Facility has produced a new tangent cable system end terminal design. This design incorporates a cable release lever at the anchor and a slip base mechanism at the base of post number two for breakaway at low energy levels upon end-on impact.

A literature review revealed limitations in existing analytical techniques, as well as finite element models, directed at predicting slip base behavior for subsequent slip base development. Therefore, a new finite element slip base model was developed within this study using LS-DYNA.

The finite element model was developed by individually isolating the various physical phenomenon inherent in slip base design. As these phenomenon and their respective components were verified, they were slowly combined to incrementally increase the complexity of the model until the final end terminal model was attained.

Because friction is the primary failure mechanism in slip bases, the frictional slip behavior of LS-DYNA was investigated. The friction model consisted of a washer sliding along a flat plate. The friction study was a development process that optimized element size, element formulation, and slip velocity relative to the slip force data output. It was concluded that a very fine washer mesh was required for contact stability and to accurately capture theoretical slip behavior. Due to the fine mesh size and crash test results that indicated minimal washer deformation, as well as test results that indicated

non-deformable washers benefit slip base activation, the washer model was assigned rigid material properties. Fully integrated solid elements were used for the plate due to unacceptably high hourglass energy observed in constant stress solid elements. Finally, the ability of LS-DYNA to capture the static-to-dynamic friction transition was verified.

Three slip base clamping techniques were investigated. The first model, Jnt-1, consisted of two shell element plates clamped together using a discrete spring element. Although this technique was able to produce a prescribed load between the plates, it was unable to capture other mechanical interactions present in an actual slip base, and was thus abandoned in this study. The second clamping model, Jnt-2, was an improvement upon bolt models previously developed by NCAC and TTI (36). The Jnt-2 model consisted of a rigid bolt and nut connected with a discrete spring element which was assigned the tensile properties of the bolt shaft. This model proved to provide the specified clamping load between two plates, while also providing realistic interaction with other slip base components. Although it was an improvement over the Jnt-1 model, the bolt shaft's inability to deform was deemed a distinct limitation of the Jnt-2 model.

The third and final model, Jnt-3, was developed with the intention of closely reproducing the actual mechanics of a bolted joint. A preliminary study using the Stress-1 model proved the concept that prestressing of deformable solid elements could be used to generate tensile loads within the model. The concept of prestressing elements was applied to the bolted joint model. The Jnt-3 bolt model consisted of an integral bolt and nut modeled with deformable solid elements. The bolt shaft elements were assigned a prestress in accordance with the stress induced during the installation process. Not only

did this model provide preload between two plates, but it also allowed for deformation of the bolt under extreme loading conditions.

To gain further insight into the slip base slip forces, the MTS tensile test machine was used to gather data for the forced slipping of a bolted joint. A two-piece jig was constructed for the MTS machine using the slip base geometry and surface characteristics. The jig was clamped together using standard bolts torqued to slip base specifications, and the jig was then pulled apart while the MTS machine monitored the slip force. Two velocities were used: a quasi-static velocity of 0.1 in/sec, and a dynamic velocity of 10 in/sec. Using the average slip force data, a static friction coefficient of 0.134 and 0.180 was calculated for each respective velocity. A dynamic friction coefficient of 0.083 was calculated. These test values coincide well with published values, with the variation reasonably explained by inherent inconsistencies in clamping forces and surface characteristics.

The Jnt-2 and Jnt-3 clamping models were then used to simulate the pull-test sequence. Initial pull-test simulations using static friction coefficient (f_s) of 0.20 and dynamic friction coefficient (f_d) of 0.15 revealed significant noise in the slip force data, which was verified in an LSTC publication. (37) Therefore, subsequent simulations used an average recommended friction coefficient of 0.15 for both static and dynamic values. Although the test and simulation data did not coincide exactly, both Jnt-2 and Jnt-3 produced acceptable energy dissipation levels for the slip event. It is noted that the use of a deformable washer nearly duplicated the test data, but was deemed unacceptable for practical use due to increased computational time.

The two validated clamping techniques, Jnt-2 and Jnt-3, were then integrated into full post and slip base models designated Sb-2 and Sb-3 respectively. The Jnt-1 model was not pursued any further due to its inability to capture directional behavior. The Sb-2 and Sb-3 post and slip base models were impacted by rigid cylinders in three separate cases: (1) weak axis impact at 137 mm above the slip plane; (2) weak axis impact at 437 mm above the slip plane (bumper height); (3) and strong axis impact at 437 mm above the slip plane.

In Case 1, the Sb-2 and Sb-3 model both activated as desired; however, the Sb-2 model required about 20% more energy than did the Sb-3 model. In Case 2, the Sb-2 model locked-up, while the Sb-3 model activated and separated as desired. It was concluded that the rigid material properties of the bolt in Sb-2 resulted in wedging and binding of the top flange, not allowing it to slip free. During the strong axis impact of Case 3, the Sb-2 model displayed significant post and flange deformation due to the load transferred from the rigid bolts. However, the Sb-3 model displayed bolt overload and failure, indicating its ability to accurately capture bolt failure during uncommon or extreme impact conditions. Thus, The Sb-3 model displayed distinct advantages in both weak and strong axis impacts, and it was concluded that the Sb-3 model held the most promise for use in full-scale simulations.

A detailed model of the MwRSF cable system end terminal was developed. The model consisted of a cable support post and slip base, an anchor bracket for anchoring of the cable ends, a cable release lever for releasing the cable ends from the anchor bracket, and cable end fittings attached to the cables via spherical joints. This model was impacted end-on with a rigid bogie model supplied by Dr. John Reid. Although the Jnt-1

clamping technique, nor the Sb-1 post and slip base, were independently pursued in this study, it was previously investigated during the development of the end terminal model. The Sb-1 post and slip base model displayed acceptable overall system behavior in an end on impact, but its inability to capture directional behavior limits its usefulness. Rather, the Sb-3 model was used for this purpose. The Sb-3 model was integrated into the end terminal system and subjected to an end-on impact by the bogie vehicle. The simulation was validated using visual time comparisons from high-speed video of the actual crash test. It was concluded that the Sb-3 post and slip base model exhibited acceptable behavior in the end terminal impact.

Finally the Sb-3 end terminal model was integrated into a partial cable system model by Dr. John Reid. The cable system model included the end terminal system, as well as the post and slip base model Sb-3, along with post number three which was the first standard line post. The remainder of the line posts were not present. The cable system was subjected to a length-of-need impact by a bogie vehicle as well as a detailed pickup truck model. Both bogie and pickup truck simulations revealed comparable cable tensions with the CT-1 full-scale crash test values at significantly reduced velocities due to the absence of the line posts. However, the cable tension and direction are the only factors that affect the cable support post, and thus, correlate directly to the forces acting on the slip base. Based on the cable loading levels and direction of action that correlate directly with the CT-1 crash-test, the slip base and post remained fixed to the base post and resisted the cable loading with deformation similar to that observed in the CT-1 crash test.

The incremental development of the slip base model components verified their behavior in simplified test cases prior to integration into full-scale simulation models. This assured detailed understanding on the component level, and finally resulted in realization of the overall objective. Following the full-scale mid-length simulation, it was concluded that the Sb-3 post and slip base model has verified its ability to capture realistic slip base behavior in a wide variety of impact conditions. It is concluded that this model can subsequently be used with confidence in crash test analysis, further development of the cable system end terminal, or for alternate slip base applications.

13 FUTURE WORK and RECOMMENDATIONS

Although the Sb-3 slip base model has proven to behave acceptably under various impact conditions, there are many areas in which further investigation would benefit the overall goals of this study. This chapter outlines some suggested areas that would benefit the further development of the slip base and the overall cable system models.

The bolt model failed during a strong axis impact, and it deformed during the length-of-need impact. This bolt behavior is attributed to the low-carbon steel material model assignment. It would be of significant benefit if the actual bolt material was tested in an effort to develop an LS-DYNA material model for application to structural bolts. Following development of the bolt material model, strong axis impact validation of the Sb-3 post and slip base model is suggested.

A parametric study revealed that the fine washer mesh size was required for contact and slip force stability, but resulted in high costs due to computational time. Thus, the rigid washers were used as a compromise in the remainder of this study. However, the MTS pull-test data and simulation study concluded that significantly improved slip behavior was obtained when deformable material properties were assigned to the washers. It is recommended that further work focus on the use of deformable washers with regard to improved slip base activation behavior.

This study did not in any way take into account the post/soil interaction. Rather it made the assumption that the end anchor and slip base post were rigidly fixed to the ground. However, movement of both anchor and slip base post were observed in both the CT-1 and CT-2 full scale crash tests, and this movement may have significant effects on slip base activation behavior.

It is also recommended that cable and anchor bracket model instabilities observed during the end terminal impact be investigated further and improvements made prior to additional cable system simulations.

Finally, the variability in the torque-tension relationship is a variable that greatly affects slip base activation forces in practice. It is recommended that the empirical torque-tension relationship for 0.500-13 UNC bolts, as used in the cable system slip base, be thoroughly studied using strain-gauged bolts or other reliable techniques. Consistent control of the clamping load is essential for consistent control of the slip base activation forces and the subsequent impact severity. With extensive empirical clamping load data, the simulated clamping forces can be assigned with confidence, and thus, the simulation results will have greater ability to accurately predict slip base activation behavior.

14 REFERENCES

1. Hallquist, J.O., *LS-DYNA Keyword User's Manual*, Livermore, CA, Livermore Software Technology Corporation, March 2001.
2. Coon, B.A., Faller, R.K., Reid, J.D., *Cable Barrier Literature Review*, Transportation Record No. TRP-03-118-02, Midwest Roadside Safety Facility, University of Nebraska-Lincoln, July, 10, 2002.
3. Laker, I.B., Naylor, A.W., *Development and Proving Tests of a Four-Rope Safety Fence*, Transportation Research Record 1419, 1993.
4. *Wire Rope Safety Fence*, Highways and Departmental Standard TD 32/89, Department of Transport, Government of the United Kingdom, 1990.
5. Ray, M.H., Bryden, J.E., *Summary Report on Selected Guardrails*, Federal Highway Administration Report No. FHWA-SA-91-050, June 1992.
6. Minnesota Department of Transportation, Standard Plate No. M833OE, *3-Cable Guardrail*, November 2002.
7. Wisconsin Department of Transportation, Drawing S.D.D. 14B 1-2a, *Cable Guard Fence*.
8. South Dakota Department of Transportation, Plate No. 629.01, *3 Cable Guardrail*, March 2001.
9. Iowa Department of Transportation, Highway Division, Standard Road Plan RE-29C, *Cable Guardrail*, Revision No. 11, April 2001.
10. Phillips, R.G., Tyrell, A.B., Bryden, J.E., Fortuniewicz, J.S., *Cable Guiderail Breakaway Terminal Ends*, Federal Highway Administration Report No. FHWA/NY/RR-90/148, March 1990.
11. Mak, K.K., Bligh, R.P., Menges, W.L., *Testing of State Roadside Safety Systems*, Report No. FHWA-RD-95, Performed by Texas Transportation Institute for the Federal Highway Administration, August 1995.
12. Nebraska Department of Roads, Drawing No. 7020 1M 07, Special Plan C, *Cable Guardrail*.
13. Missouri Highway and Transportation Commission, Drawing No. M606.41F, *Three-Strand Guard Cable*, April 2002.
14. *A Guide to Standardized Highway Barrier Hardware*, AASHTO-AGC-ARTBA Joint Committee, May 1995.
15. Polivka, K.A., Faller, R.K., Sicking, D.L., Rohde, J.R., Reid, J.D., and Holloway, J.C., *Design and Evaluation of a Cable Guardrail End Terminal System* (In Progress), Transportation Record No. TRP-03-131-03, Midwest Roadside Safety Facility, University of Nebraska-Lincoln.
16. Ross, H.E., Perera, H.S., Sicking, D.L., Bligh, R.P., *Roadside Safety Design for Small Vehicles*, National Cooperative Highway Research Program (NCHRP) Report No. 318, Transportation Research Board, Washington D.C., May 1989.
17. Chisholm, D.B., Viner, J.G., *Dynamic Testing of Luminaire Supports*, Report No. FHWA-RD-73-55, Performed by the office of Research, Structures and Applied Mechanics Division, Federal Highway Administration, July 1973.
18. Juvinall, R.C., Marshek, K.M., *Fundamentals of Machine Component Design*, Second Edition, John Wiley & Sons, Inc., 1983.
19. Belter, D.J., *Investigation of a Bolted Splice Joint Under Dynamic Loading*, A Thesis, University of Nebraska-Lincoln, May 2002.
20. Edwards, T.C., Martinez, J.E., McFarland, W.F., Ross, H.E., *Development of Design Criteria for Safer Luminaire Supports*, National Cooperative Highway Research Program (NCHRP) Report No. 77, Highway Research Board, 1969.
21. Breaux, L.D., Morgan, J.R., *Evaluation of Small-Sign Systems from Existing Crash Test Data*, Transportation Research Record No. 1258, Transportation Research Board, National Research Council, 1990, pp 13-22.
22. Chisholm, D.B., Meczkowski, L.C., *Dynamic Testing of Luminaire Supports with an Improved Pendulum Impact Facility*, Report No. FHWA-RD-78-204, Performed by the office of Research, Structures and Applied Mechanics Division, Federal Highway Administration, September 1978.
23. Edwards, T.C., Hirsch, T.J., and Olson, R.M., *Design Criteria for Break-away Sign Supports*, Highway Research Record 222, 1968.
24. Pinelli, J.P., Subramanian, C.S., Tabora, J., *Experimental Study of Breakaway Highway Sign Connections*, Journal of Transportation Engineering, January/February 2002.
25. Shigley, J.E., Mischke, C.R., *Mechanical Engineering Design*, Fifth Edition, McGraw-Hill Inc., 1989.

26. Blake, Alexander, *What Every Engineer Should Know About Threaded Fasteners, Materials and Design*, Lawrence Livermore National Laboratory, Marcel Dekker, Inc., 1986.
27. *Bolt Torque Factors*, Design News, Design Aids, Nov. 1976. (*Nomogram for Torque on Bolts*, Design News, Design Aids, year unknown)
28. Parmley, Robert O., *Standard Handbook of Fastening and Joining*, McGraw-Hill Book Company, 1977.
29. *Friction and Its Challenges Confirmed by Others*, by Spiralock and the Lake Erie Screw Corporation, http://www.arvc.com/spiralock_friction.htm, 8-6-2002.
30. Faires, Virgil Moring, *Design of Machine Elements*, Fourth Edition, United States Naval Postgraduate School, The McMillan Company, 1965.
31. Myatt, Donald J., *Machine Design*, McGraw-Hill Book Company, Inc., 1962.
32. Pfeifer, B.G., Faller, R.K., Holloway, J.C., Post, E.R., *Full-Scale Crash Tests on a Luminaire Support 4-Bolt Slipbase Design*, Submitted to Transportation Research Board, Midwest Roadside Safety Facility, University of Nebraska-Lincoln, November 1991.
33. *Pressurex, Tactile Pressure Indicating Film*, Sensor Products Inc., <http://www.sensorprod.com>, 9-9-2002.
34. *Torque*, <http://www.steelstructures.com/SBH/SBH%20torque.htm>, 8-6-2002
35. Rothbart, Harold A., *Mechanical Design and Systems Handbook*, McGraw-Hill Book Company, Inc., 1964.
36. NCAC website, www.ncac.gwu/archives/model
37. Bala, Suri, *Contact Modeling in LS-DYNA – Some Recommendations – Part 1*, Livermore Software Technology Corporation, 2001.
38. Hallquist, J.O., *LS-DYNA Theoretical Manual*, Livermore Software Technology Corporation, May 1998.
39. Paulsen, G.W., *Design and Testing of a Dual Support Breakaway Sign Using Non-Linear Finite Element Analysis*, A Thesis, University of Nebraska-Lincoln, 1996.
40. Beer, F.P., Johnston, E.R., *Mechanics of Materials*, Second Edition, McGraw-Hill Inc., 1992.

41. Boresi, A.P., Schmidt, R.J., Sidebottom, O.M., *Advanced Mechanics of Materials*, Fifth Edition, John Wiley & Sons, Inc., 1993.
42. Hiser, N.R., Paulsen, T.J., *Simulation of Cable Terminal Bogie Test CTB-4*, Mechanical Engineering 950 Term Project, University of Nebraska-Lincoln, July 2002.
43. Fating, R.M., *Dynamic Impact Testing and Simulation of Cable Barrier Posts*, A Thesis, University of Nebraska-Lincoln, 2002.

15 APPENDICES

APPENDIX A: Fortran program used for solid element stress initialization.

```

c      Nick Hiser
c      10-16-02
c      init-stress.for
c
c      This program opens and reads a data file containing element
c      id's written from HyperMesh, and then generates DYNA
c      cards for *INITIAL_STRESS_SOLID that can be copied and
c      pasted into an existing DYNA deck.
c
c      The input file (input-sbX-XX.k) should be a file exported
c      from Hypermesh and edited to contain ONLY the data contained
c      in the *ELEMENT cards, i.e., without any comment ($) lines.
c      The file should contain only columns of numbers describing
c      eid, pid, n1, n2, n3, n4, n5, n6, n7, n8.
c
c      This program will write element id, number of integration point,
c      and 6 stress components for each integration point (8 points)
c      for every solid element to an output file called output.k.
c
integer IELE,n1,n2,nint
real sig11,sig22,sig33,sig12,sig23,sig13
sig11=0.0
sig22=0.0
sig33=0.2
sig12=0.0
sig23=0.0
sig13=0.0
nint=8

c
open(1,file='input-sbX-XX.k')
open(2,file='output.k')
c      write(*,*)'*INITIAL_STRESS_SOLID'
c      write(2,*)'*INITIAL_STRESS_SOLID'
c
c      This nested goto loop reads in element numbers from input file
c      one element number at a time, and then writes the *INITIAL_STRESS_SOLID
c      Dyna cards to a file called output.k.
c
10  read(1,30,end=60)IELE
    n1=0
    n2=0
c      write(*,*)$  eid  nint'
c      write(2,*)$  eid  nint'
    write(*,40)IELE,nint
    write(2,40)IELE,nint

```

```

c      write(*,*)$  sig11  sig22  sig33  sig12  sig23'
c      write(2,*)$  sig11  sig22  sig33  sig12  sig23'
20  write(*,50)sig11,sig22,sig33,sig12,sig23,sig13
    write(2,50)sig11,sig22,sig33,sig12,sig23,sig13
    n2=n1+1
    n1=n2
    if (n2.LT.8) goto 20
    goto 10
c
c      format(18)
30  format(2(7x,13))
40  format(2(7x,13))
50  format(6(5x,F5.3))
c
c      stop
60  end

```